ISSN : 2165-4069(Online)
ISSN : 2165-4050(Print)

IJARAI

International Journal of
Advanced Research in Artificial Intelligence

Volume 4 Issue 8

www.ijarai.thesai.org

A Publication of
The Science and Information Organization

INTERNATIONAL JOURNAL OF ADVANCED RESEARCH IN ARTIFICIAL INTELLIGENCE

THE SCIENCE AND INFORMATION ORGANIZATION

www.thesai.org | info@thesai.org

Editorial Preface

From the Desk of Managing Editor…

Artificial Intelligence is hardly a new idea. Human likenesses, with the ability to act as human, dates back to Geek mythology with Pygmalion's ivory statue or the bronze robot of Hephaestus. However, with innovations in the technological world, AI is undergoing a renaissance that is giving way to new channels of creativity.

The study and pursuit of creating artificial intelligence is more than designing a system that can beat grand masters at chess or win endless rounds of Jeopardy!. Instead, the journey of discovery has more real-life applications than could be expected. While it may seem like it is out of a science fiction novel, work in the field of AI can be used to perfect face recognition software or be used to design a fully functioning neural network.

At the International Journal of Advanced Research in Artificial Intelligence, we strive to disseminate proposals for new ways of looking at problems related to AI. This includes being able to provide demonstrations of effectiveness in this field. We also look for papers that have real-life applications complete with descriptions of scenarios, solutions, and in-depth evaluations of the techniques being utilized.

Our mission is to be one of the most respected publications in the field and engage in the ubiquitous spread of knowledge with effectiveness to a wide audience. It is why all of articles are open access and available view at any time.

IJARAI strives to include articles of both research and innovative applications of AI from all over the world. It is our goal to bring together researchers, professors, and students to share ideas, problems, and solution relating to artificial intelligence and application with its convergence strategies. We would like to express our gratitude to all authors, whose research results have been published in our journal, as well as our referees for their in-depth evaluations.

We hope that this journal will inspire and educate. For those who may be enticed to submit papers, thank you for sharing your wisdom.

Editor-in-Chief
IJARAI
Volume 4 Issue 8 August 2015
ISSN: 2165-4069(Online)
ISSN: 2165-4050(Print)

Editorial Board

Reviewer Board Members

CONTENTS

Paper 1: Wavelet Compressed PCA Models for Real-Time Image Registration in Augmented Reality Applications
Authors: Christopher Cooper, Kent Wise, John Cooper, Makarand Deo
PAGE 1 – 10

Paper 2: Analysis and Prediction of Crimes by Clustering and Classification
Authors: Rasoul Kiani, Siamak Mahdavi, Amin Keshavarzi
PAGE 11 – 17

Paper 3: Locality of Chlorophyll-A Distribution in the Intensive Study Area of the Ariake Sea, Japan in Winter Seasons based on Remote Sensing Satellite Data
Authors: Kohei Arai
PAGE 18 – 25

Paper 4: Appropriate Tealeaf Harvest Timing Determination Referring Fiber Content in Tealeaf Derived from Ground based Nir Camera Images
Authors: Kohei Arai, Yoshihiko Sasaki, Shihomi Kasuya, Hideto Matusura
PAGE 26 – 33

Paper 5: Driver's Awareness and Lane Changing Maneuver in Traffic Flow based on Cellular Automaton Model
Authors: Kohei Arai, Steven Ray Sentinuwo
PAGE 34 – 41

Paper 6: Application of distributed lighting control architecture in dementia-friendly smart homes
Authors: Atousa Zaeim, Samia Nefti-Meziani, Adham Atyabi
PAGE 42 – 49

Wavelet Compressed PCA Models for Real-Time Image Registration in Augmented Reality Applications

Christopher Cooper
College of Engineering
North Carolina State University,
Raleigh, NC, 27695

John Cooper
Department of Chemistry and Biochemistry
Old Dominion University,
Norfolk, VA, 23529

Kent Wise
SGS Inc.
The Woodlands, TX, 77381

Makarand Deo*
Department of Engineering
Norfolk State University,
Norfolk, VA, 23504

***Abstract*—The use of augmented reality (AR) has shown great promise in enhancing medical training and diagnostics via interactive simulations. This paper presents a novel method to perform accurate and inexpensive image registration (IR) utilizing a pre-constructed database of reference objects in conjunction with a principal component analysis (PCA) model. In addition, a wavelet compression algorithm is utilized to enhance the speed of the registration process. The proposed method is used to perform registration of a virtual 3D heart model based on tracking of an asymmetric reference object. The results indicate that the accuracy of the method is dependent upon the extent of asymmetry of the reference object which required inclusion of higher order principal components in the model. A key advantage of the presented IR technique is the absence of a restart mechanism required by the existing approaches while allowing up to six orders of magnitude compression of the modeled image space. The results demonstrate that the method is computationally inexpensive and thus suitable for real-time augmented reality implementation.**

Keywords—Image Registration; Principal Component Analysis; Wavelet Compression; Augmented Reality; Image Classification

I. INTRODUCTION

The utilization of augmented reality (AR) in the medical field provides multiple opportunities to enhance the access to and effectiveness of patient-specific medical information [1][2]. Using real-time AR systems allows the overlay, manipulation, and visualization of the various types of medical images acquired by MRI and tomography procedures (e.g., tissue, charge density, blood flow, etc.)[3][4]. Hence AR-based visualization techniques have been increasingly employed in safer medical practices for better understanding and accurate diagnostics. Creating an interactive 3D virtual model containing multiple dimensions of information, which can be manipulated and visualized in concert, provides immediate opportunities for high-quality medical training. Furthermore, the advanced AR-guided medical procedures have the potential to decrease the invasiveness and increase the safety and accuracy of a surgery by enhancing a surgeon's ability to utilize medical imagery during the operation [1][5]. The first step to achieving these goals however, is a robust and real-time registration of high resolution images [6]. This paper presents a novel registration method which is accurate and computationally inexpensive.

Image registration (IR) is the process of aligning two similar images, taken at different times or by different sensors, in order to correctly overlay an independent image [7]. IR techniques typically fall into two categories: feature-based [8] and intensity-based [9]. The former method relies on the detection and successful tracking of distinct image features, such as lines, corners, and contours, while the latter method determines a transformation using all of the image data. Each of these techniques relies on an optimization component, which determines the optimal spatial transformation, and a similarity metric, which compares the resemblance of the transformed scene image and the model image [7, 10]. Spatial transformations can be either rigid or non-rigid. Rigid transformations are composed of translation and rotation in three directions, for a total of six degrees of freedom. Non-rigid transformations account for these changes as well as those in the actual structure or anatomy of the object [11].

Initial IR techniques such as the iterative closest point (ICP) algorithm have produced incorrect transformations due to incoming image noise and prealignment errors [12]. One optimization approach to increase convergence range and avoid erroneous local optima is the use of hierarchical multi-scale, however down-sampling of images often suppresses key differences, leading to an absence of distinctive features in similar objects [11]. In response to these errors, evolutionary computation (EC) has been used to help alleviate the complex problems of image processing, most noticeably the need for a good initial estimation of the transformation. These models, included in the broader field of metaheuristics, rely on computational models of evolutionary processes to create populations of solutions [13]. One such example is the scatter search (SS) technique, which is a metaheuristic-based method

This work was supported in part by American Heart Association (AHA) Scientist Development Grant No. 12SDG11480010.

used in both feature-based and intensity-based methods [10]. Use of this technique provides noticeable advantages in the accuracy of transformations and eliminates prealignment error. Nevertheless, even IR techniques with metaheuristics rely on a restart mechanism when transformations become low quality. This is a result of the refinement process, which optimizes the previous transform in order to produce the new spatial transform for the incoming model image. Since optimizing a low-quality transformation is unlikely to produce a high-quality transformation, it is necessary to restart the algorithm and acquire a new initial transformation [10]. Recently, more advanced IR techniques have been proposed based on Speeded up Robust Features (SURF), optical flow method, and marker-free IR method [14][15]. However, these existing methods require extensive computations to achieve real-time IR which is a major concern that limits their use in real-time AR systems.

In this paper, a novel IR technique which is capable of achieving higher accuracy with substantially reduced computational time is presented. This was achieved by creating a database of compressed vectors from reference images of an object at all possible viewing angles and then constructing a corresponding principal component analysis (PCA) model prior to image registration. The proposed approach offers multiple benefits over existing methods. There is no need for an initial estimation or camera calibration, and furthermore, since the model operates independently for each incoming frame, there is no need for a restart mechanism. A systematic performance analysis of the proposed method is presented in this paper.

II. METHODS

A. Creation of Virtual Object Database

Current IR methods involve taking an existing image and transforming it in real time. With the use of high speed flash storage, it is now feasible and competitive to eliminate this transformation step, and simply recall previously generated high-resolution images. In this study, the virtual 2D images used in the registration process were generated from 3D imaging data prior to the real time registration process. A detailed 3D model of canine heart anatomy, derived from high resolution diffusion tensor magnetic resonance imaging (DTMRI) was used as the virtual object. A Virtual Object Database (VOD) was created by manipulating the orientation of the virtual heart model as a function of three orthogonal angles of rotation. Theoretically, there are an infinite number of possible orientations and hence 2D image views; however the ability to distinguish between similar orientations (2D images) decays as the change in an angle approaches zero degrees. Therefore, it is possible to represent an object within a pre-defined angular resolution with a limited number of image orientations. The degree of resolution, however, directly impacts the number of images needed in the VOD of 2D images. A total of 22,104 images were generated that fully represented all non-degenerate object orientations at 10° angle increments. At 5° resolution, a total of 186,624 images were generated. Since the virtual object was implemented in digital form, a high-resolution database was programmatically created using MATLAB software.

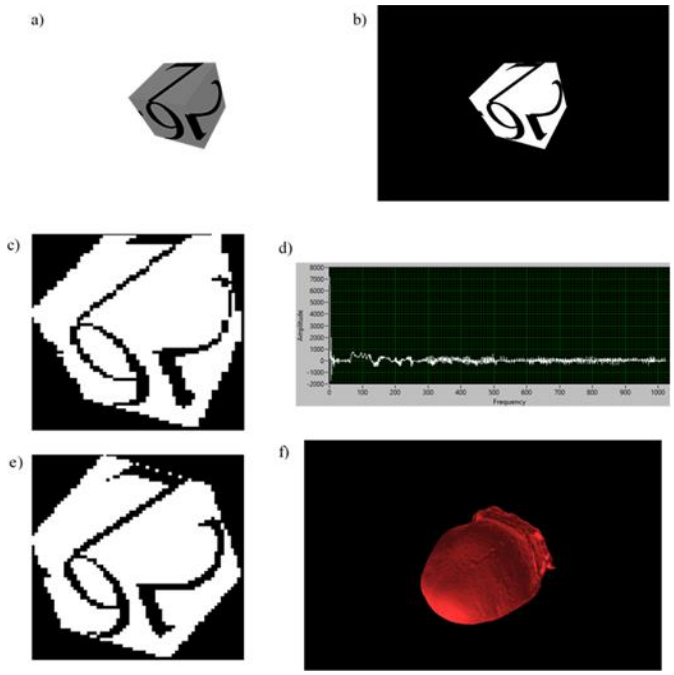

Fig. 1. This flow diagram shows the process of identifying the orientation of a reference object in the reference image and using it to correctly place a virtual heart image. The steps are: a) placement of 3D reference object in the scene, b) acquisition and processing of the reference 2D image, c) scaling of 2D image, d) wavelet transformation and compression of the 2D image, e) prediction of best match using PCA model, and f) registration and display of the appropriate virtual object image. A unique feature of this method is the absence of a restart mechanism

B. Creation of Reference Image Database

The first step in the proposed augmented reality method (shown in Figure 1) was registering an appropriate reference object in the scene to the appropriate 2D image from the VOD. Since the VOD was predetermined, the process was simplified as it only requires knowledge of the rotation of the reference object, its location within the scene, and the requisite scaling. In order to facilitate accurate determination of the three angles of rotation, the reference object must be appropriately designed. Although previous work has shown that this theoretically requires a reference object which has a minimum of four non-planar points [16], the results of this paper (described in Section 4) demonstrate that the accurate determination of the three orthogonal angles of rotation is highly dependent upon the asymmetry of the object such that as the asymmetrical complexity increases, the model accuracy increases as well.

Five reference objects (Objects I-V) with varying degrees of distinctive asymmetry (Figure 2) were created using a CAD software to study their effectiveness for precise object tracking based on optimal number of PCs required.

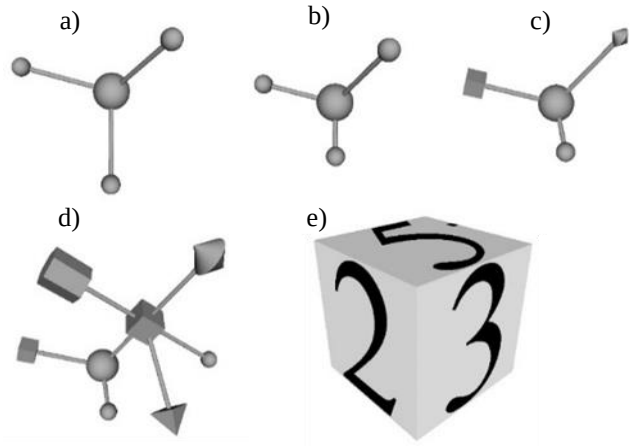

Fig. 2. The reference objects shown above are used to represent an increase in asymmetry for the reference object. The reference objects are a) Object I: Symmetric Spheres, b) Object II: Asymmetric Spheres, c) Object III: Three Shapes, d) Object IV: Multishape, and e) Object V: Dice

The first three reference objects possess only three distinct axes of asymmetry. Object I (Fig. 2a) contains bonds of equal length, resulting in a high degree of symmetry around the axes of rotation. It is worth noting that these symmetry elements are present in the 3D space of the real object. Object II (Fig. 2b) is similar, but all of the bond lengths are unique. In 3D space, this change results in the loss of all symmetry elements except for Identity. In Object III (Fig. 2c), two of the spheres have been replaced by unique shapes (a cube and a top). Object IV (Fig. 2d) possesses five axes extending from a cube where one axis has a highly complex structure attached to the end of the axis. Finally, Object V (Fig. 2e), a dice, has six perpendicular axes of asymmetry, created by a distinct number on each face. The numbers, which range from 2 to 7, were selected for their asymmetry, and hence the numbers 0, 1, and 8 were avoided since they possess symmetry elements other than the Identity.

The 3D reference objects were created as ".stl" files using Solid Edge, and reference images of the various rotations of each object were obtained in MATLAB in 10° increments for each of the three axes. The reference objects were also printed using a 3D printer and were used to acquire test images using a web camera at various object rotations and camera-to-object distances. Creating the reference object as a CAD file allows the Reference Image Database (RID) to be programmatically generated in the same manner as the VOD, while the ability to 3D print the object allows the generation of a physical reference object with high similarity to the RID. This approach ensures a high degree of correlation between the computer-generated images in the RID and the images of the reference object in the scenes that are acquired in real time.

C. Creation of Compressed Wavelet Vector Representation (CWVR) Database

In order to minimize the number of real-time calculations required for image registration, the resolution of the images in the RID was lowered and then the images were compressed further using a wavelet transform. This allowed each image in the RID to be represented by a compressed wavelet vector which was orders of magnitude smaller in number of pixels. These compressed wavelet vectors were arranged into a reference database which was used to construct the PCA model and to carry-out real-time calculations. Construction of the compressed wavelet vector reference (CWVR) database involved two steps: i) reference image scaling and ii) wavelet transformation and compression.

1) Image Scaling

Although the CAD file used to generate the RID provides high resolution, the results show that a lower resolution allows for faster processing while still allowing for sufficient information to maintain PCA model accuracy. Hence the resolution of the images in the RID was maintained at 64x64 pixels. Due to the calibration-free approach of the proposed model, there is no incoming information about the distance between the reference object and the camera. As such, a scene with a large camera-to-object separation will display a small reference object (low pixel resolution), while a scene with a small camera-to-object separation will display a larger one (high pixel resolution). In each case, however, the orientation of the reference object remains unchanged. Hence, if the object is appropriately scaled, and the scaled image possesses sufficient resolution, the numerical values of three distinct rotation angles can be determined from the PCA model. However, to preserve the scaling required for image registration, it is necessary that both the reference object images in the RID and in the scene be scaled in a similar manner. To achieve this, the incoming scene image was either up-sampled or down-sampled to the same resolution as the RID.

In both cases (scene and RID), the image was restricted to only the contents of a rectangular bounding box using the topmost, leftmost, rightmost, and bottommost points of the reference object. The horizontal scaling (S_h) required for image registration was defined as:

$$S_h = \frac{(i_R - i_L)}{n} \quad (1)$$

where i_R is the index of the rightmost side of the bounding box of the scene image, i_L is the index of the leftmost side of the bounding box of the scene image, and n is the horizontal pixel resolution in the RID. Similarly, the vertical scale (S_v) was defined as:

$$S_v = \frac{(i_T - i_B)}{n} \quad (2)$$

where i_T is the index of the topmost side of the bounding box of the scene image, i_B is the index of the bottommost side of the bounding box of the scene image, and n is the vertical pixel resolution in the RID (same as horizontal).

2) Wavelet Transform and Compression

Each scaled image was subsequently stripped into a single vector by unfolding the rows of the image. A wavelet transform with four wavelets and scaling functions [17] was applied to the resulting vector. The Daubechies family of orthogonal wavelets was chosen due to their extensive use in

data compression. Specifically, the Daubechies wavelet filter with 8 taps and 4 vanishing moments was selected (also referred to as a D8 or db4 referring to the N=2A relationship between the number of taps, N, and the number of vanishing moments, A) as a reasonable compromise between image resolution and compression efficiency. The advantage of the wavelet transform is that it preserves both the frequency and the position information of the image vector (i.e., the function is not translationally invariant as is the case with most Fourier transform methods) [18]. Moreover, the use of discrete wavelet transform (DWT) is computationally efficient. Due to the nature of the reference object image, the dominant and requisite information was contained almost completely in the low frequency wavelet coefficients. Thus, the final step of compression involved truncating the high frequency wavelet coefficients to achieve image compression while preserving the lowest 1024 coefficients that retain essential information needed to determine the object orientation. As shown in Figure 3, the original input sample image (Panel A) and the reconstructed compressed image after wavelet transform (Panel B) were almost identical, but the latter required 75% less data for creation and storage. A slight blurring of sharp edges in the compressed images due to the loss of the high frequency components is evident in the figure but this had an insignificant impact on the accuracy of the PCA model.

D. Constructing the Principal Component Analysis (PCA) Model

Once the CWVR database was created, it was then used to construct a PCA Model [19]. The use of a PCA model provided two distinct advantages. First, it allowed the CWVR for all images of the reference object to be described using a multi-dimensional eigenvector space that accounted for the greatest variance of the underlying data structure. Second, it enabled each CWVR to be mapped into the eigenvector space by using a single scalar value (eigenvalue or score) for each eigenvector. Since the number of eigenvectors (more commonly referred to as principal components) required to account for the majority of variance was considerably less than the length of the CWVR, a significant further compression of the data dimensionality was achieved. For example, if the CWVR contained 1024 data points, and the variance was described by 10 principal components, then a compression of 100-fold was achieved since each CWVR could now be represented by only 10 eigenvalues within the space of the PCA model.

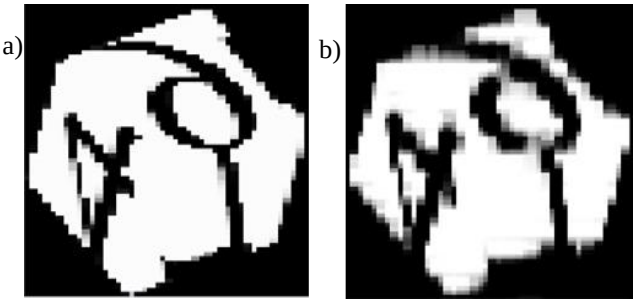

Fig. 3. Two images a) before wavelet compression and b) after wavelet compression are shown. The differences in the images are minimal, however, the amount of information required to reconstruct the image after compression is significantly smaller, and is used as the basis of the CWVR database

The PCA model was constructed by creating a data matrix X, where each row of the matrix corresponds to a CWVR, and the number of rows is equal to the number of reference images. The data matrix was then decomposed using a singular value decomposition algorithm:

$$X = U\Sigma V^T \quad (3)$$

where U is an $n \times m$ orthonormal matrix, Σ is an $m \times m$ eigenvalue matrix with all zero off-diagonal elements, $\mathbf{V}^T$ is an orthonormal $m \times m$ matrix, n is the number of reference images and m is the length of the CWVR. Each row of matrix V^T is an eigenvector or principal component (PC), thus the resulting number of principal components is equal to the length of the CWVR. Since V^T is an orthonormal matrix, all of the PC row vectors are orthogonal and define a multivariate space containing the compressed images. The coordinates of each compressed image within this multivariate space was given by the rows of a scores matrix, S, which is simply:

$$S = U\Sigma \quad (4)$$

where S is a $n \times m$ matrix. Thus the scores reflect where each sample lies on the PC axes. However, since the PCs were sorted in decreasing order of variance, the majority of the variance was described by the first few PCs and the higher order PCs were dominated mostly by noise. This allowed the PCA model to be constructed by truncating to the number of columns (k) in the scores matrix, S, and the loadings matrix, V:

$$X' = S'(V')^T \quad (5)$$

Where X' is an approximation of the compressed image data, and S' and V' have $k \times m$ dimension ($k \ll n$). T indicates the transpose. Figure 4 illustrates the matrix order reduction obtained while solving the Eqn. 5.

E. Image Registration

Since this was a rigid image registration method, there were six degrees of freedom which had to be determined in order to accurately display a virtual object in the scene image. These included three degrees of freedom in translation and three degrees of freedom in rotation.

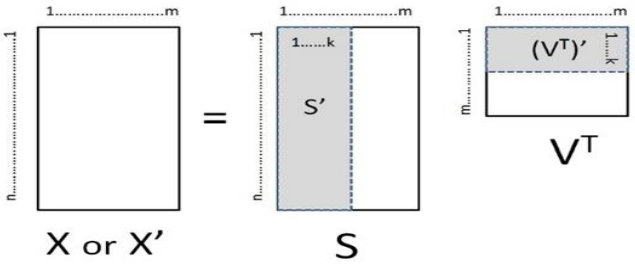

Fig. 4. The equation for creation of the PCA model is shown where n corresponds to the number of images in the PCA model and m corresponds to the length of the compressed wavelet vector representation (CWVR) of each image. The solid polygons correspond to the data matrix **X**, the scores matrix **S**, and the loadings (principal component) matrix $\mathbf{V}^T$. The dashed polygon boxes correspond to the retained columns (k) of **S** and **V** which are used to construct an approximation (**X'**) of the data matrix to generate the PCA model

The translation that occurred between two images was determined by using the information acquired during the image scaling process. By comparing the geometric mean of the bounding box surrounding the reference object between the model and scene image, the translation on the two axes (which are parallel to the sides of the image) was determined. Translation along the third axis was accounted for by scaling the virtual object image according to the scale of the incoming reference object image. This was performed using the horizontal and vertical scale ratios given by Eqn. 1 and Eqn. 2, respectively.

The rotation around three orthogonal angles was simultaneously determined by using the PCA model as discussed earlier. An image of the reference object in an incoming scene was processed in the same way as that of the CWVR database. The PCs of the unknown object orientation were then calculated using the resulting CWVR (y) and the reference object PCA Model (i.e., the truncated matrix $(V')^T$) by solving Eqn. 6 for the scores vector s:

$$(V')^T s = y \tag{6}$$

Since the PCs are orthogonal, $[(V')^T]^{-1} = V'$. This yielded a trivial solution for determining the scores for unknown compressed images:

$$s_{new} = y_{new} V' \tag{7}$$

where s_{new} corresponds to the scores vector containing the coordinates of a new compressed image in PCA space and y_{new} is the CWVR for the new image. The significance of Eqn. 7 is that regardless of the size of the image database used to create the PCA model, the model of the image space was described by a $n \times k$ matrix, where k is the number of PCs and n is the length of the CWVR. Thus for an image database at 10 degree resolution (total 22,104 images) where each original image was defined by 1024x 1024 pixels ($n = 1024$), a PCA model containing 22 principal components ($k = 22$) yielded a compression of the database by six orders of magnitude.

Although it is possible for the new image to contain an exact match with the scores of the database, this probability was limited by the angular resolution of the database. For this reason, the best match was taken as the nearest neighbor (smallest distance) in PC model space, where the distance from nearest neighbors was calculated as the sum of the squares of the score differences:

$$d = \sum_{PC=1}^{k} (\boldsymbol{s}_{\mathrm{PC}}^{\mathrm{new}} - \boldsymbol{s}_{PC}^{model})^2 \tag{8}$$

where d is the distance, k is the maximum number of PCs in the model, and s is the score for a particular PC for the new image being predicted and a neighboring images contained in the PCA model. Since each vector in the CWVR database was indexed to the angles of rotation of its reference image, identifying the best match also identified the corresponding values for rotation about three different axes.

Each reference object was tested using PCA Models constructed using a PC space ranging from one to 50 PCs in order to determine the optimal number of PCs for that object. The optimum number of PCs was chosen as the minimum PC number where adding an additional PC did not yield a statistically significant decrease in the standard error of the model predictions. This was determined by Malinowski's F-test [20]. Malinowski's F-test assumes that the sum of the eigenvalues can be decomposed into either parts which are significant or noise, and that the significant eigenvalues provide an estimate of the true number of principal components needed. If there are a maximum of p possible principal components (the minimum of either the number of samples or the number of variables), then the F-statistic for the s^{th} eigenvalue (λ_s) is:

$$F_s = \frac{\lambda_s}{\sum_{j=s+1}^{p} \lambda_j/(\mathrm{p} - \mathrm{s})} \tag{9}$$

and the maximum PC is taken as that having the minimum F_s value.

The best match for an acquired image was restricted to a reference object image within the CWVR database (10° angle increments) and as such, an angle error of less than or equal to ±5° is considered accurate. Thus for an incoming sample image with a 45° rotation on a particular axis, a correct match is either 40° or 50° in that same angle. Figure 5 illustrates one example of the largest error for an incoming scene image with X-axis rotation =45°, Y-axis rotation =315°, Z-axis rotation =0° (henceforth written as: 45°, 315°,0°) (panel a) and the corresponding best RID correct match through the PCA

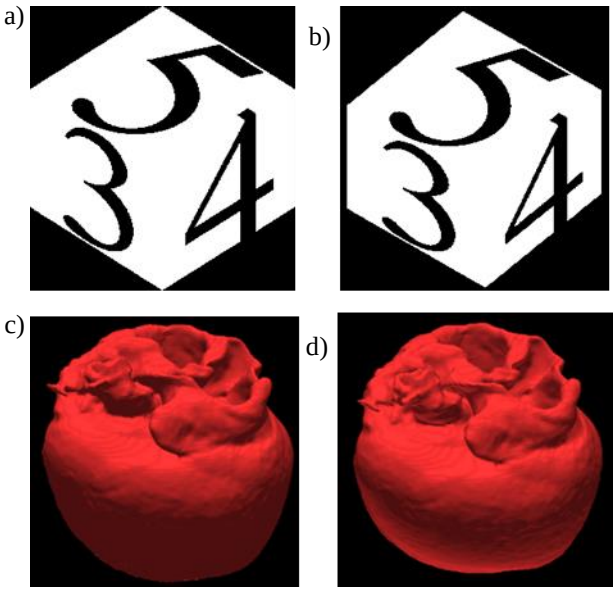

Fig. 5. Shown is an example of the largest error for a correct match given the selected angular resolution (10° increments) of the reference image database. The images shown are a) the scene image (45° 315° 0°), and b) the best RID match through PCA analysis (40° 310° 0°). The corresponding registered heart images are shown in c) and d). As seen, the difference between the two Object V images and their respective heart images is barely perceptible, but could be further reduced by using a higher angulation resolution (i.e. 5° increments)

analysis (40°, 310°, 0°). As seen, the difference between the two Object V images and their respective heart images is barely perceptible, but could be further reduced by using a higher angulation resolution (i.e. 5° increments).

The performance of the object matching algorithm was assessed by percent error (δ) calculated as:

$$\delta = \frac{i}{a} \times 100 \qquad (10)$$

Where i was the number of incorrect angle matches over a certain tolerance of error for a given PCA model and a was the total number of angles (or three times the number of images tested).

III. Results

The percent standard errors for each reference object model as a function of the number of PCs are plotted in Figure 6**.** Each model reaches an apparent minimum percent error after reaching an optimum number of PCs, implying that the additional PCs are no longer providing significant additional information. For all objects, the error dropped significantly for the initial PCs after which the accuracy does not improve noticeably for higher order PCs. It was observed that the accuracy improved with extent of asymmetry in the objects with the most symmetric object (Object I) giving the highest error and the most asymmetric object (Object V) giving the lowest error regardless of the number of PCs included.

Table I lists the number of optimal PCs needed for each type of reference object. It was observe that as the asymmetry of the reference object increases, the number of PCs required to describe the variance of the CWVR database increases. Thus the highly symmetric object (Object I) required only 9 PCs, while the most asymmetric object (Object V) required 29 PCs. The table also provides percent errors for each reference object PCA model at the optimum PC number. The percent errors are broken down into three categories: 15° (the percent of incorrect predictions exceeding an error of 15°), 10° (percent of incorrect predictions exceeding an error of 10°), and 5° (percent of incorrect predictions exceeding an error of 5°). Also shown for each object PCA model is the root mean square of the distances between the reference and sample images where an error less than or equal to 5° is considered accurate. As can be observed, the results showed a significant increase in both accuracy and the optimum number of PCs as the complexity of the asymmetry in the reference objects increased.

The errors shown in Table I and Figure 6 both correspond to errors in the predicted angle vs. the actual angle of rotation. However, since each object possesses 3 orthogonal angles of rotation, it is possible for each image mismatch to correspond to one or more improper angles. The actual number of incorrect images and incorrect angles for each of the 672 tested samples is given in Table II.

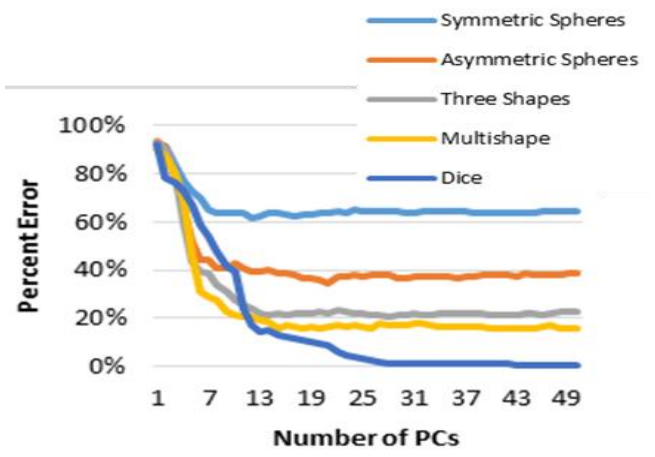

Fig. 6. The graph shows the percent standard error of the PCA model for each reference object as a function of number of retained PCs. Initially the error decreases rapidly with each addition of a PC, however, after a certain number of PC's the resulting decrease in error becomes minimal, implying that the inclusion of further PC's is no longer providing significant information to the PCA model. Reference objects with higher degrees of asymmetry yield correspondingly lower errors once the minimal number of PCs is reached

TABLE I. Effect of Reference Object Asymmetry on PCA Optimal PC# and PCA Model Error

Object	Optimal Number of PCs	Percent Error (5°)	Percent Error (10°)	Percent Error (15°)	Average RMS
Object I	9	63.79%	61.71%	56.35%	62.9964
Object II	12	39.63%	30.26%	28.47%	31.9440
Object III	14	21.58%	11.86%	9.62%	12.4449
Object IV	24	16.82%	8.48%	5.26%	6.7919
Object V	29	0.79%	0.00%	0.00%	0.1022

TABLE II. The Number of Incorrect Image and Angle Predictions (At 5°) When Predicting the 671 Unique Samples

Object	Optimal Number of PCs	Incorrect Images	Incorrect Angles	Average
Object I	9	498	1286	2.582
Object II	12	330	799	2.421
Object III	14	224	435	1.942
Object IV	24	189	339	1.794
Object V	29	9	16	1.778

As the asymmetry increased for the first four objects, the number of image mismatches decreased monotonically from 498 to 189. For the Object V PCA model, however, there was a precipitous decrease to only 9 incorrect images. Table II also gives the average number of incorrect angles per sample, and shows that as the average number of incorrect angles in each image mismatch decreased with an increase in asymmetry in the objects. One example of an image mismatch for Object II is shown in Figure 7. Panel a) corresponds to a test sample (60°, 50°, 210°) and Panel b) corresponds to the PCA predicted match (140°, 230°, 90°).

As can be seen, although the object possesses no symmetry in 3D space, there still exist combinations of distinct angle rotations which yield 2D views which are nearly identical. This predicted mismatch problem was further exacerbated upon image compression. Figure 8 shows one example for Object III after compression and scaling. The image with rotations (10°, 180°, 80°) (Panel A) was wrongly recognized as (0°, 0°, 40°) (Panel B), leading to an error of 230°. At the lower resolution, the image differences approach the noise limit.

For Object V, the highest error mismatch is shown in Figure 9 (reconstructed from their respective CWVRs). Despite the low resolution, the images are clearly distinguishable with the rotations of (90°, 90°, 285°) in Panel A, and that of (100°, 80°, 290°) in Panel B. The relatively small angle error combined with the *visually distinguishable features* of the two images suggests that the cause of the mismatch was rooted in the PC model itself. Indeed, a plot of the % variance attributable to each PC (Figure 10) indicated that the higher order PCs for object V constituted a significant amount of variance (Figure 10, inset) when compared to that of more symmetric object (Object II). This is consistent with the finding that more PCs are required to effectively describe the modeling space of objects with greater asymmetry (Figure 6). It also suggests that using an F-test may not be a reliable

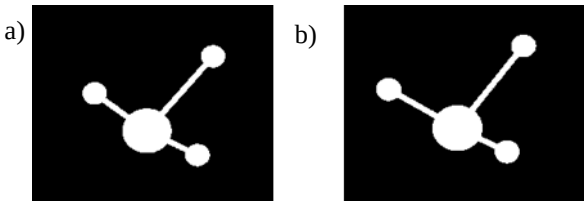

Fig. 7. An image mismatch resulting from PCA model of the Asymmetrical Spheres reference object. The images are shown at high resolution prior to compression. The left image (x-axis rotation = 60°, y-axis rotation = 50°, z-axis rotation 210°) is very similar, even at high resolution, to the right database image (x-axis rotation = 140°, y-axis rotation = 230°, z-axis rotation = 90°); however the angles are significantly different. This is a result of the loss of information as one moves from 3D to 2D space

method to determine the optimum number of PCs since the percentage of incorrectly identified object images beyond 29 PCs is relatively small (1.34%; 9 out of 672 images). When the Object V PC model is expanded to 45 PCs, the number of image mismatches dropped to 6 (0.89% incorrect) and no mismatches at 200 PCs. Thus the error in the Object V PCA models appears to originate in the ability of the PCA model to describe the asymmetry and not in the lack of distinguishable asymmetry. Since the truncation of PCs for a given model is part of the data compression, it suggests the need to balance compression in an effort to maintain the asymmetric properties required for accuracy. This is not noteworthy in case of more symmetric objects since the error remains high even for a significantly larger number of PCs (see Figure 6). Although a higher degree of asymmetry requires a higher number of PCs to maintain accuracy, the overall compression is still significant. For example, the original sample image contains over 1 million pixels, and conversion to a 64x64 image results into 4096 pixels. It is further reduced to 1024 pixels after wavelet compression and truncation. Thus even when using 200 PCs to represent the image, provides an additional factor of 5 in data compression and yields a total data compression of over 5000 per image. With regards to the image database space (22,103 images x 1024 x 1024 = 23 billion coordinates), the PCA model compression (200 PCs x 1024 length of CWV = 204,000 coordinates) still results in five *orders of magnitude* compression.

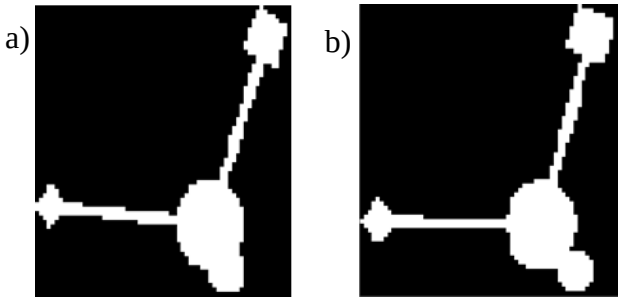

Fig. 8. The figure shows an example of a PCA predicted image-mismatch for the Object III PCA model. The images are shown after scaling and image compression. The differences between the top image (10°, 180°, 80°) and the bottom database image (0°,0°,40°) are almost indistinguishable at the lower resolution, where they approach the noise limit

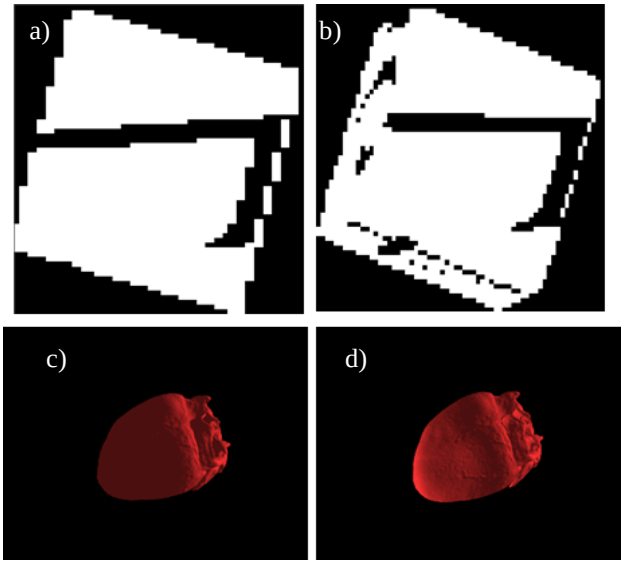

Fig. 9. An example of the maximum error obtained using a PCA model with 29 retained principal components for Object V is shown. The images are a) the sample image (90°, 90°, 285°), b) the best match (100°, 80°, 290°), c) the heart image corresponding to the sample image, and d) the heart image corresponding to the best match. Since the images are visually distinctive, it can be reasoned that the error lies in the PC model itself and indicates the need for additional PCs if more accuracy is required

The PCA models for each object were constructed using 22,103 images (i.e., 22,103 vectors in the CWVR database). Figure 11 shows the PCA space defined by these images at various orders of PCs for Object V (Fig. 11d-e) and Object II (Fig. 11a-c). The panels A and D show contents of the images extracted in the first three principal components (X, Y and Z axes). As can be seen, the plot for Object II (Panel a) exhibits a great deal of structure. Indeed, if the points in the plot are considered as a solid object, a 3-fold improper axis of rotation exists (S_3). For the Object V plot (Panel d), the defined space is less structured, and although not spherical, is significantly

more homogeneous. As higher PC numbers are used to define the axes, the spread in the PC scores decreased for both objects, as expected.

IV. Discussion

The paper presents a novel image registration method using pre-processed database of compressed image vectors spanning all possible image rotations and scaling. This method uses a combination of discrete wavelet transform to compress the images without losing any valuable information and principal component analysis to construct an accurate estimation model. This approach significantly reduced the computations and enabled real-time processing for seamless medical augmented reality applications.

The computational benefits of this approach are achieved by utilizing additional computational time prior to image registration for processing already acquired reference image database using a reference object with distinct and complex asymmetric properties. By acquiring reference object images

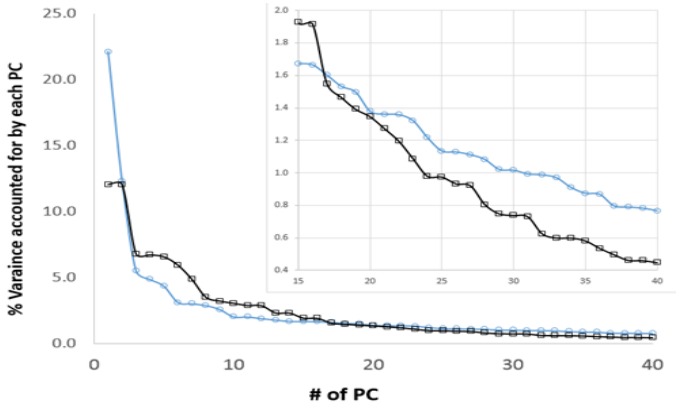

Fig. 10. The graph shows the relationship between %variance and the retained PC number for Object V and Object II. The graph inset shown in the top right shows that the Object V PCA model still contains a significant amount of variance at higher order PCs when compared to the PCA models of the more symmetric reference objects. This indicates that more PCs are required to accurately reflect the higher degree of asymmetry and is supported by the observation that inclusion of 200 PCs in the Object V PCA model eliminates all mismatches

from multiple viewpoints, a comprehensive model can be developed using principal component analysis which accurately matches an incoming image whose angles of rotation (with respect to the viewer) are not known, with a corresponding reference image. Since the reference image is indexed to the angles of rotation, image registration is straightforward and only requires scaling and positioning. Alternatively, these indexed angles can be used to determine an appropriate transform of the 3D virtual heart model into 2D image space. The advantages of the former are - 1) the bulk of the computations (generating high resolution heart images, building the reference image database, and constructing the PCA models) are carried out only once and in advance so that the real-time IR is computationally inexpensive; and 2) the current trend in computing storage is the use of high speed flash interfaced to the CPU via a high speed bus (e.g. PCIe) which allows extremely fast image recall. Thus the IR time of this algorithm remains superior to the existing method while offering the advantage of a higher resolution rendering upon registration.

The robust nature of the model presented in this paper is created due to the use of a predefined, asymmetric reference object which is present in the incoming image. Unlike other methods, where tracked features are chosen in real time [8,9,21], in this method, the tracked features are predetermined. This significantly enhances the speed and accuracy of image registration at the cost of creating a more rigid technique which requires the presence and visibility of a specific reference object. Traditional IR methods rely on the creation of mathematical transformations to track features in scene images which are cumbersome to use with higher resolution images, and require "good" features which can be easily tracked [22] [23]. Intensity-based IR is one way to bypass this requirement, but these methods still employ a mathematical transformation, which ultimately increases the amount of real-time computation necessary for image registration [9]. Intensity-based IR methods also require a computationally expensive restart mechanism to obtain an optimal transform instead of trying to refine a bad transformation [10]. The proposed method, however, does not refine previous transforms, eliminating the need for a restart mechanism altogether.

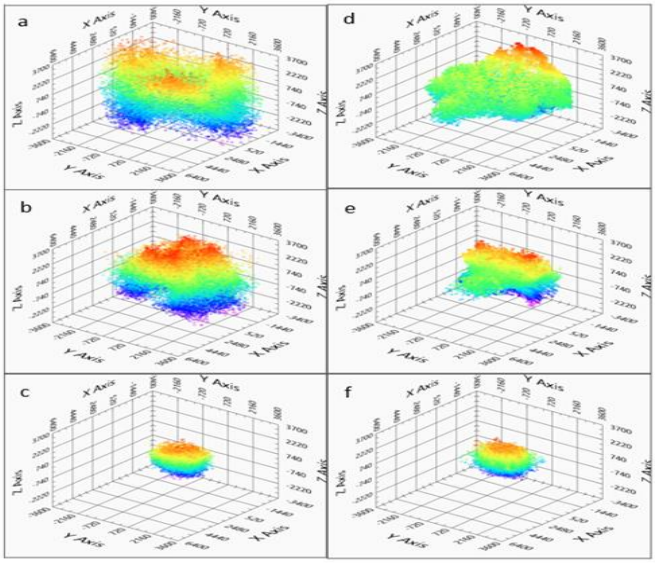

Fig. 11. The figure shows the PC space of the PCA model for Object V (right) and Object II (left) using different combinations of PCs for the axes of the space. The top images show the scores for the 1st (x-axis), 2nd (y-axis), and 3rd (z-axis) PCs. The middle images show the scores for the 4th, 5th, and 6th PCs; and the bottom images show the scores of 27th, 28th, and 29th PCs. A three-fold axis of improper rotation (S_3) can be seen in the Object II PCA space for the first 3 PCs (top left), while the similar PCA space for Object V is more homogenous (top right)

The significant difference of the proposed method compared to other IR techniques makes it difficult to draw a direct comparison. Nevertheless shape-based image retrieval techniques have often utilized PCA in order to reduce data dimensionality and decrease computation time. Image retrieval methods have demonstrated that more complex shapes are easier to use with PCA analysis [24], and the principal component descriptors are preferable to other methods of image identification and retrieval [25]. Content based image

retrieval (CBIR) is a popular technique that utilizes such methods to search and retrieve images from large databases [26]. Typically employed to manage large volumes of digital images, this technique is similar to the proposed method which is repurposed as an IR method.

When uniform PCA space is encountered in a model, it is common to convert from a PCA classification method (as used in this paper) to a principal component regression (PCR) method [27] in order to derive more quantitative results (e.g., the ability to quantitatively interpolate between the modeled angles). Although it is beyond the scope of the present work, construction of a PCR model for this implementation of augmented reality would involve the multivariate regression of the scores of a PCA model against the angles of rotation. This could also be accomplished with a partial least squares model using a PLS-2 algorithm [28]. The more homogenous clustering for the Object V PCA model would suggest a greater likelihood of success of such quantitative modeling when using a higher degree of reference object asymmetry. This further exemplifies the importance of introducing complexity into the asymmetry of reference objects.

V. CONCLUSIONS

This paper presents a novel image registration technique involving image compression and PCA modeling based on the use of reference objects with complex asymmetry. The design provides a method to eliminate the real-time computational costs of performing geometric transforms and by using PCA classification, operates without the need for a restart mechanism. The method was validated using 672 object images to test a PCA model created from 22,103 reference images. The asymmetry of the reference objects was found to highly correlate with the accuracy of the image registration. In particular, for highly asymmetric objects, the accuracy was predominantly dependent upon the inclusion of enough principal component vectors to accurately describe the asymmetry of the objects described in the PCA model space. For higher symmetry objects, the inclusion of higher PC order models had little to no impact on the accuracy. Future studies could further investigate the properties and uses of complex asymmetry to enhance the accuracy of image registration methods. Since the majority of image processing in this method is done prior to the real-time process, and the data compression resulted in significant reduction in memory requirements, the proposed method is well suited for real-time medical augmented reality applications.

REFERENCES

[1] Azuma, R., Baillot, Y., Behringer, R., Feiner, S., Julier, S., & MacIntyre, B. "Recent advances in augmented reality. Computer Graphics and Applications," IEEE, vol. 21, no. 6, pp. 34-47. Nov, 2001.

[2] Van Krevelen, D., & Poelman, R. "A survey of augmented reality technologies, applications and limitations," International Journal of Virtual Reality, vol. 9, no. 2, pp. 1-19. Jun, 2010.

[3] Fritz, J., Paweena, U., Ungi, T., Flammang, A. J., Fichtinger, G., Iordachita, I. I., & Carrino, J. A. "Augmented reality visualisation using an image overlay system for MR-guided interventions: technical performance of spine injection procedures in human cadavers at 1.5 Tesla," European radiology, vol. 23, no. 1, pp. 235-245. Jul, 2013.

[4] Azagury, D., Ryou, M., Shaikh, S., San José Estépar, R., Lengyel, B., Jagadeesan, J., . . . Thompson, C. "Real-time computed tomography-based augmented reality for natural orifice transluminal endoscopic surgery navigation," British Journal of Surgery, vol. 99, no. 9, pp. 1246-1253, Sep, 2012.

[5] Nakamoto, M., Ukimura, O., Faber, K., & Gill, I. S. "Current progress on augmented reality visualization in endoscopic surgery," Current opinion in urology, vol. 22, no. 2, pp. 121-126, Mar, 2012.

[6] Liao, H., Inomata, T., Sakuma, I., & Dohi, T. "3-D augmented reality for MRI-guided surgery using integral videography autostereoscopic zimage overlay," Biomedical Engineering, IEEE Transactions on, vol. 57, no.6, pp. 1476-1486, Jun, 2010.

[7] Zitova, B., & Flusser, J. "Image registration methods: a survey, Image and vision computing, vol. 21, no. 11, pp. 977-1000, Jun, 2003.

[8] Reddy, B. S., & Chatterji, B. N. "An FFT-based technique for translation, rotation, and scale-invariant image registration," IEEE transactions on image processing, vol. 5, no. 8, pp. 1266-1271, Aug, 1996.

[9] Kim, J., & Fessler, J. A. "Intensity-based image registration using robust correlation coefficients," Medical Imaging, IEEE Transactions on, vol. 23, no. 11, pp. 1430-1444, Nov, 2004.

[10] Valsecchi, A., Damas, S., Santamaría, J., & Marrakchi-Kacem, L. "Intensity-based image registration using scatter search," Artificial intelligence in medicine, vol. 60, no. 3, pp. 151-163, Feb, 2014.

[11] Markelj, P., Tomaževič, D., Likar, B., & Pernuš, F. "A review of 3D/2D registration methods for image-guided interventions," Medical image analysis, vol. 16, no. 3, pp. 642-661, Apr, 2010.

[12] Besl, P. J., & McKay, N. D. "Method for registration of 3-D shapes," Pattern Analysis and Machine Intelligence, IEEE Transactions on, vol. 14, no. 2, pp. 239-256, Feb, 1992.

[13] Glover, F., & Kochenberger, G. A. "Handbook of metaheuristics," Springer Science & Business Media, 2003.

[14] Li, H., Qi, M., & Wu, Y. "A Real-Time Registration Method of Augmented Reality Based on Surf and Optical Flow," Journal of Theoretical and Applied Information Technology, vol. 42, no. 2, pp. 281-286, Aug, 2012.

[15] Wang, J., Suenaga, H., Hoshi, K., Yang, L., Kobayashi, E., Sakuma, I., & Liao, H. "Augmented Reality Navigation with Automatic Marker-Free Image Registration Using 3D Image Overlay for Dental Surgery," IEEE Trans Biomed Eng., vol. 61, no. 4, pp. 1295-1304, Apr, 2014.

[16] Vallino, J. R. "Interactive augmented reality," University of Rochester, 1998.

[17] Mohamed, M., & Deriche, M. "An Approach for ECG Feature Extraction using Daubechies 4 (DB4) Wavelet," International Journal of Computer Applications, vol. 96, no. 12, pp. 36-41, Jun, 2014.

[18] Jensen, A., & Cour-Harbo, A. "Ripples in mathematics: the discrete wavelet transform," Springer, 2001.

[19] Wold, S., Esbensen, K., & Geladi, P. "Principal component analysis," Chemometrics and intelligent laboratory systems, vol. 2, no. 1, pp. 37-52, Aug, 1987.

[20] Malinowski, E. R. "Statistical F-tests for abstract factor analysis and target testing," Journal of Chemometrics, vol. 3, no. 1, pp. 49-60, Jan, 1989.

[21] Jin, H., Favaro, P., & Soatto, S. "Real-time feature tracking and outlier rejection with changes in illumination," Computer Vision, 2001. Proceedings. Eighth IEEE International Conference on, pp. 684-689, Jul, 2001.

[22] Lucas, B. D., & Kanade, T. "An iterative image registration technique with an application to stereo vision," IJCAI, vol. 81, pp. 674-679, Aug, 1981.

[23] Shi, J., & Tomasi, C. "Good features to track," Computer Vision and Pattern Recognition, Proceedings IEEE Computer Society Conference on, pp. 593-600, Jun, 1994.

[24] Tavoli, R., & Mahmoudi, F. "PCA-Based Relevance Feedback in Document Image Retrieval," International Journal of Computer Science Issues, vol. 9, no. 4, Jul, 2012.

[25] Wang, B., & Bangham, J. A. "PCA based shape descriptors for shape retrieval and the evaluations," Computational Intelligence and Security, International Conference on, pp. 1401-1406, Nov, 2006.

[26] Jain, A., Muthuganapathy, R., & Ramani, K. "Content-based image retrieval using shape and depth from an engineering database," Advances in Visual Computing, Springer,.pp.255-264, Nov, 2007.

[27] Geladi, P., & Esbensen, K. "Regression on multivariate images: principal component regression for modeling, prediction and visual diagnostic tools," Journal of Chemometrics, vol. 5, no. 2, pp. 97-111, Mar, 2005.

[28] Wold, S. "Nonlinear partial least squares modelling II. Spline inner relation," Chemometrics and intelligent laboratory systems, vol. 14, no. 1, pp. 71-84, Apr, 1992.

Analysis and Prediction of Crimes by Clustering and Classification

Rasoul Kiani
Department of Computer Engineering, Fars Science and Research Branch, Islamic Azad University, Marvdasht, Iran

Siamak Mahdavi
Department of Computer Engineering, Fars Science and Research Branch, Islamic Azad University, Marvdasht, Iran

Amin Keshavarzi
Department of Computer Engineering, Marvdasht Branch, Islamic Azad University, Marvdasht, Iran

***Abstract*—Crimes will somehow influence organizations and institutions when occurred frequently in a society. Thus, it seems necessary to study reasons, factors and relations between occurrence of different crimes and finding the most appropriate ways to control and avoid more crimes. The main objective of this paper is to classify clustered crimes based on occurrence frequency during different years. Data mining is used extensively in terms of analysis, investigation and discovery of patterns for occurrence of different crimes. We applied a theoretical model based on data mining techniques such as clustering and classification to real crime dataset recorded by police in England and Wales within 1990 to 2011. We assigned weights to the features in order to improve the quality of the model and remove low value of them. The Genetic Algorithm (GA) is used for optimizing of Outlier Detection operator parameters using RapidMiner tool.**

Keywords—crime; clustering; classification; genetic algorithm; weighting; rapidminer

I. INTRODUCTION

A. Crime Analysis

Today, collection and analysis of crime-related data are imperative to security agencies. The use of a coherent method to classify these data based on the rate and location of occurrence, detection of the hidden pattern among the committed crimes at different times, and prediction of their future relationship are the most important aspects that have to be addressed.

In this regard, the use of real datasets and presentation of a suitable framework that does not be affected by outliers should be considered. Preprocessing is an important phase in data mining in which the results are significantly affected by outliers. Thus, the outlier data should be detected and eliminated though a suitable method. Optimization of Outlier Detection operator parameters through the GA and definition of a Fitness function are both based on Accuracy and Classification error. The weighting method was used to eliminate low-value features because such data reduce the quality of data clustering and classification and, consequently, reduce the prediction accuracy and increase the classification error.

The main purposes of crime analysis are mentioned below [1]:

- Extraction of crime patterns by crime analysis and based on available criminal information,
- Prediction of crimes based on spatial distribution of existing data and prediction of crime frequency using various data mining techniques,
- Crime recognition.

B. Clustering

Division of a set of data or objects to a number of clusters is called clustering. Thereby, a cluster is composed of a set of similar data which behave same as a group. It can be said that the clustering is equal to the classification, with only difference that the classes are not defined and determined in advance, and grouping of the data is done without supervision [2].

C. Clustering by K-means Algorithm

K-means is the simplest and most commonly used partitioning algorithm among the clustering algorithms in scientific and industrial software [3] [4] [5]. Acceptance of the K-means is mainly due to its being simple. This algorithm is also suitable for clustering of the large datasets since it has much less computational complexity, though this complexity grows linearly by increasing of the data points [5]. Beside simplicity of this technique, it however suffers from some disadvantages such as determination of the number of clusters by user, affectability from outlier data, high-dimensional data, and sensitivity toward centers for initial clusters and thus possibility of being trapped into local minimum may reduce efficiency of the K-means algorithm [6].

D. Classification

Classification is one of the important features of data mining as a technique for modeling of forecasts. In other words, classification is the process of dividing the data to some groups that can act either dependently or independently [7]. Classification is used to make some examples of hidden and future decisions on the basis of the previous decision makings [8]. Decision tree learning, neural network, nearest neighborhood, Nave Bayes method and support vector machine are different algorithms which are used for the purpose of classification [9].

E. Genetic Algorithm

In [10] S. Sindhiya and S. Gunasundari, have discussed about Genetic Algorithm (GA) as an evolutionary algorithm. "GA starts with an initial population called a candidate solution. After a sequence of iterations it achieves the optimal solution. The fitness is used to estimate the quality of each candidate solution. The chromosome, which has the highest fitness is to be kept in the next iteration. The crossover and mutation are the two basic operators of GA. The crossover is the procedure of taking above one parent solutions and generating a child solution. The mutation is used to preserve the genetic diversity from one iteration to the next iteration. And again the fitness function and the genetic operators are used to generate successive generations of individuals and are repeated several times until a suitable solution is found. The performance of GA depends on a number of issues such as crossover, mutation, fitness function and the various user determined parameters such as population size, probability of genetic operators."

The rest of the paper is organized as follows. Section 2 describes the existing systems for analyzing crimes. The New framework and experimental results are presented in section 3. Section 4 contains the conclusion. Finally, section 5 discusses the future scope of this paper.

II. LETRATURE REVIEW

J. Agarwal, R. Nagpal and R. Sehgal in [1] have analyzed crime and considered homicide crime taking into account the corresponding year and that the trend is descending from 1990 to 2011. They have used the k-means clustering technique for extracting useful information from the crime dataset using RapidMiner tool because it is solid and complete package with flexible support options. Figure1 shows the proposed system architecture.

Priyanka Gera and Dr. Rajan Vohra in [11] have used a linear regression for prediction the occurrence of crimes in Delhi (India). They review a dataset of the last 59 years to predict occurrence of some crimes including murder, burglary, robbery and etc. Their work will be helpful for the local police stations in decision making and crime supervision.

"After training systems will predict data values for next coming fifteen years. The system is trained by applying linear regression over previous year data. This will produce a formula and squared correlation(r^2).

The formula is used to predict values for comong future years. The coefficent of determination, r^2, is useful because is gives the proportion of variance of one variable that is predictable from other variable." Figure 2 shows the proposed system architecture.

In [12] an integrated system called PrepSearch have proposed by L. Ding et al. It has been combined using two separate categories of visualization tools: providing the geographic view of crimes and visualization ability for social networks. "It will take a given description of a crime, including its location, type, and the physical description of suspects (personal characteristics) as input.

To detect suspects, the system will process these inputs through four integrated components: geographic profiling, social network analysis, crime patterns and physical matching." Figure 3 shows the system design and process of PrepSearch.

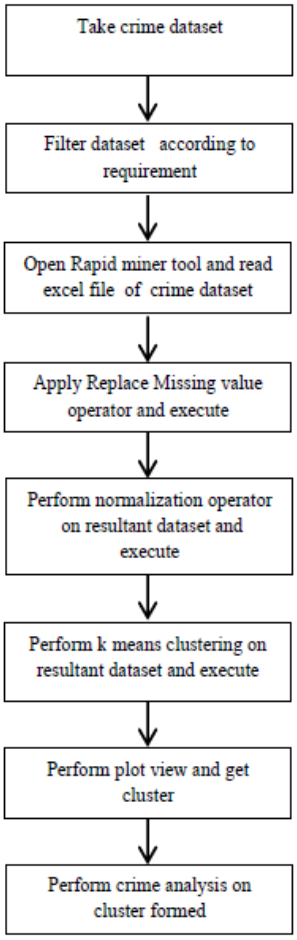

Fig. 1. Flow chart of crime analysis [1]

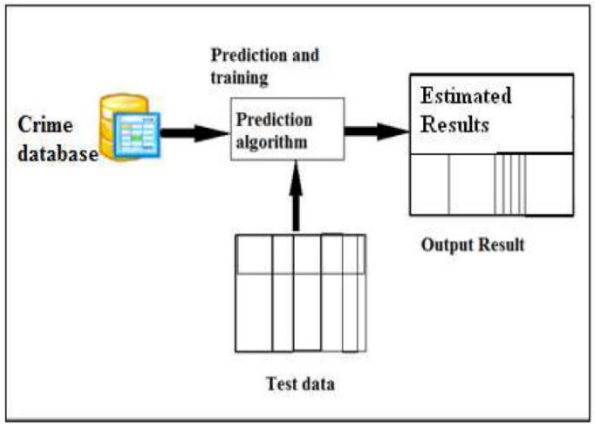

Fig. 2. Predicting future crime trends [11]

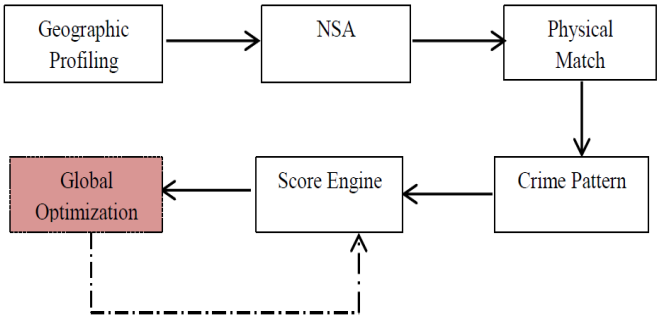

Fig. 3. System design and process of PrepSearch [12]

In [13] researches have introduced intelligent criminal identification system called ICIS which can potentially distinguish a criminal in accordance with the observations collected from the crime location for a certain class of crimes.

The system uses existing evidences in situations for identifying a criminal by clustering mechanism to segment crime data in to subsets, and the Nave Bayesian classification has used for identifying possible suspect of crime incidents. ICIS has been used the communication power of multi agent system for increasing the efficiency in identifying possible suspects. In order to describe the system ICIS is divided to user interface, managed bean, multi agent system and database. Oracle Database is used for implementing of database, and identification of crime patterns has been implemented using Java platform.

In [14] an improved method of classification algorithms for crime prediction has proposed by A. Babakura, N. Sulaiman and M. Yusuf. They have compared Naïve Bayesian and Back Propagation (BP) classification algorithms for predicting crime category for distinctive state in USA. In the first step phase, the model is built on the training and in the second phase the model is applied. The performance measurements such as Accuracy, Precision and Recall are used for comparing of the classification algorithms. The precision and recall remain the same when BP is used as a classifier.

In [15] researches have introduced crime analysis and prediction using data mining. They have proposed an approach between computer science and criminal justice to develop a data mining procedure that can help solve crimes faster. Also they have focused on causes of crime occurrence like criminal background of offender, political, enmity and crime factors of each day. Their method steps are data collection, classification, pattern identification, prediction and visualization.

III. NEW FRAMEWORK

In this section a new framework is introduced for clustering and prediction of cluster members to analyze crimes. A dataset of crimes recorded by police in England and Wales[1] within 1990 to 2011 has been used, and RapidMiner will be used for the purpose of implementation.

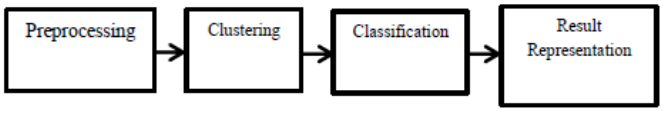

Fig. 4. New framework

A. Preprocessing Phase

1) Read the dataset of crime using Read Excel operator: The dataset selectd by the operator is read in RapidMiner tool.

2) Filter dataset according to requirement: Since there may be data in the read dataset that would not be used according to our method, the unnecessary data have to be filtered.

3) Apply Replace Missing Value operator: This operator replaces the dataset missing values with a new value, and adds it to our previous dataset. This can be done by one of the "Minimum", "Maximum", "Average" and "None" functions which is determined by the Default parameter. If "None" were selected, it will be leaded to no replacement. To achieve this purpose there is an accessible wizard using Column parameter.

Each one of these features chooses one of the functions through Column parameter. If one feature name were be shown as a key in the list, function name will be used as the key value. If the feature name does not exist in the list, a selected function with default parameters can be used for it. For nominal features the Mod function, nominal value that has been occurred the most in the dataset, can be replaced with the Average function as an example. For the nominal features which their replacement parameter has been assigned Zero for them, the first nominal defined value for the feature will be replaced with the missing values. We can also use the Replenishment Value parameter to specify the replacement values.

4) Outlier detection using Outlier Detection(Distance) operator: Outlier detection goals:

- Improving the quality of clusters in clustering phase,
- Increasing the accuracy of Decision tree in classification phase,
- Decreasing the classification error in classification phase.

This operator tries to detect outliers in the dataset according to their distance with their neighbors. This operator discovers outliers by a kind of search that can be known as a statistical search. This method starts the search according to the distance of K-th nearest neighbors, and then it tries to sort the search result by their local position. The ones which are farther than their K-th nearest neighbor will be specified as the outlier in the dataset more probably. Theory says dispersion and distance of outliers is more than the average of dataset. Then according to the distance of each data with its K-th nearest neighbor, all data will be ranked and then we can say the higher ranking shows the outlier of the dataset.

[1] www.gov.uk/government/publications/offences

Parameters:

- Number of neighbors: Specifies the value for the k-th nearest neighbors,
- Number of outliers: The number of top-n outliers need to be looked for.

5) Outlier Distance operator parameters optimization using GA: At this point, as shown in Figure 5, given that the process of optimizing the Outlier Detection operator parameters must improve the results of the predicted cluster members in the clusters, parameters of Accuracy and Classification error are used to define the fitness function

Optimize Parameters (Evolutionary) operator values:

- Max generation= 50
- Population size= 5
- Crossover prob= 0.9

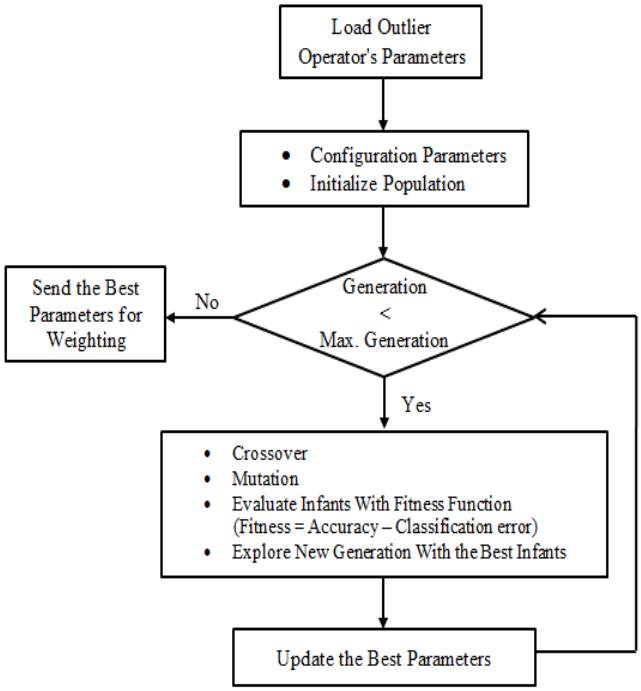

Fig. 5. Genetic algorithm for optimizing

6) Store a new dataset: After applying the changes, the dataset is stored for further use.

B. Clustering Phase

1) Apply Weight by Deviation operator: One of the clustering algorithm challenges is high-dimensional data, so to deal with this challenge is using weighted features and removing low-value featuers. A suitable operator to apply our idea is Weight by Deviation. It creates weights from the standard deviations of all featuers. The values can be normalized by the "Average", "Minimum", or "Maximum" of the featuers.

Parameters:

- Normalize weights: Activates the normalization of all weights,
- Normalize: Indicates that the standard deviation should be divided by the minimum, maximum, or average of the featuers.

2) Thershold selection: There is not specific critria for selecting the threshold. It is selected based on the Trial and error method for removing low-value featuers. The threshold is determined, and all the featuers, that their values are equal or less than it, will be removed from the dataset.

3) Store a new dataset: After applying the changes, the dataset is stored for further use.

4) Performe K-means algorithm on result dataset: At this step, the clustering process is carried out on the dataset using K-means operator.

5) Enable K-means Operator Parameters: The classification process is performed on the data after data clustering; therefore, the target class is defined in this step. The goal is that the cluster obtained in the previous step be defined as the target class. The k-means operator parameters are used for this purpose.

Parameters:

- Add cluster attribute: If enabled, a cluster id is generated as new special attribute directly in this operator. Othrwise this operator does not add an id attribute,
- Add as label: If true, the cluster id is stored in an attribute with the special role "label" instead of "cluster".

C. Classification Phase

1) Training and Testing Data: In this phase production of training and testing data is done using Sample (Stratified) and Set Minus operators for increasing confidence in the response without replacement.

- Sample operator is used to reserve 10% of data,
- Set Minus operator is used to reduce training data from the dataset.

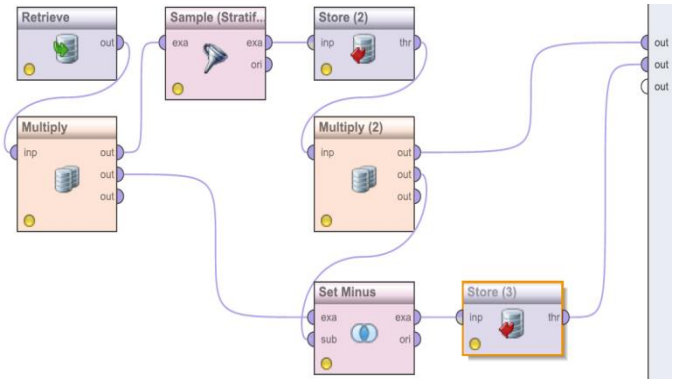

Fig. 6. Production of training and testing data

2) Decision Tree: We use Decision Tree operator to learn decision tree model, and the value of Criterion parameter is selected "gini_index".

3) Apply the model and test data: The model and test data have been produced in the previous steps are applied on Apply Model operator inputs to predict the cluster members.

D. Result Presentation Phase

At this phase, the following operators are used to show the results obtained from the presented framework.

- The model accuracy and classification error are calculated by Performance operators,
- Log operator is used to record and save performance report,
- A comparison of accuracy and classification error are used to evaluate the effect of optimization Outlier Detection operator parameters,
- Analysis of crimes based on the new framework.

Figure 7 shows the new framework scheme with details. Comparison between results in Table 1 shows that when the number of clusters is similar, after optimizing the parameters of the Outlier Detection operator, the classification accuracy increased and classification error decreased and, consequently, the obtained fitness function was optimized. Figure 8 shows the predicted occurrence rate for the crimes of buggery, homicide, and robbery. Also Figure 9 shows the implementation of the model by Rapid Miner tool.

TABLE I. RESULTS

Mode	Number of Cluster	Accuracy of Prediction	Classification Error	Fitness Function
Optimized	6	91.64%	8.36%	83.28
Non-Optimized	6	85.74%	13.26%	72.48

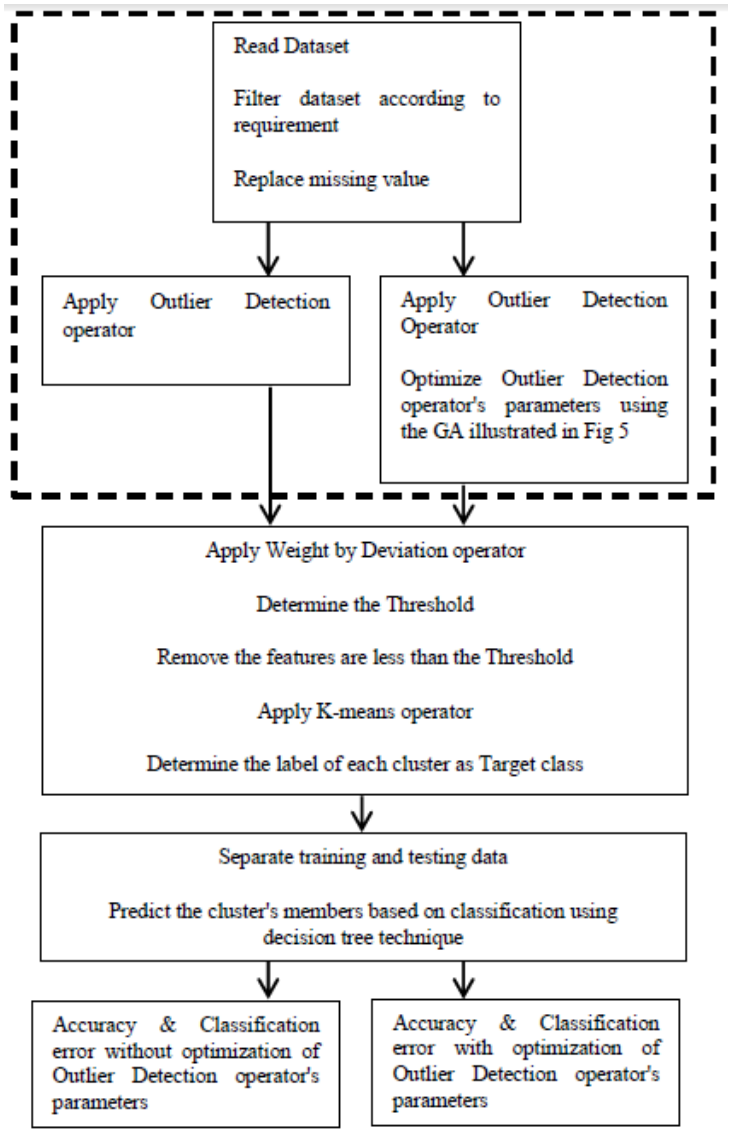

Fig. 7. The new framework scheme with details

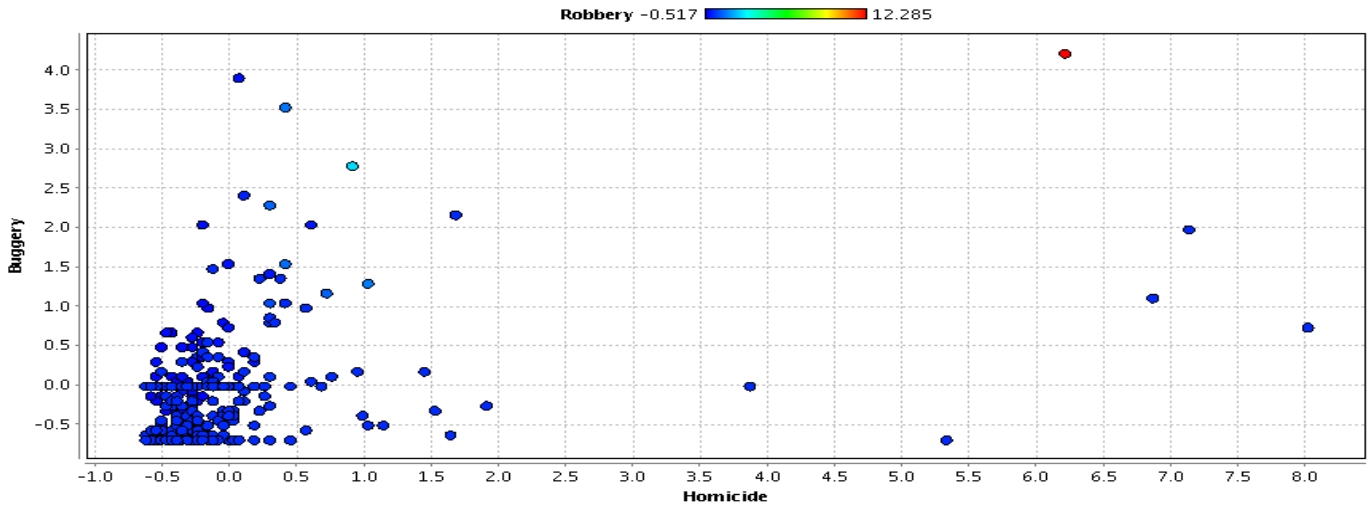

Fig. 8. Prediction of robbery, buggery and homicide

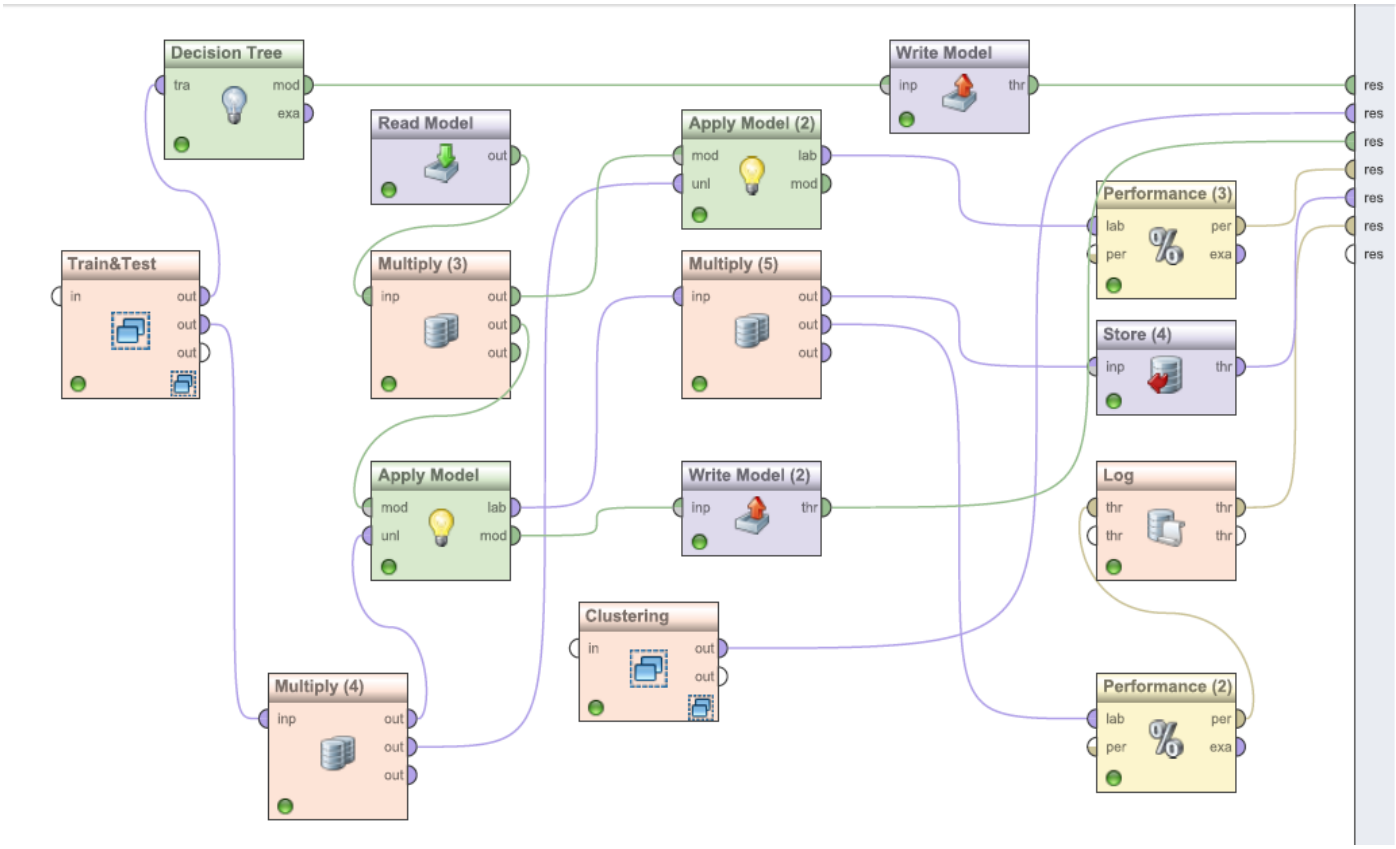

Fig. 9. Model for prediction of criems using decision tree

IV. Conclusion

This paper presents a new framework for clustering and predicting crimes based on real data. Examining the methods proposed for crime prediction shows that the parameters such as the effect of outliers in the data mining preprocessing, quality of the training and testing data, and the value of features have not been addressed before. In this framework, the GA was used to improve outlier detection in the preprocessing phase, and the fitness function was defined based on accuracy and classification error parameters. In order to improve the clustering process, the features were weighted, and the low-value features were deleted through selecting a suitable threshold. The proposed method was implemented, and the results of the optimized and non-optimized parameters were compared to determine their quality and effectiveness.

The main purposes of the new framework for clustering and classification of crimes are mentioned below:

- Generation of training and testing data,
- Removing low-value attributes using weighting technique to deal with high-dimensional data challenge,
- Optimization of Outlier operator parameters using GA.

V. Future Scope

One of the most important issues that should be addressed in the model presented in this paper to improve the clustering process and crime detection is the optimization of the number of clusters in the clustering process and the optimization of the technique used in the prediction phase of model development.

Acknowledgment

Hereby, we would like to kindly acknowledge sincere cooperation and valuable instructions of Mr. Mojtaba Montazeri and Mr. Mohammad Sarabi.

References

[1] J. Agarwal, R. Nagpal, and R. Sehgal, "Crime analysis using k-means clustering," International Journal of Computer Applications, Vol. 83 – No4, December 2013.

[2] J. Han, and M. Kamber, "Data mining: concepts and techniques," Jim Gray, Series Editor Morgan Kaufmann Publishers, August 2000.

[3] P. Berkhin, "Survey of clustering data mining techniques," In: Accrue Software, 2003.

[4] W. Li, "Modified k-means clustering algorithm," IEEE Congress on Image and Signal Processing, pp. 616- 621, 2006.

[5] D.T Pham, S. Otri, A. Afifty, M. Mahmuddin, and H. Al-Jabbouli, "Data clustering using the Bees algorithm," proceedings of 40th CRIP International Manufacturing Systems Seminar, 2006.

[6] J. Han, and M. Kamber, "Data mining: concepts and techniques," 2nd Edition, Morgan Kaufmann Publisher, 2001.

[7] S. Joshi, and B. Nigam, "Categorizing the document using multi class classification in data mining," International Conference on Computational Intelligence and Communication Systems, 2011.

[8] T. Phyu, "Survey of classification techniques in data mining," Proceedings of the International Multi Conference of Engineers and Computer Scientists Vol. IIMECS 2009, March 18 - 20, 2009, Hong Kong.

[9] S.B. Kim, H.C. Rim, D.S. Yook, and H.S. Lim, "Effective Methods for Improving Naïve Bayes Text Classifiers," In Proceeding of the 7th Pacific Rim International Conference on Artificial Intelligence, Vol.2417, 2002.

[10] S. Sindhiya, and S. Gunasundari, "A survey on Genetic algorithm based feature selection for disease diagnosis system," IEEE International Conference on Computer Communication and Systems(ICCCS), Feb 20-21, 2014, Chermai, INDIA.

[11] P. Gera, and R. Vohra, "Predicting Future Trends in City Crime Using Linear Regression," IJCSMS (International Journal of Computer Science & Management Studies) Vol. 14, Issue 07Publishing Month: July 2014.

[12] L. Ding et al., "PerpSearch: an integrated crime detection system," 2009 IEEE 161-163 ISI 2009, June 8-11, 2009, Richardson, TX, USA.

[13] K. Bogahawatte, and S. Adikari, "Intelligent criminal identification system," IEEE 2013 The 8th International Conference on Computer Science & Education (ICCSE 2013) April 26-28, 2013. Colombo, Sri Lanka.

[14] A. Babakura, N. Sulaiman, and M. Yusuf, "Improved method of calssification algorithms for crime prediction," International Symposium on Biometrics and Security Technologies (ISBAST) IEEE 2014.

[15] S. Sathyadevan, and S. Gangadharan, "Crime analysis and prediction using data mining," IEEE 2014.

Locality of Chlorophyll-A Distribution in the Intensive Study Area of the Ariake Sea, Japan in Winter Seasons based on Remote Sensing Satellite Data

Kohei Arai 1
1Graduate School of Science and Engineering
Saga University
Saga City, Japan

***Abstract*—Mechanism of chlorophyll-a appearance and its locality in the intensive study area of the Ariake Sea, Japan in winter seasons is clarified by using remote sensing satellite data. Through experiments with Terra and AQUA MODIS data derived chlorophyll-a concentration and truth data of chlorophyll-a concentration together with meteorological data and tidal data which are acquired for 6 years (winter 2010 to winter 2015), it is found that strong correlation between the chlorophyll-a concentration and tidal height changes. Also it is found that the relations between ocean wind speed and chlorophyll-a concentration. Meanwhile, there is a relatively high correlation between sunshine duration a day and chlorophyll-a concentration. Furthermore, it is found that there are different sources of chlorophyll-a in the three different sea areas of Ariake Sea area in the back, Isahaya bay area, and Kumamoto offshore area.**

Keywords*—chlorophyl-a concentration; red tide; diatom; solar irradiance; ocean winds; tidal effect

I. INTRODUCTION

The Ariake Sea is the largest productive area of Nori (Porphyra yezoensis1) in Japan. In winters of 2012 and 2013, a massive diatom bloom occurred in the Ariake Sea, Japan [1]. In case of above red tides, bloom causative was Eucampia zodiacus[2]. This bloom has being occurred several coastal areas in Japan and is well reported by Nishikawa et al. for Harimanada sea areas [2]-[10]. Diatom blooms have recurrently occurred from late autumn to early spring in the coastal waters of western Japan, such as the Ariake Sea [11] and the Seto Inland Sea [12], where large scale "Nori" aquaculture occurs. Diatom blooms have caused the exhaustion of nutrients in the water column during the "Nori" harvest season. The resultant lack of nutrients has suppressed the growth of "Nori" and lowered the quality of "Nori" products due to bleaching with the damage of the order of billions of yen [3].

This bloom had been firstly developed at the eastern part of the Ariake Sea. However, as the field observation is time-consuming, information on the developing process of the red tide, and horizontal distribution of the red tide has not yet been clarified in detail. To clarify the horizontal distribution of red tide, and its temporal change, remote sensing satellite data is quite useful.

In particular in winter, almost every year, relatively large size of diatoms of *Eucampia zodiacus* appears in Ariake Sea areas. That is one of the causes for damage of *Porphyra yezoensis*. There is, therefore, a strong demand to prevent the damage from Nori farmers. Since 2007, *Asteroplanus karianus* appears in the Ariake Sea almost every year. In addition, *Eucampia zodiacus* appears in Ariake Sea since 2012. There is a strong demand on estimation of relatively large size of diatoms appearance, size and appearance mechanism).

The chlorophyll-a concentration algorithm developed for MODIS[3] has been validated [13]. The algorithm is applied to MODIS data for a trend analysis of chlorophyll-a distribution in the Ariake Sea area in winter during from 2010 to 2015 is made. Then chlorophyll-a distributions of three specific areas, Ariake Bay, Isahaya Bay and Kumamoto Offshore are compared. It is intended to confirm that the sources of the chlorophyll-a concentration are different each other of sea areas.

The major influencing factors of chlorophyll-a concentration are species, sea water temperature (sunshine duration a day), northern winds for convection of sea water, and tidal effect have to be considered. Therefore, the relations between chlorophyll-a concentration and tidal effects, ocean wind speed as well as sunshine duration a day are, then, clarified.

In the next section, the method and procedure of the experimental study is described followed by experimental data and estimated results. Then conclusion is described with some discussions.

[1] http://en.wikipedia.org/wiki/Porphyra

[2] http://www.eos.ubc.ca/research/phytoplankton/diatoms/centric/eucampia/e_zodiacus.html

[3] http://modis.gsfc.nasa.gov/

II. METHOD AND PROCEDURE

A. The Procedure

The procedure of the experimental study is as follows,

1) Gather MODIS data of the Ariake Sea areas together with the chlorophyll-a concentration estimation with the MODIS data,

2) Compare chlorophyll-a distribution of three different sea areas, Ariake Bay, Isahaya Bay and Kumamoto Offshore,

3) Gather the meteorological data which includes sunshine duration a day, ocean wind speed and direction, tidal heights,

4) Correlation analysis between MODIS derived chlorophyll-a concentration and geophysical parameters, ocean wind speed, sunshine duration a day, tidal heights is made.

B. The Intensive Study Areas

Fig.1 shows the intensive study areas in the Ariake Sea area, Kyushu, Japan.

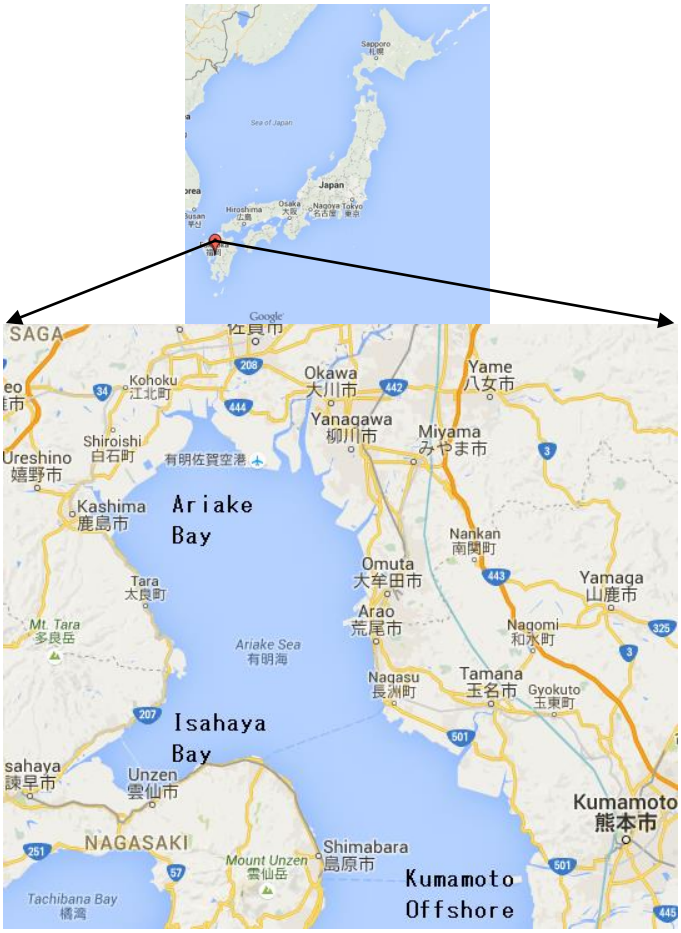

Fig. 1. Intensive study areas

III. EXPERIMENTS

A. The Data Used

MODIS derived chlorophyll-a concentrations which area acquired for the observation period of one month (January) in 2010 to 2015 are used for the experiments. Also, the meteorological data which includes sunshine duration a day, ocean wind speed and direction, tidal heights which are acquired for the same time periods as MODIS acquisitions mentioned above. In particular for 2015, two months January and February) data are used for trend analysis. Fig.2 shows the data used for two month period of time series MODIS derived chlorophyll-a concentrations in January and February, 2015. These data are acquired on January 4, 6, 7, 8, 9, 9[4], 10, 12, 17, 18, 20, 23, February 1, 3, 6, 9, 13, 14, 20, 27, and March 2 in 2015, respectively (from top left to bottom right in Fig.2). MODIS data are acquired on these days. MODIS data cannot be acquired on the rest of days due to cloudy condition. White portions in the chlorophyll-a concentration images are cloud covered areas.

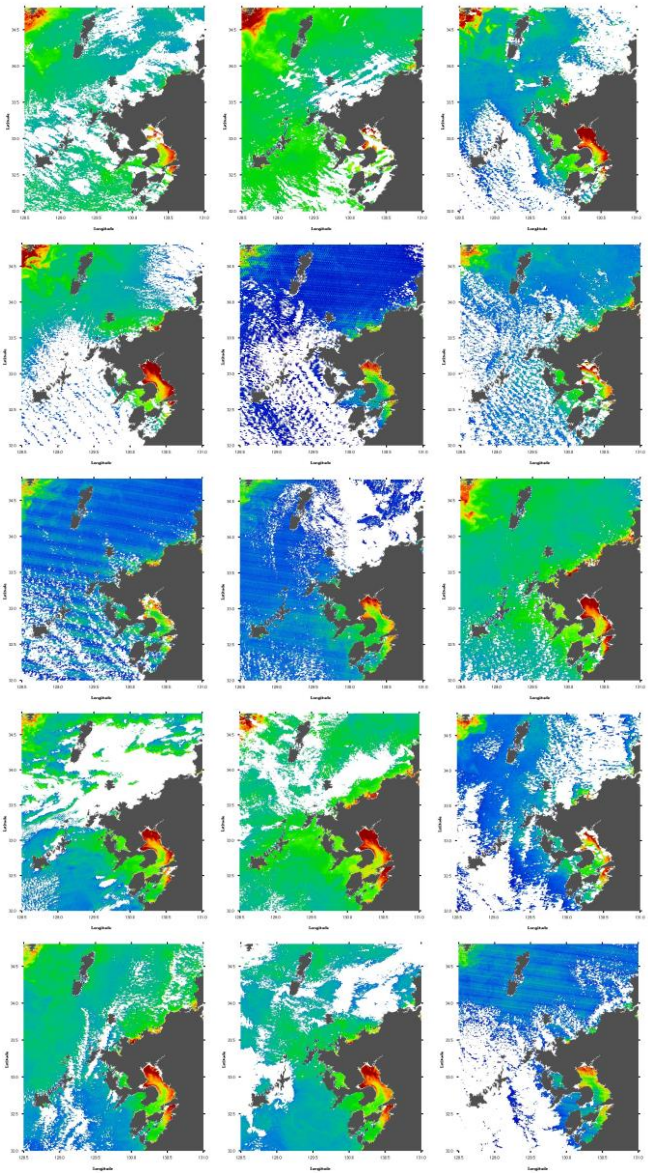

[4] There are two satellites which carry MODIS instruments, Terra and AQUA. Two MODIS data derived chlorophyll-a concentrations can be acquired occasionally.

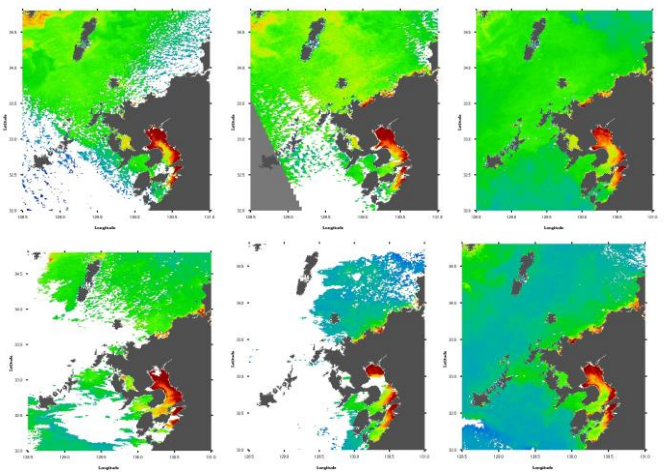

Fig. 2. MODIS data derived chlorophyll-a distribution in 2015

This time frame is red tide (Phytoplankton) blooming period. Such this MODIS derived chlorophyll-a concentration data are available almost every day except cloudy and rainy conditions.

Blooming is used to be occurred when the seawater becomes nutrient rich water, calm ocean winds, long sunshine duration after convection of seawater (vertical seawater current from the bottom to sea surface). Therefore, there must are relations between the geophysical parameters, ocean wind speed, sunshine duration, tidal heights and chlorophyll-a concentration.

As shown in Fig.2, it is clear that the diatom appeared at the back in the Ariake Sea, Ariake Bay and is not flown from somewhere else. Also, there is relatively low chlorophyll-a concentration sea areas between Isahaya Bay and Ariake Bay. Therefore, chlorophyll-a concentration variations are isolated each other (Isahaya Bay and Ariake Bay).

Fig.3 to Fig.7 also shows MODIS data derived chlorophyll-a concentrations in January 2014, 2013, 2012, 2011 and 2010, respectively. MODIS data are acquired on January 10, 13, 15, 16, 19, 23, 24, 26, 27, 29, 30 and February 4, respectively (from top left to bottom right in Fig.3).

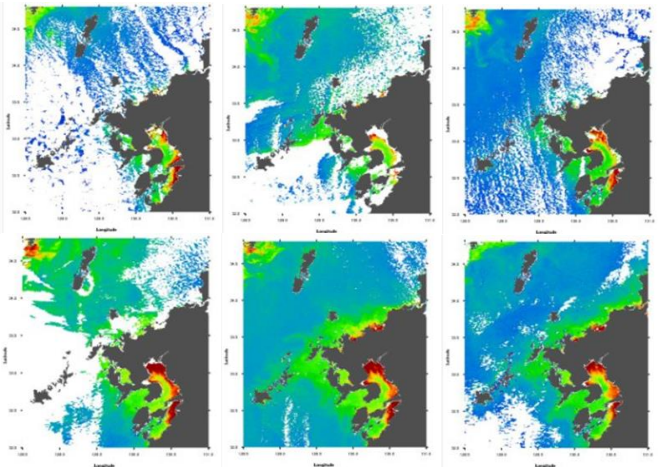

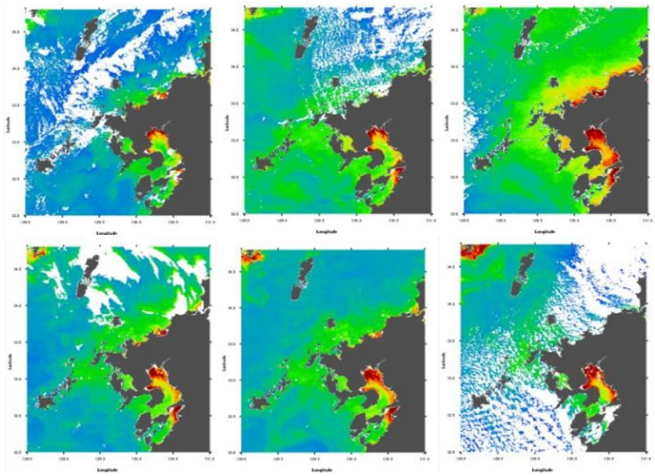

Fig. 3. MODIS data derived chlorophyll-a concentrations in 2014

Fig.4 shows the time series of MODIS data derived chlorophyll-a concentrations in 2013. MODIS data are acquired on January 4, 6, 10, 12, 15, 18, 19, 25, 28, 30, and 31, respectively (from top left to bottom right in Fig.4).

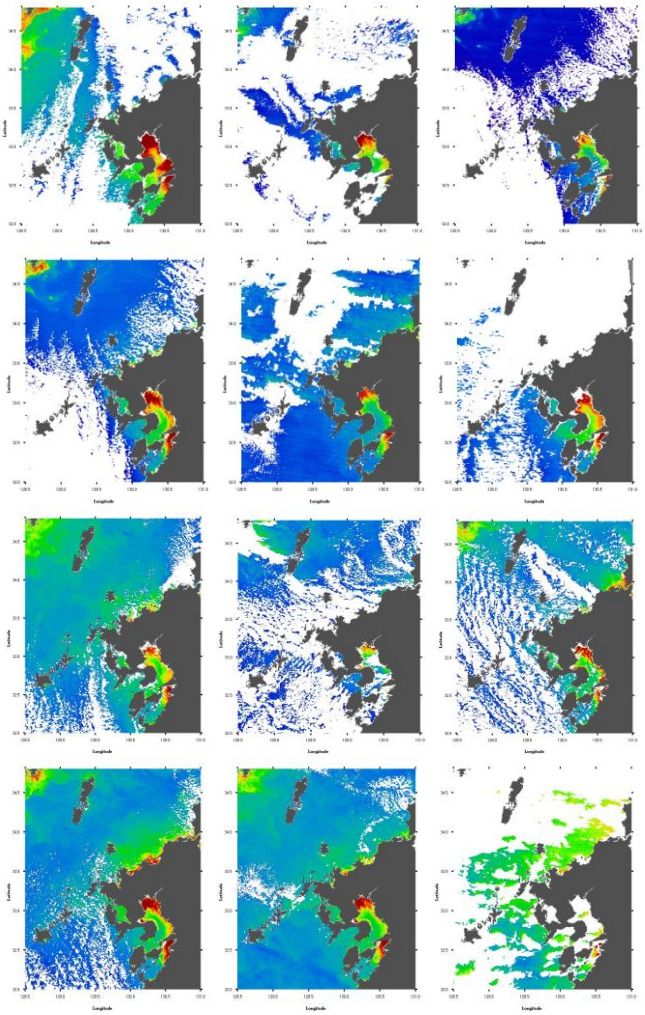

Fig. 4. MODIS data derived chlorophyll-a concentrations in 2013

Fig.5 also shows MODIS data derived chlorophyll-a concentrations acquired in 2012. MODIS data are acquired on January 2, 6, 7, 12, 17, 20, 21, 23, 26, 29, 30, and 31, respectively (from top left to bottom right in Fig.5).

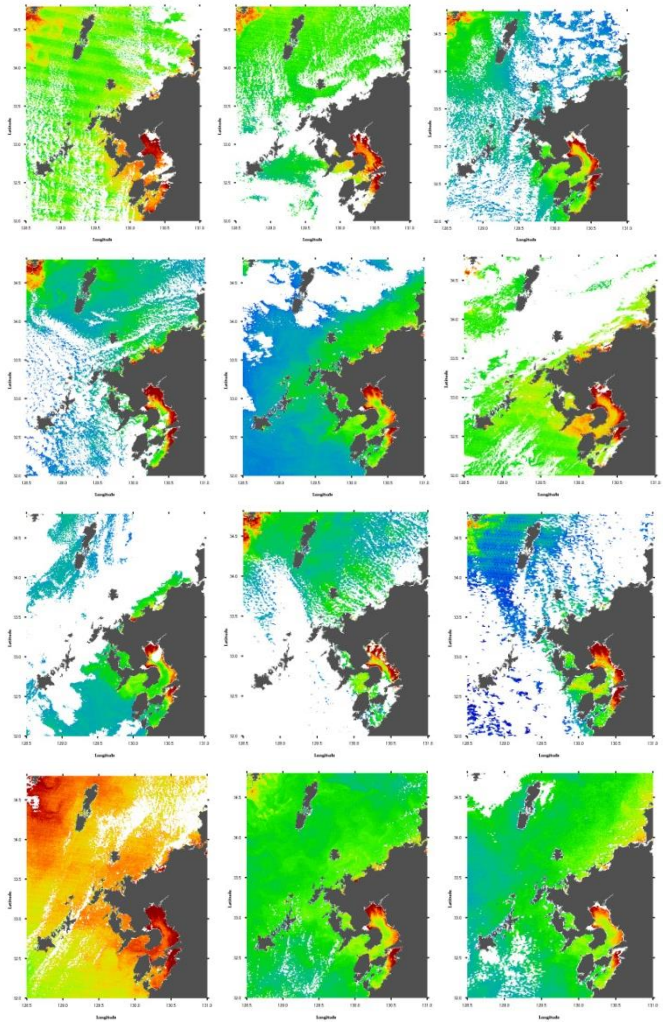

Fig. 5. MODIS data derived chlorophyll-a concentrations in 2012

Fig.6 shows the time series of MODIS data derived chlorophyll-a concentrations in 2011. MODIS data are acquired on January 1, 2, 7, 8, 14, 17, 22, 26, and 27, respectively (from top left to bottom right in Fig.6).

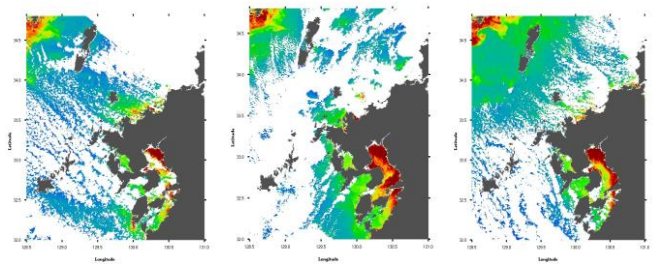

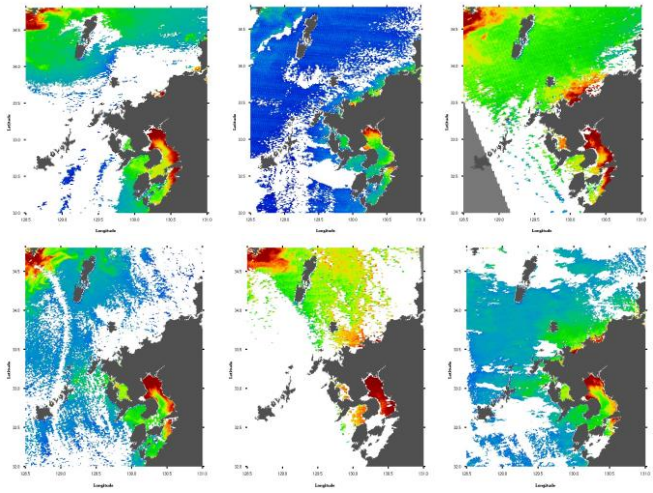

Fig. 6. MODIS data derived chlorophyll-a concentrations in 2011

Fig.7 shows the time series of MODIS data derived chlorophyll-a concentrations in 2011. MODIS data are acquired on January 1, 2, 9, 14, 16, 17, 18, 22, 24, 26, 27, 29, respectively (from top left to bottom right in Fig.7).

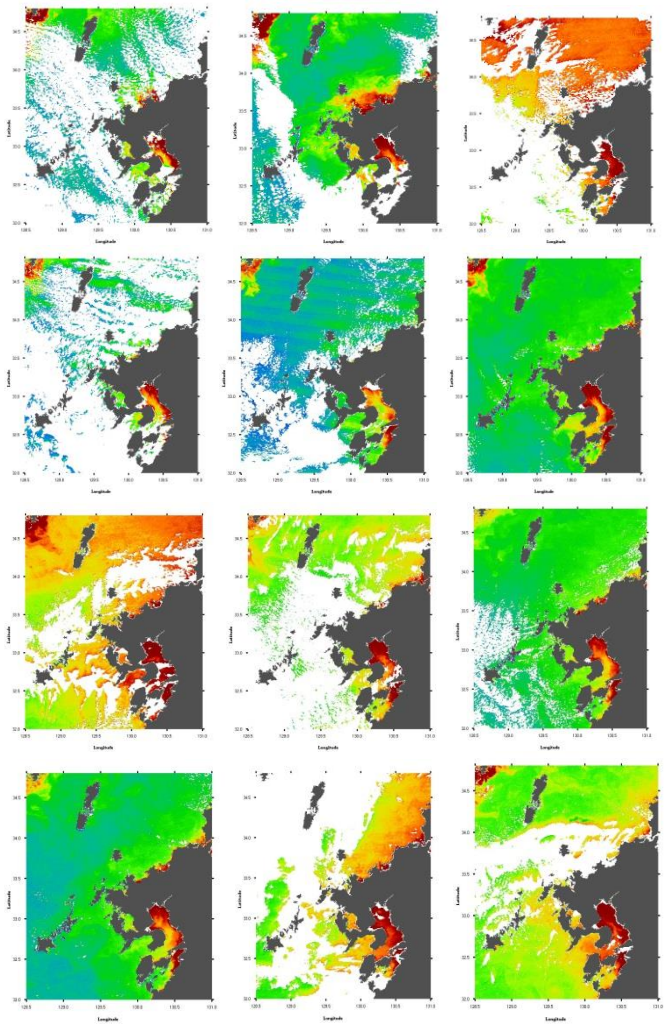

Fig. 7. MODIS data derived chlorophyll-a concentrations in 2010

B. Trends of Chlorophyll-a Concentration in Ariake Bay Area as well as Tidal Hieght, Solar Direct Irradiation, and Wind Speed from North

Fig.8 (a) to (f) shows trends of chlorophyll-a concentration in Ariake Bay area as well as tidal height difference a day, solar direct irradiance and wind speed from the North in 2015, 2014, 2013, 2012, 2011 and 2010, respectively. Typical trend is that chlorophyll-a concentration is increased in accordance with the tidal height difference a day it is not always true though. The reason for this is the following, namely, (1) chlorophyll appears in around sea bottom because nutrition rich water is situated in around sea bottom, (2) chlorophyll moves up to sea surface due to tidal effect (from the neap to the spring tide).

This fact is not always true. For instance, chlorophyll is not increased at the spring tide (35 days in the begging of February in 2015 and 12 days in January in 2012). In such cases, wind speed from the north is relatively strong and solar irradiance is not so high. This implies that sea water is mixed up between sea surface and sea bottom due to convection caused by relatively strong wind. Also it is implied that sea surface temperature is not getting warm because solar irradiance is weak results in decreasing of chlorophyll-a concentration.

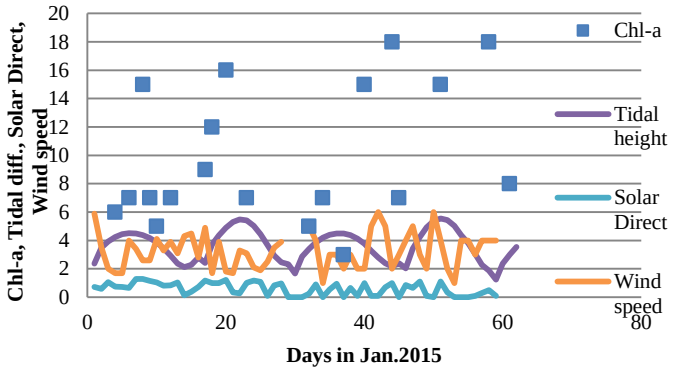

(a) 2015

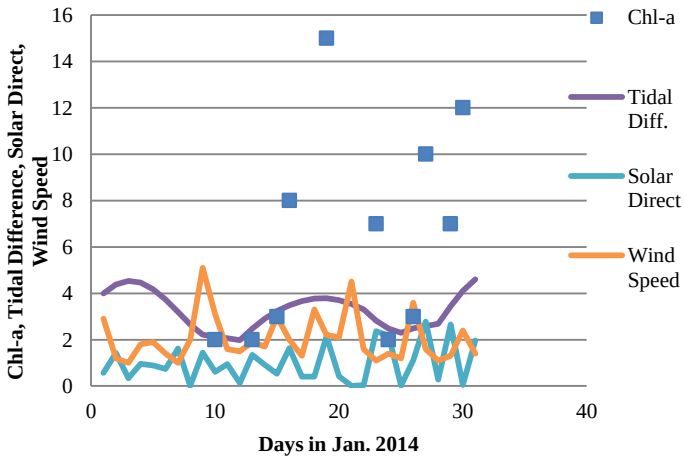

(b) 2014

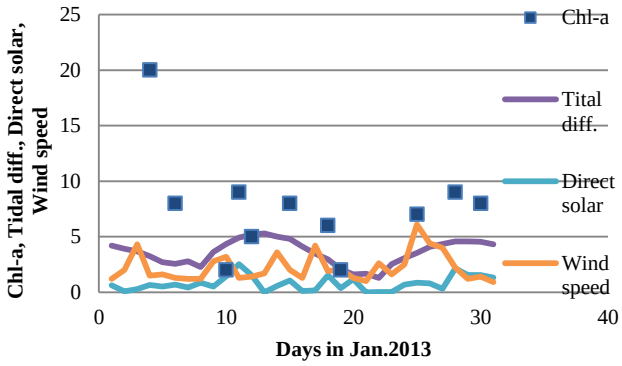

(c) 2013

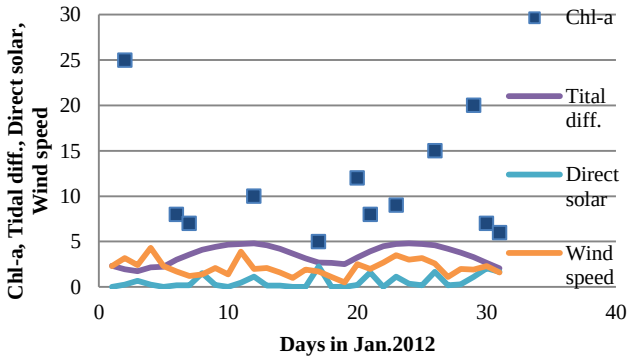

(d) 2012

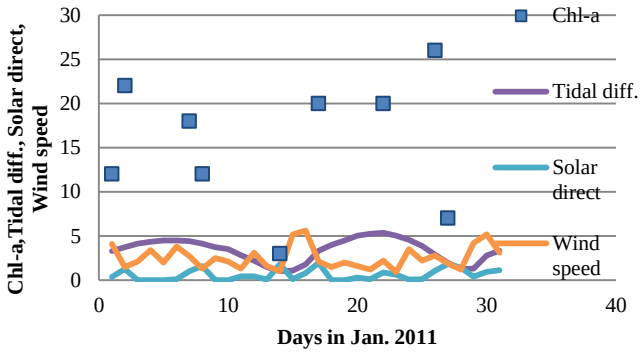

(e) 2011

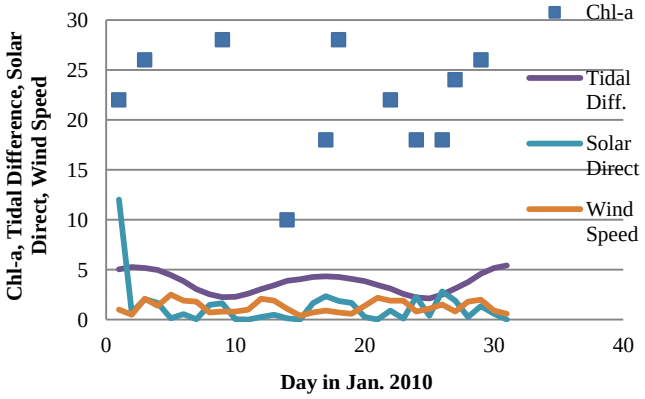

(f) 2010

Fig. 8. Trends of chlorophyll-a concentration in Ariake Bay area as well as tidal height, solar direct irradiance and wind speed from the North

C. *Locality of Chlorophyll-a Concentration in Ariake Bay, Isahaya Bay and Kumamoto Offshore Areas*

In order to make sure that the sources of the chlorophyll-concentrations of the three different sea areas, Ariake Bay, Isahaya Bay and Kumamoto Offshore are different each other, trends of chlorophyll-a concentration of three sea areas are compared. Fig.9 (a) to (f) shows the calculated trends for the year of 2010 to 2015. Although these trends are very similar due to the fact that nutrition condition and weather condition are almost same in the Ariake Sea area, the chlorophyll-a concentrations of these sea areas shows somewhat different trends each other in detail. Therefore, it may say that the sources of the chlorophyll-a concentration are different.

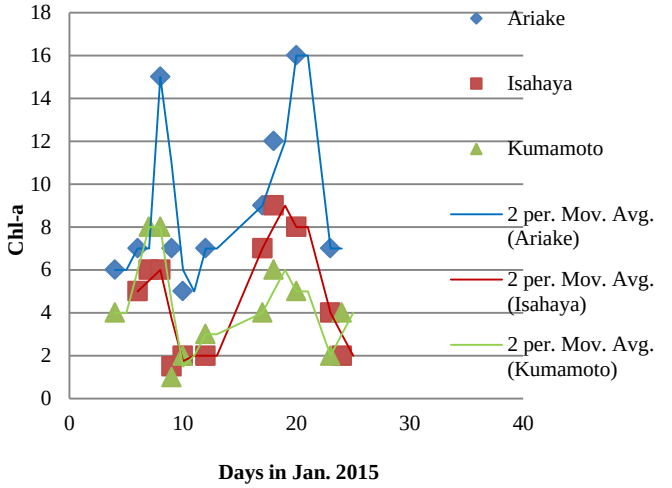

(a) 2015

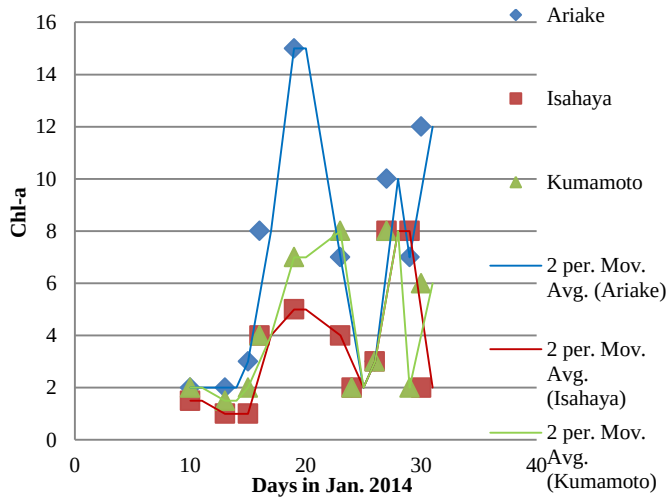

(b) 2014

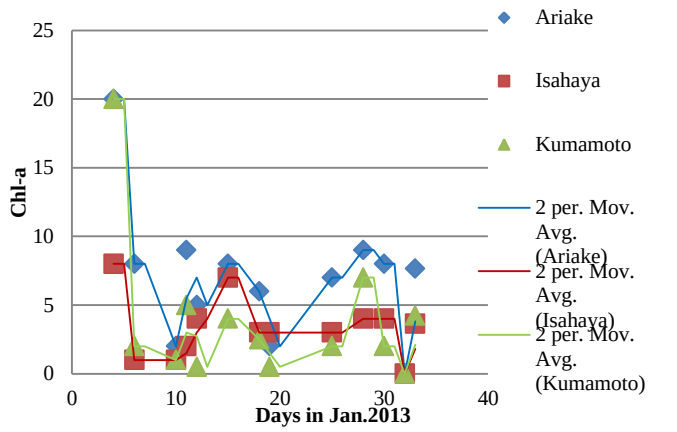

(c) 2013

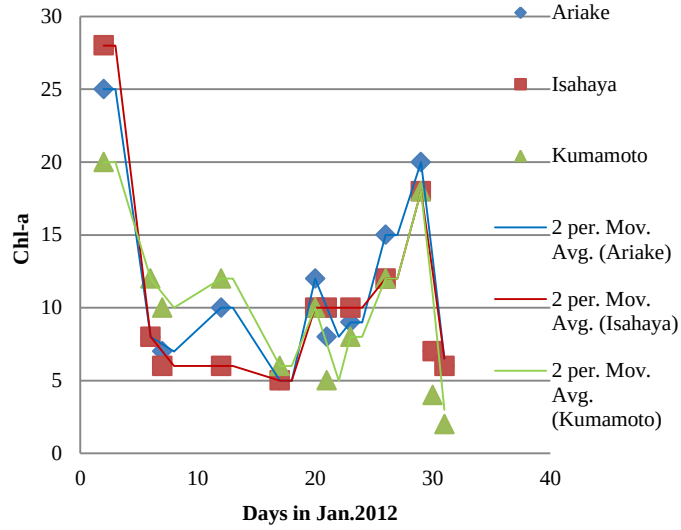

(d) 2012

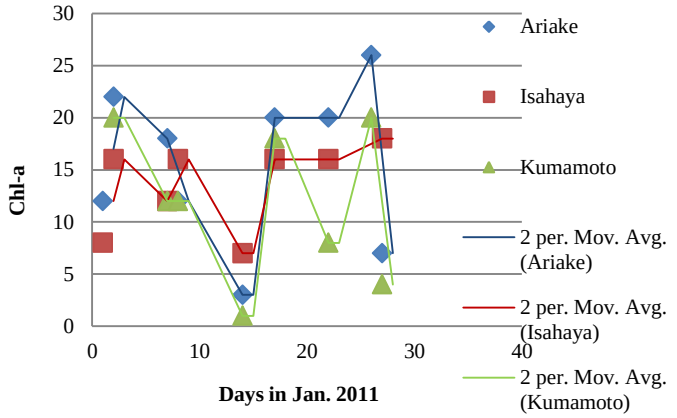

(e) 2011

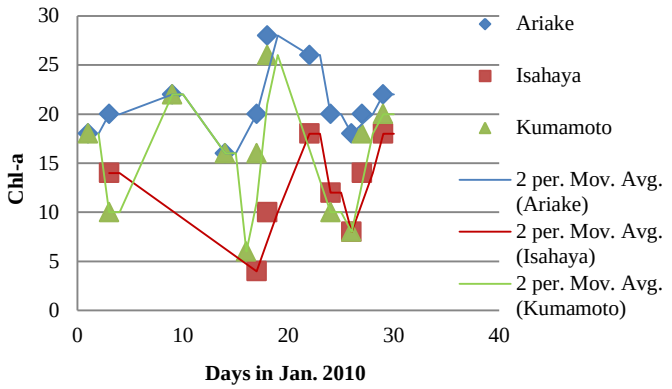

(f) 2010

Fig. 9. Trends of chlorophyll-a concentrations at three intensive test sites

As is mentioned before, these three trends are very similar due to the fact that nutrition condition and weather condition are almost same in the Ariake Sea area. Therefore, monthly mean of chlorophyll-a concentrations of three sea areas show almost same trends as shown in Fig.10.

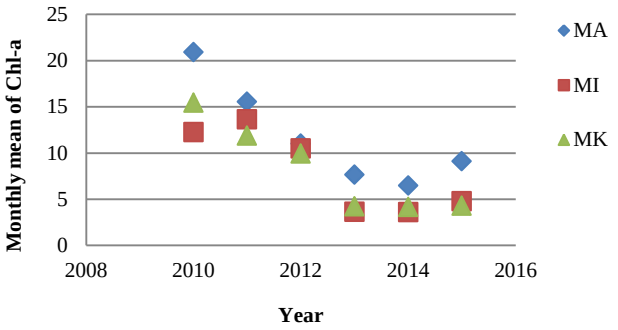

Fig. 10. Monthly mean of chlorophyll-a concentrations of three sea areas

Also, correlations of chlorophyll-a concentration of three different sea areas are very similar as shown in Fig.11.

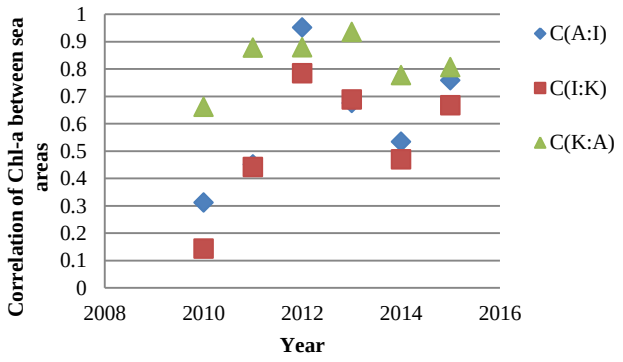

Fig. 11. Correlations of chlorophyll-a concentrations of three different sea areas

D. *Correlations Between Chlorophyll-a Concentration and Meteorological Conditions for Three Different Sea Areas*

Fig.12 shows the correlations between chlorophyll-a concentration and the meteorological conditions, tidal difference a day, solar irradiance, wind speed from the north.

Correlation coefficients are calculated between chlorophyll-a concentration and the other data of tidal difference a day, sun shine time duration a day and wind speed from the north. The result shows that there is a strong relation between chlorophyll-a concentration and tidal difference a day, obviously followed by wind speed from the north.

It is not always true. The situation may change by year by year. In particular, there is clear difference between year of 2011 and the other years, 2012 to 2015. One of the specific reasons for this is due to the fact that chlorophyll-a concentration in 2011 is clearly greater than those of the other years. Therefore, clear relation between chlorophyll-a concentration and the other data of tidal difference a day, sun shine time duration a day and wind speed from the north cannot be seen. That is because of the fact that there is time delay of chlorophyll-a increasing after the nutrient rich bottom seawater is flown to the sea surface.

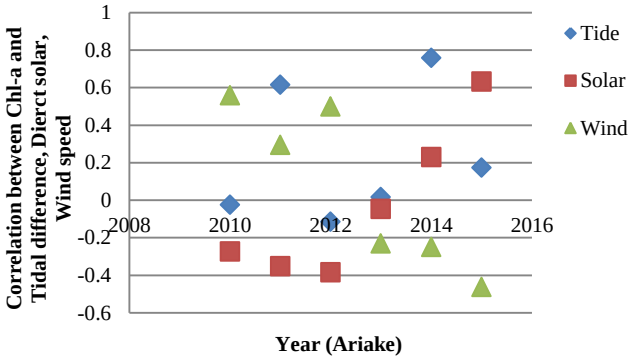

(a) Ariake

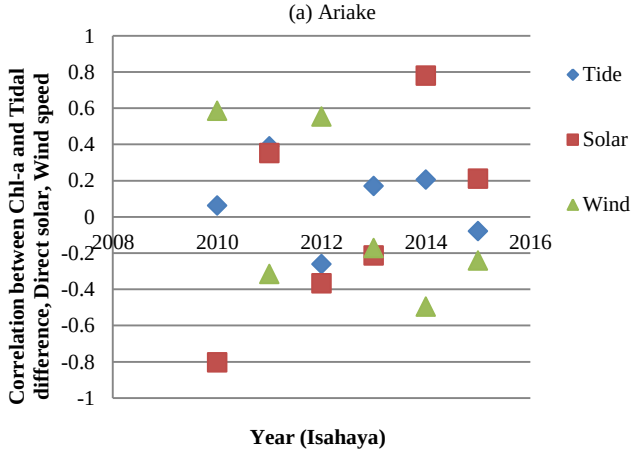

(b) Isahaya

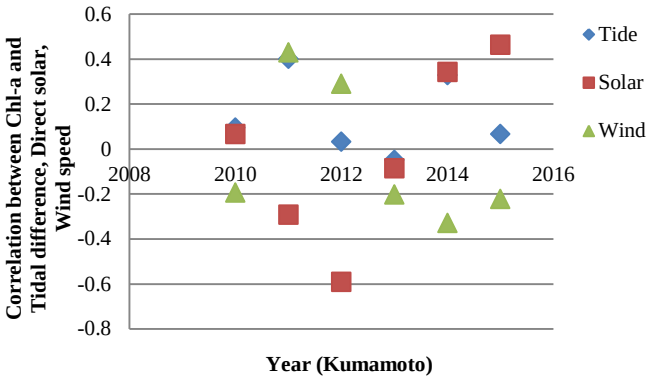

(c) Kumamoto

Fig. 12. Correlations between chlorophyll-a concentration and the meteorological conditions

IV. Conclusion

Through experiments with Terra and AQUA MODIS data derived chlorophyll-a concentration and meteorological data and tidal data which are acquired for 6 years (winter 2010 to winter 2015), it is found that strong relation between the chlorophyll-a concentration and tidal height changes. Also it is found that the relations between ocean wind speed and chlorophyll-a concentration. Meanwhile, there is a relatively high correlation between sunshine duration a day and chlorophyll-a concentration.

It is found that strong correlation between the truth data of chlorophyll-a and MODIS derived chlorophyll-a concentrations with R square value ranges from 0.677 to 0.791. Also, there is relatively low chlorophyll-a concentration sea area between Isahaya Bay and Ariake Bay. Therefore, chlorophyll-a concentration variation are isolated between both sea areas. Meantime, chlorophyll-a concentrations of Isahaya Bay, Ariake Bay and Kumamoto Offshore are different each other. It seems that chlorophyll-a concentrations at Isahaya Bay, Kumamoto Offshore and Ariake Bay are originated from the mouth of rivers while that of Kumamoto Offshore is migrated from the south.

Acknowledgment

The authors would like to thank Dr. Toshiya Katano of Tokyo University of Marine Science and Technology, Dr. Yuichi Hayami, Dr. Kei Kimura, Dr. Kenji Yoshino, Dr. Naoki Fujii and Dr. Takaharu Hamada of Institute of Lowland and Marine Research, Saga University for their great supports through the experiments.

References

[1] Yuji Ito, Toshiya Katano, Naoki Fujii, **Masumi Koriyama,** Kenji Yoshino, and Yuichi Hayami, Decreases in turbidity during neap tides initiate late winter large diatom blooms in a macrotidal embayment, Journal of Oceanography,69: 467-479. 2013.

[2] Nishikawa T (2002) Effects of temperature, salinity and irradiance on the growth of the diatom *Eucampia zodiacus* caused bleaching seaweed *Porphyra* isolated from Harima-Nada, Seto Inland Sea, Japan. Nippon Suisan Gakk 68: 356–361. (in Japanese with English abstract)

[3] Nishikawa T (2007) Occurrence of diatom blooms and damage tocultured *Porphyra* thalli by bleaching. Aquabiology 172: 405–410. (in Japanese with English abstract)

[4] Nishikawa T, Hori Y (2004) Effects of nitrogen, phosphorus and silicon on the growth of the diatom *Eucampia zodiacus* caused bleaching of seaweed *Porphyra* isolated from Harima-Nada, Seto Inland Sea, Japan. Nippon Suisan Gakk 70: 31–38. (in Japanese with English abstract)

[5] Nishikawa T, Hori Y, Nagai S, Miyahara K, Nakamura Y, Harada K, Tanda M, Manabe T, Tada K (2010) Nutrient and phytoplankton dynamics in Harima-Nada, eastern Seto Inland Sea, Japan during a 35-year period from 1973 to 2007. Estuaries Coasts 33: 417–427.

[6] Nishikawa T, Hori Y, Tanida K, Imai I (2007) Population dynamics of the harmful diatom *Eucampia zodiacus* Ehrenberg causing bleachings of *Porphyra* thalli in aquaculture in Harima- Nada, the Seto Inland Sea, Japan. Harmful algae 6: 763–773.

[7] Nishikawa T, Miyahara K, Nagai S (2000) Effects of temperature and salinity on the growth of the giant diatom *Coscinodiscus wailesii* isolated from Harima-Nada, Seto Inland Sea, Japan. Nippon Suisan Gakk 66: 993–998. (in Japanese with English abstract)

[8] Nishikawa T, Tarutani K, Yamamoto T (2009) Nitrate and phosphate uptake kinetics of the harmful diatom *Eucampia zodiacus* Ehrenberg, a causative organism in the bleaching of aquacultured *Porphyra* thalii. Harmful algae 8: 513–517.

[9] Nishikawa T, Yamaguchi M (2006) Effect of temperature on lightlimited growth of the harmful diatom *Eucampia zodiacus* Ehrenberg, a causative organism in the discoloration of *Porphyra* thalli. Harmful Algae 5: 141–147.

[10] Nishikawa T, Yamaguchi M (2008) Effect of temperature on lightlimited growth of the harmful diatom *Coscinodiscus wailesii*, a causative organism in the bleaching of aquacultured *Porphyra* thalli. Harmful Algae 7: 561–566.

[11] Syutou T, Matsubara T, Kuno K (2009) Nutrient state and nori aquaculture in Ariake Bay. Aquabiology 181: 168–170. (in Japanese with English abstract)

[12] Harada K, Hori Y, Nishikawa T, Fujiwara T (2009) Relationship between cultured *Porphyra* and nutrients in Harima-Nada, eastern part of the Seto Inland Sea. Aquabiology 181: 146–149. (in Japanese with English abstract)

[13] Arai K., T. Katano, Trend analysis of relatively large diatoms which appear in the intensive study area of the ARIAKE Sea, Japan, in winter (2011-2015) based on remote sensing satellite data, Internationa Journal of Advanced Research in Artificial Intelligence (IJARAI), 4, 7, to appear, 2015.

Authors Profile

Kohei Arai, He received BS, MS and PhD degrees in 1972, 1974 and 1982, respectively. He was with The Institute for Industrial Science and Technology of the University of Tokyo from April 1974 to December 1978 also was with National Space Development Agency of Japan from January, 1979 to March, 1990. During from 1985 to 1987, he was with Canada Centre for Remote Sensing as a Post Doctoral Fellow of National Science and Engineering Research Council of Canada. He moved to Saga University as a Professor in Department of Information Science on April 1990. He was a councilor for the Aeronautics and Space related to the Technology Committee of the Ministry of Science and Technology during from 1998 to 2000. He was a councilor of Saga University for 2002 and 2003. He also was an executive councilor for the Remote Sensing Society of Japan for 2003 to 2005. He is an Adjunct Professor of University of Arizona, USA since 1998. He also is Vice Chairman of the Commission "A" of ICSU/COSPAR since 2008. He wrote 34 books and published more thyan 510 journal papers. He is Edito-inChief of IJACSA and International Journal of Intelligent Systems and Applications. http://teagis.ip.is.saga-u.ac.jp/bib.html

Appropriate Tealeaf Harvest Timing Determination Referring Fiber Content in Tealeaf Derived from Ground based Nir Camera Images

Kohei Arai 1
Graduate School of Science and Engineering
Saga University
Saga City, Japan

Shihomi Kasuya [2],
2 Sasaki Green Tea Company,
Kakegawa city – Japan

Yoshihiko Sasaki [2],
2 Sasaki Green Tea Company,
Kakegawa city – Japan

Hideto Matusura [2]
2 Sasaki Green Tea Company,
Kakegawa city – Japan

***Abstract*—Method for most appropriate tealeaves harvest timing with the reference to the fiber content in tealeaves which can be estimated with ground based Near Infrared (NIR) camera images is proposed. In the proposed method, NIR camera images of tealeaves are used for estimation of nitrogen content and fiber content in tealeaves. The nitrogen content is highly correlated to Theanine (amid acid) content in tealeaves. Theanine rich tealeaves taste good. Meanwhile, the age of tealeaves depend on fiber content. When tealeaves are getting old, then fiber content is increased. Tealeaf shape volume also is increased with increasing of fiber content. Fiber rich tealeaves taste not so good, in general. There is negative correlation between fiber content and NIR reflectance of tealeaves. Therefore, tealeaves quality of nitrogen and fiber contents can be estimated with NIR camera images. Also, the shape volume of tealeaves is highly correlated to NIR reflectance of tealeaf surface. Therefore, not only tealeaf quality but also harvest amount can be estimated with NIR camera images. Experimental results show the proposed method works well for estimation of appropriate tealeaves harvest timing with fiber content in the tealeaves in concern estimated with NIR camera images.**

Keywords*—*Tealeaves; Nitrigen content; Amino accid; Leaf volume; NIR images; Fiber content; Theanine; Amid acid; Regressive analysis

I. INTRODUCTION

There is a strong demand for monitoring of the vitality of crops in agricultural areas automatically with appropriate measuring instruments in order to manage agricultural area in an efficient manner. It is also required to monitor not only quality but also quantity of vegetation in the farmlands. Vegetation monitoring is attempted with red and photographic cameras [1]. Grow rate monitoring is also attempted with spectral observation [2].

Total nitrogen content corresponds to amid acid which is highly correlated to Theanine: 2-Amino-4-(ethylcarbamoyl) butyric acid for tealeaves so that total nitrogen is highly correlated to tea taste. Meanwhile, fiber content in tealeaves has a negative correlation to tea taste. Near Infrared: NIR camera data shows a good correlation to total nitrogen and fiber contents in tealeaves so that tealeaves quality can be monitored with network NIR cameras. It is also possible to estimate total nitrogen and fiber contents in tealeaves with remote sensing satellite data, in particular, Visible and near infrared: VNIR radiometer data. Moreover, VC, NDVI, BRDF of tealeaves have a good correlation to grow index of tealeaves so that it is possible to monitor expected harvest amount and quality of tealeaves with network cameras together with remote sensing satellite data. BRDF monitoring is well known as a method for vegetation growth [3],[4]. On the other hand, degree of polarization of vegetation is attempted to use for vegetation monitoring [5], in particular, Leaf Area Index: LAI together with new tealeaves growth monitoring with BRDF measurements [6].

Theanine in new tealeaves are changing to Catechin [7],[8],[9] with sunlight. In accordance with increasing of sunlight, also, new tealeaves grow up so that there is a most appropriate time for harvest of tealeaves in order to maximize the amount and the taste of new tealeaves simultaneously.

Optical properties of tealeaves and methods for estimation of tealeaves quality and harvest amount estimation accuracy are well reported [10]-[17].

The method proposed here is to determine tealeaves harvest timing by using NIR camera images through the estimation of fiber content in tealeaves together with meteorological data. This paper, also, deals with automatic monitoring of a quality of tealeaves with earth observation satellite, network cameras together with a method that allows estimation of total nitrogen and fiber contents in tealeaves as an example.

The following section describes the proposed method together with some research background. Then experimental results are described followed by some tealeaves harvest timing related discussions. Finally, conclusions are described together with some discussions.

II. PROPOSED METHOD

The proposed method for most appropriate tealeaves harvest timing is based on Near Infrared (NIR) camera images of tealeaves which are acquired in tea farm areas. The most appropriate tealeaves harvest timing is difficult to define. Tea farmers determine the timing empirically. It may be defined as maximizing Theanine in tealeaves and harvest amount as well as softness of tealeaves (less fiber content).

Theanine is highly correlated to the nitrogen content in tealeaves. Nitrogen content in tealeaves is proportional to NIR reflectance of tealeaf surfaces. Meanwhile, harvest amount is proportional to leaf area of tealeaves which depends on NIR reflectance of tealeaf surfaces. Also, tealeaf thickness, length and width can be measured results in shape volume of tealeaves measurements. It is also crossly related to the harvest amount. For time being, tealeaves are getting old and fiber content is also increased accordingly. Such old tealeaves taste not so good. New fresh tealeaves which have less fiber and have much Theanine taste good. Due to the fact that there is relations between NIR reflectance of tealeaves and Theanine (Nitrogen), fiber (age), Theanine and fiber content in tealeaves and harvest amount can be estimated with NIR camera imagery data.

NIR reflectance can be obtained from the acquired NIR camera images if a standard reflectance panel or plaque is acquired simultaneously with tealeaves in concern. Standard panel, for instance Spectralon, is not so cheap. In order to minimize a required cost for acquisition of NIR camera images, typical print sheets are used as standard panel. Therefore, cross comparison of reflectance between Spectralon and the print sheet is needed. Fig.1 shows acquired NIR image of Spectralon and the print sheet. Correction curve for conversion of NIR reflectance with the print sheet to Spectralon based NIR reflectance can be obtained from the acquired reflectance measured for Spectralon and the print sheet.

Fig. 1. Acquired NIR image of Spectralon and the print sheet

Fig.2 shows the ratio of the Spectralon based NIR reflectance and the print sheet based NIR reflectance.

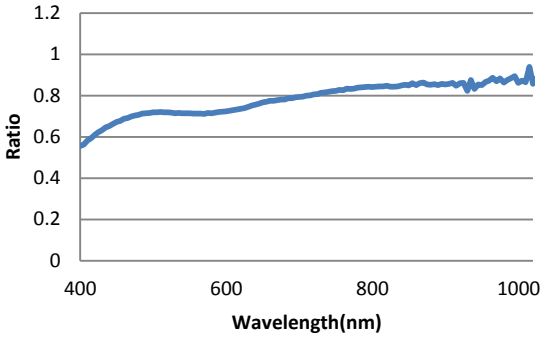

Fig. 2. Ratio of the Spectralon based NIR reflectance and the print sheet based NIR reflectance

III. EXPERIMENTS

A. Intensive Study Test Sites

Experiments are conducted at the tea farm areas of Kakegawa in Shizuoka prefecture, Japan in April and May time frame (first harvesting time period a year). Outlook of one of the typical tea farm areas which is called "Pilot farm area" is shown in Fig.3. Longitude and latitude of the Pilot tea farm area is as follows,

34°44'30.7"N 138°01'27.6"E

Fig. 3. Outlook of one of the typical tea farm areas which is called "Pilot farm area"

Other than Pilot tea farm area, there are other test sites, "Front" and "Back" which are situated the following longitude and latitude, respectively.

34°45'44.3"N 138°03'11.3"E(Front)

34°44'40.0"N 138°03'11.9"E(Back)

Usually, tealeaves are harvested three times, (1) begging in May, (2) middle in July, (3) middle in October. Therefore, tealeaves are growing in April and then tealeaves are harvested in the begging of May in general for the first harvesting time period. Fig.4 shows examples of NIR camera image of photos which are acquired before and after the

harvest. Fig.3 (a) and (b) shows an example of NIR camera image of tealeaves which is acquired just before harvest together with the print sheet and of tealeaves which is acquired just after harvest together with the same print sheet, respectively. In the experiments, the center wavelength of NIR camera is 800nm with band width of 100nm.

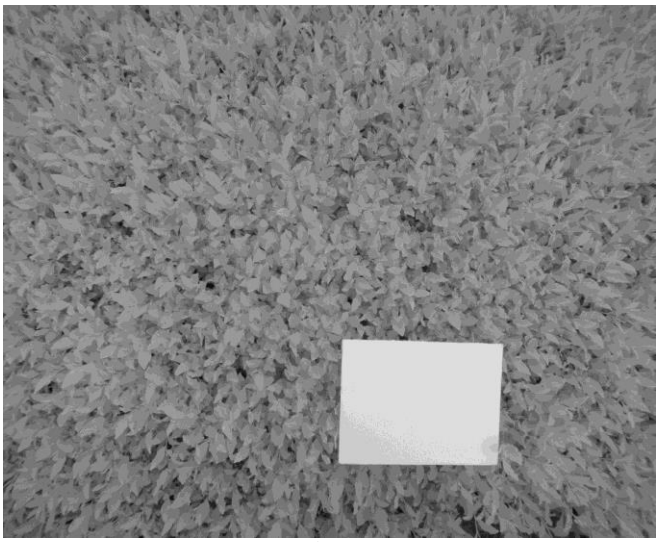

(a)Before harvest

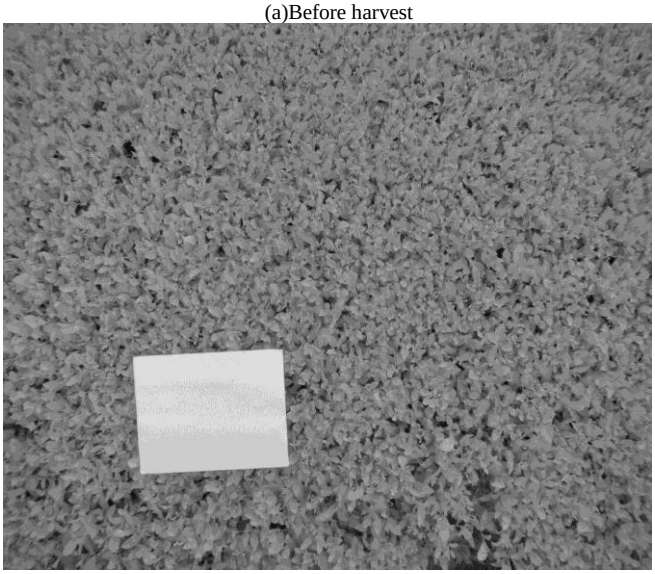

(b)After harvest

Fig. 4. Examples of NIR camera images which are acquired just before (a) and after (b) harvest of tealeaves together with the print sheet as secondly standard panel

Fig.5 shows examples of tealeaves and nadir view of tea farm areas of the intensive test sites, "Pilot", "Front" and "Back".

(a)Tealeaves in Pilot

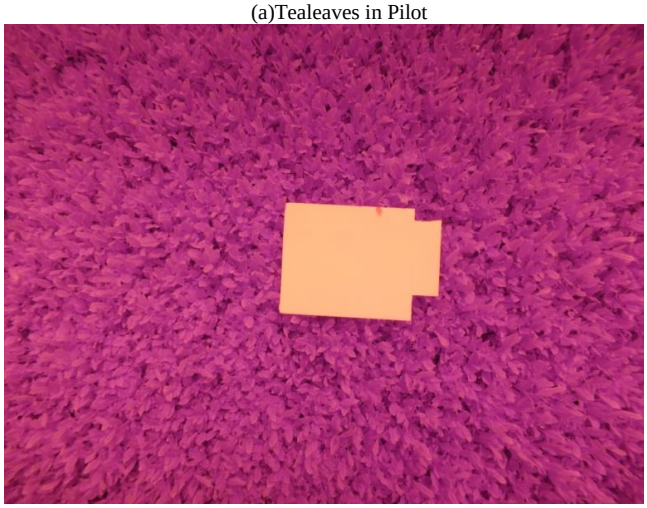

(b)Nadir view in Pilot

(c)Tealeaves in Front

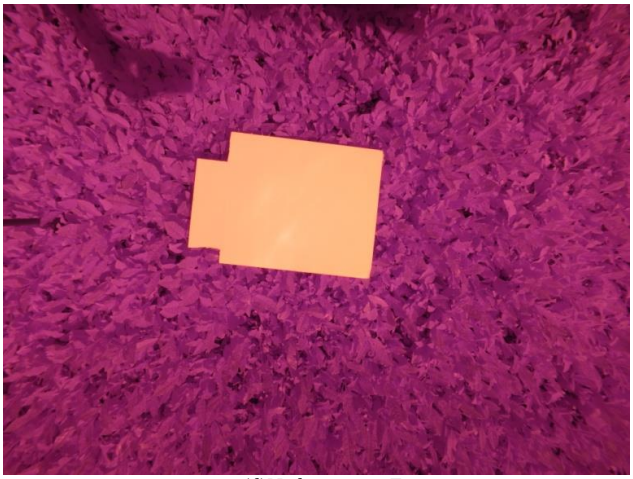

(d)Nadir view in Front

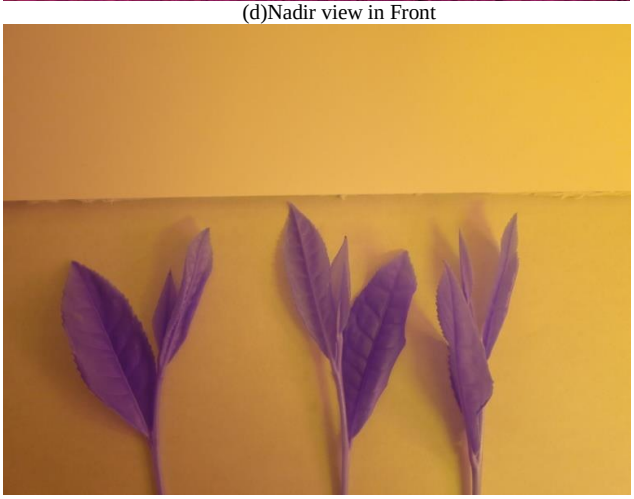

(e)Tealeaves in Back

(f)Nadir view in Back

Fig. 5. Example of the acquired NIR images for the three intensive test sites, Pilot, Front and Back of tea farm areas which are taken just before harvest, April 23, Mar 2 and May 3 in 2015, respectively

B. Relation between NIR Reflectance and TN and Fiber

Through the comparison of NIR reflectance measured in both time frames, it is found that Theanine which is proportional to the measured NIR reflectance is increased for the time being. Also, it is found that the Theanine is decreased for the short term periods (around one month). During the short term periods, tealeaf thickness (T), length (L), and width (W) are increased as shown in Fig.6 (a) and (b) shows the relation between NIR reflectance which is calculated with nadir view camera data and nitrogen and fiber contents in tealeaves. Although R square values are not so large, there are not so bad correlations between NIR reflection and nitrogen and fiber contents. There are positive and negative correlations between NIR reflectance and nitrogen as well as fiber contents, respectively. Trends of nitrogen and fiber contents in April 2015 are shown in Fig.7 (a) and (b), respectively. Fiber content is getting large while nitrogen content is getting small for the time being, obviously. These trends are different from each other tea farm areas.

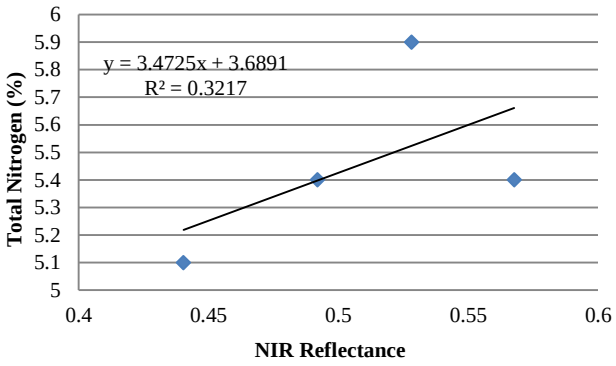

(a)Nitrogen

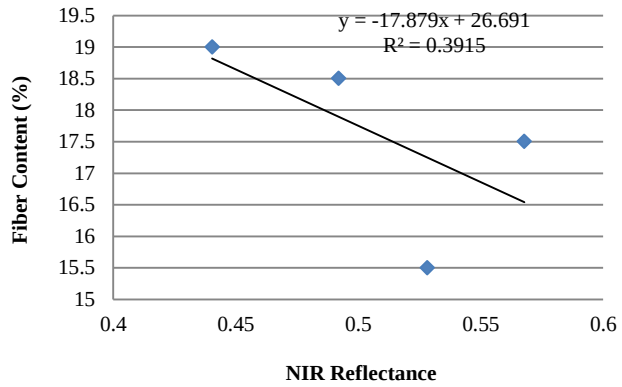

(b)Fiber

Fig. 6. Relation between NIR reflectance which is calculated with nadir view camera data and nitrogen and fiber contents in tealeaves

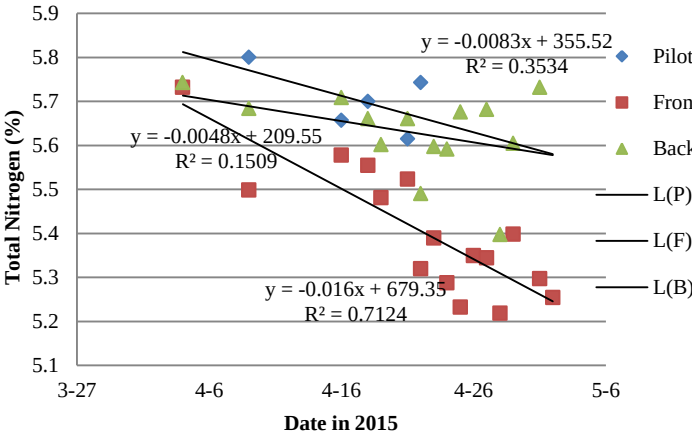

(a)Nitrogen

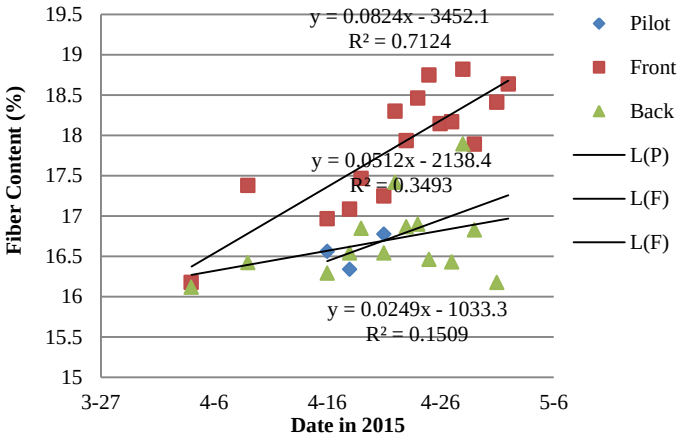

(b)Fiber

Fig. 7. Trends of nitrogen and fiber contents in April 2015

C. *Relation between TN and Fiber as well as Meteorological Data*

If the appropriate harvest timing is relating to the meteorological data, it is very convenient to determine the timing with the meteorological data. The harvest dates for the test sites of Pilot, Front and Back are April 23, May 2 and May3, respectively. These are determined by tea farmers in subjective manner. They used to determine the best harvest days through touching the typical top of tealeaves (softness of the tealeaves), and looking the shape of tealeaves, length, width, and thickness.

Fig.8 (a) shows the trends of the maximum air temperature on the ground a day (triangle), the sunshine duration time a day (cross) while Fig.8 (b) shows cumulative maximum air temperature (blue square) and cumulative sunshine duration time a day (brown square) since March 23 2015, respectively. Also, Fig.8 (c) shows the measured irradiance at the three test sites. Due to the fact that the harvest dates for the test sites of Pilot, Front and Back are April 23, May 2 and May3, respectively, these dates are coincident to the dates when the irradiance reaches to 10000 for each test site. These measured irradiances vary by day by day. 10000 arbitrary unit of measured irradiance is the maximum of the measurable irradiance range. In this case, the irradiance is measured when the tealeaf shape is measured together with the NIR camera data is taken.

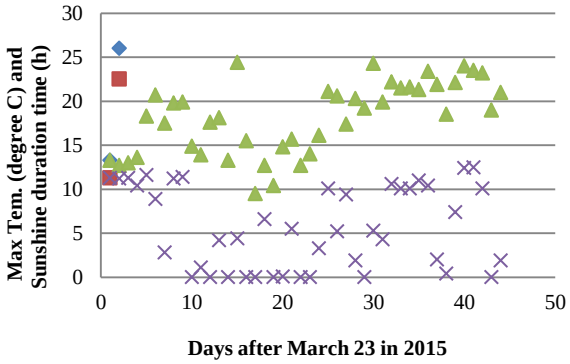

(a)Maximum air temperature a day and sunshine duration time a day

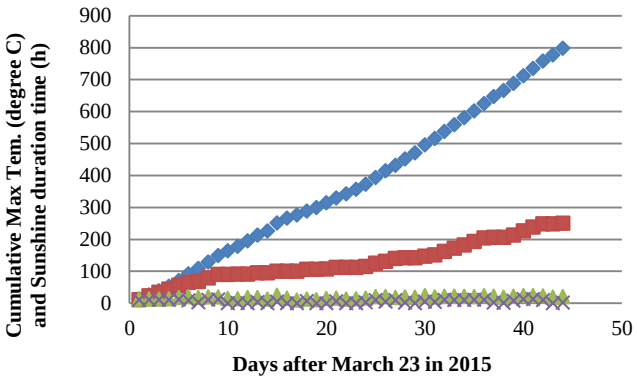

(b)Cumulative

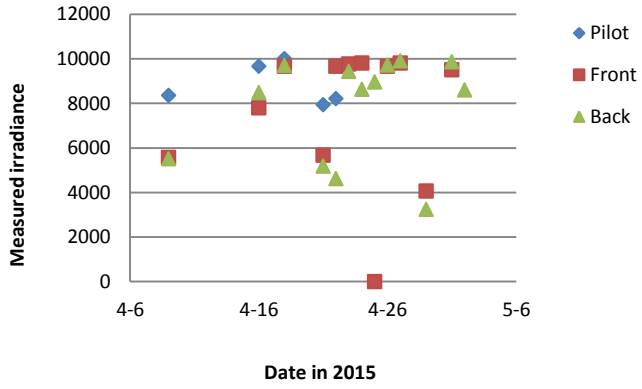

(c)Measured irradiance

Fig. 8. Maximum air temperature a day and sunshine duration time a day and cumulative those since March 23 2015

Fig.9 (a) and (b), meanwhile, shows nitrogen and fiber contents in tealeaves at the three test sites, Pilot, Front and Back as a function of cumulative maximum air temperature a day since March 23 2015, respectively. Also, Fig.9 (c) shows fiber content in tealeaves and the shape volume (width by length by thickness) at the test sites, Pilot, Front and Back. Due to the fact that the harvest day at the test site, Pilot is April 23 2015, there is only one data point of the measured shape volume while there are two data points for the test sites, Front and Back.

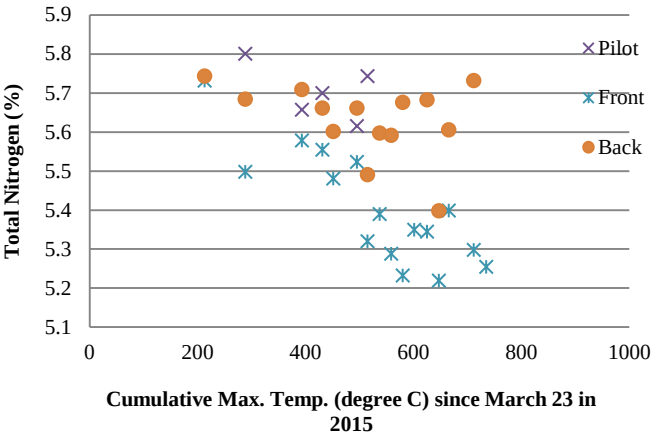

(a)Nitrogen

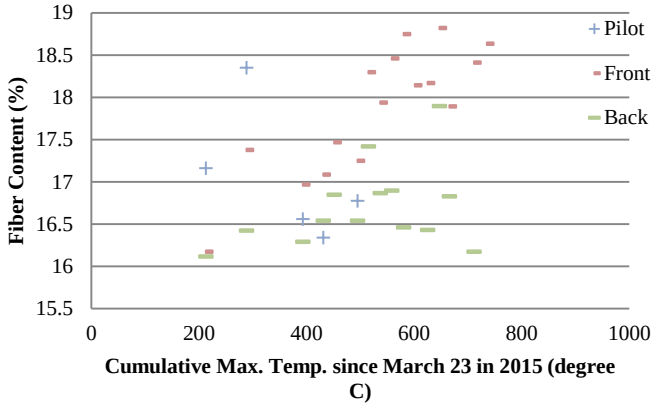

(b)Fiber

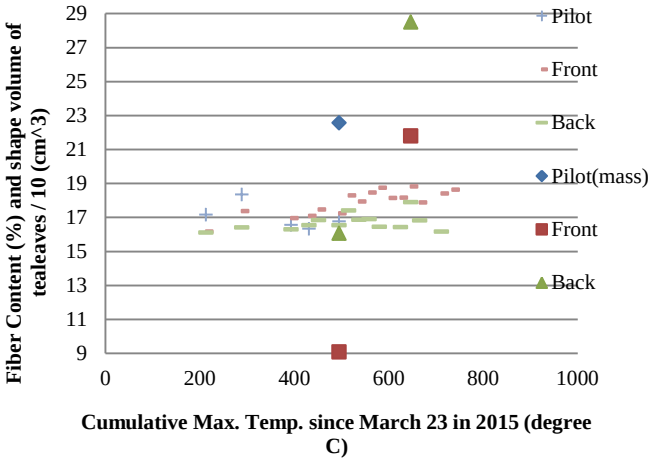

(c)Shape Volume

Fig. 9. Nitrogen and fiber contents in tealeaves at the test sites, Pilot, Front, Back tea farm areas

Although the harvest days for the different test sites, Pilot, Front, Back are different, the shape volumes at the harvest days are almost same (greater than 230 cm^3). It is not easy to measure the shape volume. Tea farmers used to measure the shape of tealeaves not so frequently because it takes time. On the other hand, it is not so difficult to take a NIR camera image for tea farmers. Also, as is aforementioned, the shape volume is proportional to fiber content and is negatively proportional to nitrogen content. Therefore, it seems reasonable to determine harvest day with nitrogen and fiber contents in tealeaves. The relations between leaf shape volume and nitrogen and fiber contents in tealeaves are shown in Fig.10. It is quite obvious that sensitivity of fiber content is greater than that of nitrogen content.

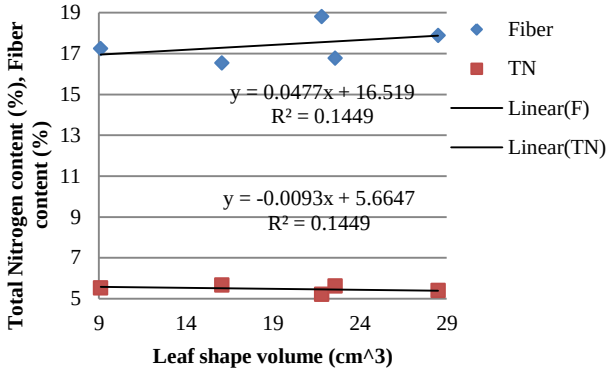

Fig. 10. relations between leaf shape volume and nitrogen and fiber contents in tealeaves

A relation between fiber content and cumulative maximum air temperature a day since March 23 2015 is estimated by using this relation of regressive equation. Fig.11 shows the relation between both.

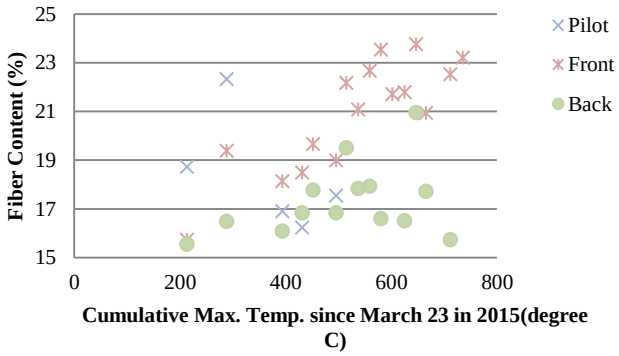

Fig. 11. Relation between fiber content and cumulative maximum air temperature a day since March 23 2015

From this figure, it is found that the harvest day can be determined by using fiber content in tealeaves with the threshold at around 23 (%). If the fiber content is greater than 23 (%), such tealeaves are no longer new fresh tealeaves and are getting down in terms of tealeaf quality (it tastes getting bad).

D. Estimation of Harvest Amount

Harvest amounts (Kg/a) of the test sites, Pilot, Front, and Back are 60.79, 93.4, 85.0, respectively. Harvest amount may be estimated with shape volume. Namely, it seems reasonable that large size of tealeaf shape means a great harvest amount. The other factor would be fiber content in tealeaves. Namely, in accordance with tealeaf age, fiber content is increased. This implies that harvest amount is increased with increasing of

fiber content. Fig.12 shows the relations between harvest amount and shape volume as well as fiber content in tealeaves.

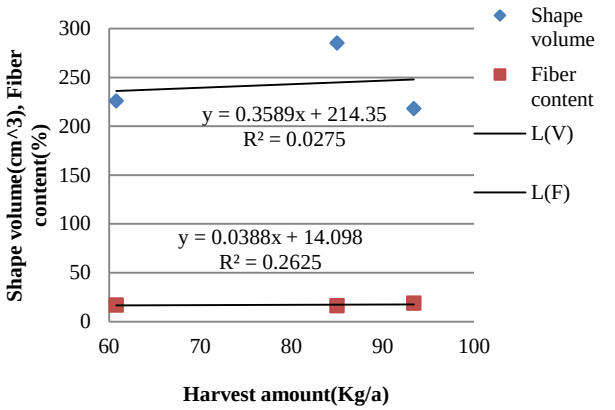

Fig. 12. Relations between harvest amount and shape volume as well as fiber content in tealeaves

It is found that the relation between harvest amount and fiber content is greater than that shape volume.

IV. CONCLUSION

Method for most appropriate tealeaves harvest timing with the reference to the fiber content in tealeaves which can be estimated with ground based Near Infrared (NIR) camera images is proposed. In the proposed method, NIR camera images of tealeaves are used for estimation of nitrogen content and fiber content in tealeaves. The nitrogen content is highly correlated to Theanine (amid acid) content in tealeaves. Theanine rich tealeaves taste good. Meanwhile, the age of tealeaves depend on fiber content. When tealeaves are getting old, then fiber content is increased. Tealeaf shape volume also is increased with increasing of fiber content. Fiber rich tealeaves taste not so good, in general. There is negative correlation between fiber content and NIR reflectance of tealeaves. Therefore, tealeaves quality of nitrogen and fiber contents can be estimated with NIR camera images. Also, the shape volume of tealeaves is highly correlated to NIR reflectance of tealeaf surface. Therefore, not only tealeaf quality but also harvest amount can be estimated with NIR camera images.

Experimental results show the proposed method works well for estimation of appropriate tealeaves harvest timing with fiber content in the tealeaves in concern estimated with NIR camera images. It is found that the appropriate tealeaf harvest day can be determined by using fiber content in tealeaves which is estimated with NIR camera data. Also, it is found that harvest amount can be estimated with fiber content in tealeaves which is derived from NIR camera data.

Further study is required for a relation between micro meteorological condition and the best harvest timing. Pilot tea farm area is the best solar illumination condition among three test sites followed by Front and Back. The other conditions, fertilizer amount, water supply, insect damage management, etc. are almost same for each test sites. Therefore, weather condition; in particular, solar illumination condition must be key issues for determination of the best harvest timing.

REFERENCES

[1] J.T.Compton, Red and photographic infrared linear combinations for monitoring vegetation, Journal of Remote Sensing of Environment, 8, 127-150, 1979.

[2] C.Wiegand, M.Shibayama, and Y.Yamagata, Spectral observation for estimating the growth and yield of rice, Journal of Crop Science, 58, 4, 673-683, 1989.

[3] S.Tsuchida, I.Sato, and S.Okada, BRDF measurement system for spatially unstable land surface-The measurement using spectro-radiometer and digital camera- Journal of Remote Sensing, 19, 4, 49-59, 1999.

[4] K.Arai, Lecture Note on Remote Sensing, Morikita-shuppan Co., Ltd., 2000.

[5] K.Arai and Y.Nishimura, Degree of polarization model for leaves and discrimination between pea and rice types of leaves for estimation of leaf area index, Abstract, COSPAR 2008, A3.10010-08#991, 2008.

[6] K.Arai and Long Lili, BRDF model for new tealeaves and new tealeaves monitoring through BRDF monitoring with web cameras, Abstract, COSPAR 2008, A3.10008-08#992, 2008.

[7] Greivenkamp, John E., *Field Guide to Geometrical Optics*. SPIE Field Guides vol. FG01. SPIE. ISBN 0-8194-5294-7, 2004.

[8] Seto R H. Nakamura, F. Nanjo, Y. Hara, *Bioscience, Biotechnology, and Biochemistry*, Vol.61 issue9 1434-1439 1997.

[9] Sano M, Suzuki M ,Miyase T, Yoshino K, Maeda-Yamamoto, M.,J.Agric.Food Chem., 47 (5), 1906-1910 1999.

[10] Kohei Arai, Method for estimation of grow index of tealeaves based on Bi-Directional reflectance function: BRDF measurements with ground based network cameras, International Journal of Applied Science, 2, 2, 52-62, 2011.

[11])Kohei Arai, Wireless sensor network for tea estate monitoring in complementally usage with Earth observation satellite imagery data based on Geographic Information System(GIS), International Journal of Ubiquitous Computing, 1, 2, 12-21, 2011.

[12] Kohei Arai, Method for estimation of total nitrogen and fiber contents in tealeaves with ground based network cameras, International Journal of Applied Science, 2, 2, 21-30, 2011.

[13] Kohei Arai, Monte Carlo ray tracing simulation for bi-directional reflectance distribution function and grow index of tealeaves estimation, International Journal of Research and Reviews on Computer Science, 2, 6, 1313-1318, 2011.

[14] K.Arai, Monte Carlo ray tracing simulation for bi-directional reflectance distribution function and grow index of tealeaves estimations, International Journal of Research and Review on Computer Science, 2, 6, 1313-1318, 2012.

[15] K.Arai, Fractal model based tea tree and tealeaves model for estimation of well opened tealeaf ratio which is useful to determine tealeaf harvesting timing, International Journal of Research and Review on Computer Science, 3, 3, 1628-1632, 2012.

[16] Kohei Arai, Method for tealeaves quality estimation through measurements of degree of polarization, leaf area index, photosynthesis available radiance and normalized difference vegetation index for characterization of tealeaves, International Journal of Advanced Research in Artificial Intelligence, 2, 11, 17-24, 2013.

[17] K.Arai, Optimum band and band combination for retrieving total nitrogen, water, and fiber in tealeaves through remote sensing based on regressive analysis, International Journal of Advanced Research in Artificial Intelligence, 3, 3, 20-24, 2014.

AUTHORS PROFILE

Kohei Aarai He received BS, MS and PhD degrees in 1972, 1974 and 1982, respectively. He was with The Institute for Industrial Science and Technology of the University of Tokyo from April 1974 to December 1978 and also was with National Space Development Agency of Japan from January, 1979 to March, 1990. During from 1985 to 1987, he was with Canada Centre for Remote Sensing as a Post Doctoral Fellow of National Science and Engineering Research Council of Canada. He moved to Saga University as a Professor in Department of Information Science on April 1990. He was a councilor for the Aeronautics and Space related to the Technology Committee of the Ministry of Science and Technology during from 1998 to

2000. He was a councilor of Saga University for 2002 and 2003. He also was an executive councilor for the Remote Sensing Society of Japan for 2003 to 2005. He is an Adjunct Professor of University of Arizona, USA since 1998. He also is Vice Chairman of the Commission-A of ICSU/COSPAR since 2008. He wrote 34 books and published more thyan 510 journal papers. He is Edito-inChief of IJACSA and International Journal of Intelligent Systems and Applications. http://teagis.ip.is.saga-u.ac.jp/bib.html

Driver's Awareness and Lane Changing Maneuver in Traffic Flow based on Cellular Automaton Model

Kohei Arai[1]
1 Graduate School of Science and Engineering
Saga University
Saga City, Japan

Steven Ray Sentinuwo[2]
2 Sam Ratulangi University,
Kampus Unsrat, Manado, Indonesia

***Abstract*—Effect of driver's awareness (e.g., to estimate the speed and arrival time of another vehicle) on the lane changing maneuver is discussed. "Scope awareness" is defined as the visibility which is required for the driver to make a visual perception about road condition and the speed of vehicle that appears in the target lane for lane changing in the road. Cellular automaton based simulation model is created and applied to simulation studies for driver awareness behavior. This study clarifies relations between the lane changing behavior and the scope awareness parameter that reflects driver behavior. Simulation results show that the proposed model is valid for investigation of the important features of lane changing maneuver.**

Keywords—traffic cellular automata; scope awareness; lane changing maneuver; driver perception; speed estimation

I. INTRODUCTION

Recent study on the traffic flow reports that the traffic congestion is influenced not only by the road capacity condition, but also by the driver behavior [1]. The other studies also found the strong relationship between the driver' speed behavior and accidents [2]-[6]. There are two separate components which affect human factors in driving, driving skills and driving style [7]. Driving style has a direct relation to the individual drivers' behavior. The U.S. Department of Transportation recently reported that driver behavior is leading to lane-change crashes and near-crashes [8]. In some countries, the reckless driving behaviors such as sudden-stop by public-buses, tailgating, or vehicles which changing lane too quickly also could give an impact to the traffic flow.

The lane changing maneuver is one of the actions in the highway. Lane changing is defined as a driving maneuver that moves a vehicle laterally from one lane to another lane where both lanes have the same direction of travel. Lane changing maneuvers are occasionally performed in order to avoid hazards, obstacles, vehicle collision, or pass through the slow vehicle ahead. Lane changing requires high attention and visual perceptions compared to normal highway of freeway driving due to the need to continually monitor areas around the subject vehicle [9]. However, in the real traffic situations, there are some reckless drivers that change the lanes at the moment when they signal or who make "last-minutes-decision" on the road. Frequent lane changing in roadway could affect traffic flow and even lead accidents. The lane changing behaviors can be very depended on the characteristic of the driver [10].

There are some crashes of accidents typically referred to as Look-But-Fail-To-See errors because drivers involved in these accidents frequently. These are reported that they failed notification of the conflicting vehicles in spite of looking in the appropriate directions; commonly occur when drivers change lanes [25]. This means that the drivers typically use their visual perception in order to estimate the speed and the arrival time of the other vehicles before making a maneuver, e.g., lane changing maneuver.

A psychology study is also reported that the accuracy level of this visual perception may lead to both failures, detect the collision and judge the crash risk (e.g., time-to-contact). From a certain distance, a short fixation may be enough to identify an approaching vehicle. If gaze duration for stimulus processing is long, then it is complicated processing while it is short for simple processing. Inaccuracy of the gazes' duration is likely to reflect a failure to process these stimuli [26].

The Cellular Automata model of Nagel and Schreckenberg (NaSch) [12] is improved for showing effects of scope awareness that reflect drivers' behavior when they are making a lane changing. This NaSch model has been modified to describe more realistic movement of individual vehicle when make a lane changing maneuver. Moreover, the recent study of spontaneous braking behavior [1] enhances the driver's scope awareness behavior. The proposed model is based on NaSch model which takes into account scope of awareness and spontaneous braking in order to clarify the effects of these drivers' behavior.

This paper is organized as follows. Section 2 presents a theoretical aspect of traffic CA model. Section 3 explains the proposed model. Section 4 describes simulation process and the results in the form of fundamental diagrams and space-time diagrams. Finally, in section 5, a summary and conclusion is described with some discussions.

II. TRAFFIC CELLULAR AUTOMATA MODEL

One of the famous microscopic models for road traffic flow simulation is Cellular Automata (CA) model. CA model is a discrete computability mathematical model. In comparison with another microscopic model, CA model based approach is efficient [11] and is used for dynamic system simulations. CA model consists of two components, a cellular space and a set of state. The state of a cell is completely determined by its nearest neighboring cells.

All neighborhood cells have the same size in the lattice. Each cell can either be empty, or is occupied by exactly one node (car in this simulation model). There is a set of local transition rule that is applied to each cell from one discrete

time step to another (i.e., iteration of the system). This parallel updating from local simple interaction leads to the emergence of global complex behavior. Furthermore, the utilization of CA model successfully explains the phenomenon of transportation. These traffic cellular automata (TCA) are dynamical systems that are discrete in nature and powerful to capture all previously mentioned basic phenomena that occur in traffic flows [11].

The one dimensional cellular automata model for single lane freeway traffic is introduced by Nagel and Schreckenberg (NaSch) [12]. This model shows how traffic congestion can be thought of as an emergent or collective phenomenon due to interactions between cars on the road, when the car density is high (cars are close to each on average). According to NaSch model, the randomization rule captures natural speed fluctuations due to human behavior or varying external conditions [14].

In a real traffic situation, most highways have two or more lanes. Regarding this road condition, there are a few analytical models for multi-lane traffic. Nagatani is one of the first researchers who introduced a CA model for two lane traffic [24]. Then, in addition to the Nagatani's model, Rickert et al. [15] considers a model with $v_{\max} \geq 1$. Their model introduces the lane changing behavior for two lanes traffic. They proposed a symmetric rule set where the vehicle changes lanes if the following criteria are fulfilled:

$$\text{gap}(i) < l \quad (1)$$

$$\text{gap}_0(i) > l_0 \quad (2)$$

$$\text{gap}_{0,\text{back}}(i) > l_{0,\text{back}} \quad (3)$$

The variable gap(i), $\text{gap}_0(i)$, and $\text{gap}_{0,\text{back}}(i)$ denote the number of empty cells between the vehicle and its predecessor on its current lane, and forward gap on the desired lane, and backward gap on the desired lane, respectively. Rickert also uses the parameters which allow decide how far the vehicle look ahead in the current lane for l, ahead on the desired lane for l_0, and how far the vehicle look back on the desired lane for $l_{0,back}$.

The advanced analysis about lane-changing behavior is reported which includes symmetric and asymmetric rules of lane-changing [16]-[19], [20]-[23].

III. Proposed Model Definition and Simulation

The proposed model uses two-lane highway with unidirectional traffic character in periodic boundaries condition. Two-lane model is necessary in order to accommodate the lane changing behavior in the real traffic condition. A one-dimensional chain of L cells of length 7.5 m represents each lane. This value is considered as the length of vehicle plus the distance between vehicles in a stopped position. A one-lane consists of 10^3 cells. There are just two possible states of each cell. Each cell can only be empty or containing by just one vehicle. The speed of each vehicle is integer value between v = 0, 1, . . ., v_{max}. In this model, all vehicles are considered as homogeneous and have the same maximum speed v_{max} = 5. The speed value number corresponds to the number of cell that the vehicle proceeds at one time step. The state of a road cell at the next time step, form t to t + 1 is dependent on the states of the direct frontal neighborhood cell of the vehicle and the core cell itself of the vehicle.

Rickert et al. [15] discusses criteria of safety by introducing the parameters which decide how far the vehicle looks ahead on current lane, looks ahead on desired lane, and looks back on desired lane. Those criteria have to be fulfilled before a vehicle makes a lane changing. However, in real traffic condition, these criteria of safety rules by Rickert are not sufficient to describe driver's behaviors in highway traffic. This paper introduces a new additional parameter to accommodate the driver behavior when making a lane changing. In addition to considering the gap of cell that consists of vehicle, the speed parameter of the other vehicle that situated in the desired lane is taken into account. The parameter of scope awareness S_a that reflects the various characters of driver is introduced. The scope awareness parameter represents drivers' behavior when lane changing. S_a value reflects the degree of driver aggressiveness and awareness. Fig.1 shows schematic definition diagram of scope awareness S_a from the perspective of the vehicle (the third cell on lane 2) in its current speed and position $v_{(1);}\ x_{(1)}$

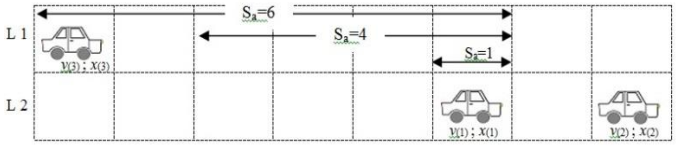

Fig. 1. Schematic definition diagram of scope awareness S_a from the perspective of the vehicle (the third cell on lane 2) in its current speed and position $v_{(1);}\ x_{(1)}$

S_a=1 implies very dangerous because the driver of vehicle 1intend to make a lane changing even the gap between the car and the car ahead of the car on the next lane is only one cell. On the other hand, the lane changing can be done safely when S_a=6 because the gap between both is six cells.

In contrast to the gap-length model's parameter [15], the scope awareness parameter S_a accommodates the sight distance taken by the driver to make a perception about road-lane condition and the speed of other vehicles that exist in target lane. Therefore, the subject vehicle would consider changing its lane not only due to the comparison value between the number of gap and condition which decide how far the vehicle look ahead in the current lane, but also depending on the current speed of the subject vehicle and the speed of other vehicles that situated along the scope awareness area.

The updating rule for lane changing maneuver is done in accordance with a set of rules. In comparison to the lane changing model of Rickert et al. [15], there are two basic differences rules from the proposed model. The first one, as the result of traffic conditions ahead of subject driver, the subject vehicle would consider changing its lane not only due to the comparison value between the number of gap and condition which decide how far the vehicle look ahead in the current lane, but also depending on the current speed of the subject vehicle that can be varied based on traffic situation. Another difference is the scope awareness value (S_a). The subject vehicle would consider the speed of vehicles that situated along with its scope

awareness area then decide whether possible or not to change the lane.

At the beginning of iterations, the subject driver checks desirability of a lane changing. The subject driver looks ahead to check if the existing gap in the current lane can accommodate the current speed. If not, then due to the randomness number of percentage ratio, the subject driver decides whether the driver maintains or decelerates the vehicle speed due to the existing gap number or change the lane. When the subject driver chooses to "lane changing", then driver looks sideways at the other lane to check whether the cell next to the subject vehicle is empty and the forward gap on the other lane is equal or longer than the current lane. If one cell is unoccupied or free-cell then its state is 0. Moreover, the subject driver also looks back at the other lane to check road condition. In real traffic situations, a subject driver also has to look back on the other lane in order to estimate the velocity of the following vehicle to avoid a collision. Equation (8) accommodates the driver behavior that estimate the velocity of vehicle at the moment before making a lane changing.

If there is another vehicle within the area of scope awareness, then the subject driver estimates the speed of the vehicle in order to avoid collision during the lane changing maneuver. The subject driver makes a lane changing maneuver if the speed of the vehicle that is located within the area of scope awareness is less than the existing gap. The lane changing rules can be summarized as follows:

$$gap_{same} < v_{current} \quad (4)$$

$$cell_{next} = 0 \quad (5)$$

$$rand() < p_{change} \quad (6)$$

$$gap_{target} > gap_{same} \quad (7)$$

$$v_{Vehicle,back} \leq gap_{back} ; X(vehicle_{back}) \epsilon S_a \quad (8)$$

The lane changing rules are applied to the vehicle that changes from right lane to left lane and conversely. The vehicle only moves sideways and it does not advance. Once all the lane changing maneuvers are made, then the updating rules from a single lane model are applied independently to each lane. Fig.2 shows the schematic diagram of lane changing operation.

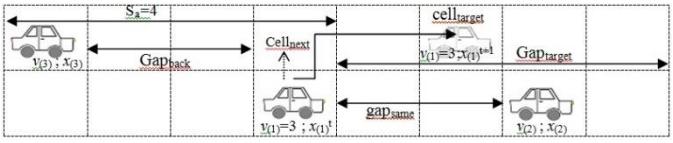

Fig. 2. Schematic diagram of a lane changing operation

In Fig.2, the subject vehicle $v_{(1)}$; $x_{(1)}$ is assumed that have the current speed $v_{(1)}^{t}$ = 3 cell per time step and the parameter of scope awareness S_a = 4 cells. In order to avoid the introduction of any unrealistic artifacts in the simulation then the proposed model uses eq. (7) to express the more realistic lane changing decision. According to eq. (7), the driver must consider that the forward gap in the desired lane is more than the gap in the current lane. This consideration is important because the proposed model uses the different desired velocities for the vehicles.

Once the lane changing maneuvers are made to all possible vehicles, then the updating rules from a single lane model are applied independently to each lane. Together with a set of lane changing rules, the road state is obtained by applying the following rules to all by parallel updated:

$$\text{Acceleration: } v(i) \rightarrow \min(v(i)+1, v_{max}) \quad (9)$$

$$\text{Deceleration: } v(i) \rightarrow \min(v(i), gap_{same}(i)) \quad (10)$$

$$\text{Driving: } x(i) \rightarrow x(i)+v(i) \quad (11)$$

IV. Simulation Results

The simulation starts with an initial configuration of *N* vehicles, with fixed distributions of positions on both lanes. The simulation uses the same initial velocity for all vehicle v_{min} = 0 and the maximum vehicle speed has been set to v_{max} = 5 cell/time-step. The velocity corresponds to the number of cells that a vehicle advances in iteration. Many simulations are done with the different density ρ. The density ρ is defined as the number of vehicles *N* along with the highway over the number of cells on the highway *L*.

The traffic model uses close (periodic) boundary conditions. This means that during one simulation, the total number of vehicles on the highway cannot be changed. Vehicles move from left to right. If a vehicle arrives on the right boundary then it moves to the left boundary. Since the proposed model assumes symmetry character of the both lanes, the traffic flow characteristics on both lanes are identical.

A. Traffic Flow

In order to examine the effect of scope awareness on the traffic flow, then the proposed model is simulated over 1000 iterations on 10^3 cells for all possible density level. The flow indicates the number of moving vehicles per unit of time. Along with the study of the proposed model, a comparative study between with and without using scope awareness parameter.

Fig.3 shows the average flow-density diagram of the proposed model is compared to a two-lane traffic system without using scope awareness parameter.

The following results are made:

1) The proposed model reproduces a recognizable diagram of flow towards density relationship. Flow is linearly increasing together with the increases in density level. A maximum flow level is achieved at density level ρ=0.5 for each value of S_a. After reaches the critical point of flow at ρ=0.5, the flow at each level of S_a becomes linearly decreasing in density. In other words, the laminar flow turn into back travelling start-stop waves after density level ρ=0.5.

2) Compared to the model without scope awareness consideration (Fig.3-bottom diagram), the usage of S_a parameter produced a better flow of vehicles, especially above density ρ=0.4. The Sa parameter maintained the traffic to keep flowing by carefully calculate the appropriate time to make a lane changing decision, thus the lane changing maneuver does not disturb the traffic in the target lane.

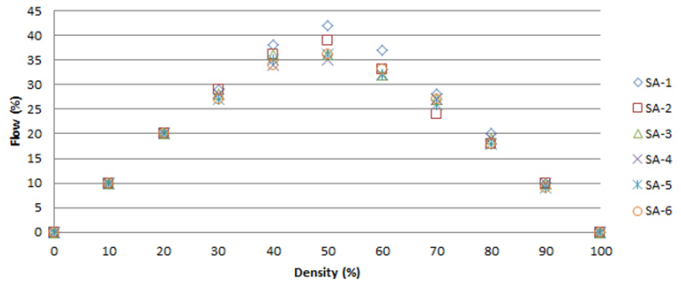

(a) Average flow-density diagram of the proposed model

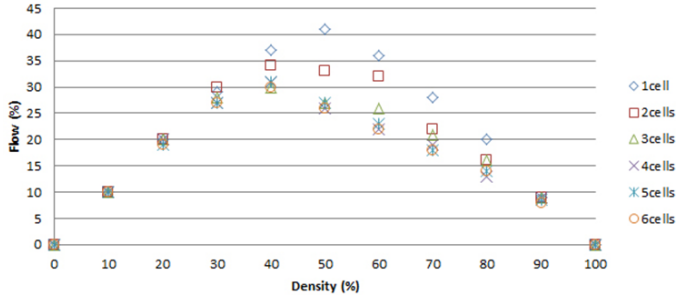

(b) Two-lane traffic system without using scope awareness parameter

Fig. 3. The average flow-density diagram of the proposed model is compared to a two-lane traffic system without using scope awareness parameter

B. Space-Time Diagram

The space-time diagram represents the location of the vehicles at the certain time. The space-time diagram for density ρ=0.25, ρ=0.5, and ρ=0.75 is shown. These three values of density assumed as the light traffic, moderate traffic, and heavy traffic in the real traffic condition, respectively. Fig.4 shows the result for density ρ=0.25 at all the values of scope awareness while the lane changing probability is 100%. Fig.4 (a) for Scope awareness Sa=1 ; (b) for Scope awareness Sa=2 ; (c) for Scope awareness Sa=3 ; (d) for Scope awareness Sa=4 ; (e) for Scope awareness Sa=5 ; (f) for Scope awareness Sa=6, respectively. The horizontal axis represents space while the vertical axis represents the time. Vehicles move from left to right in space axis while from top to bottom in time axis.

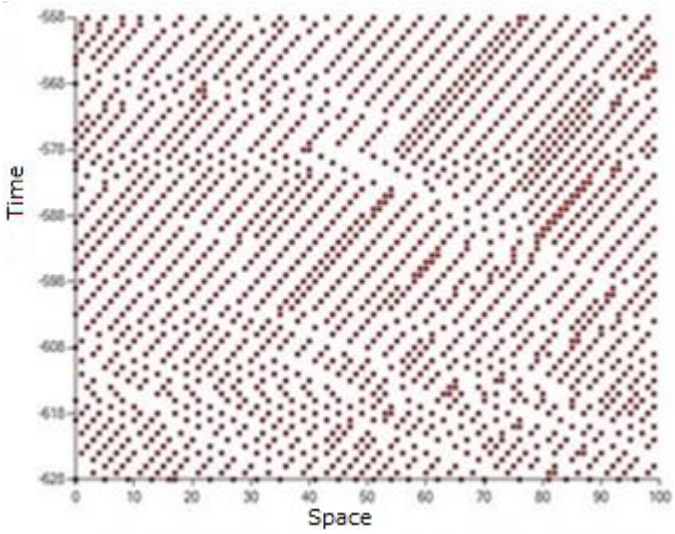

(a)Sa=1

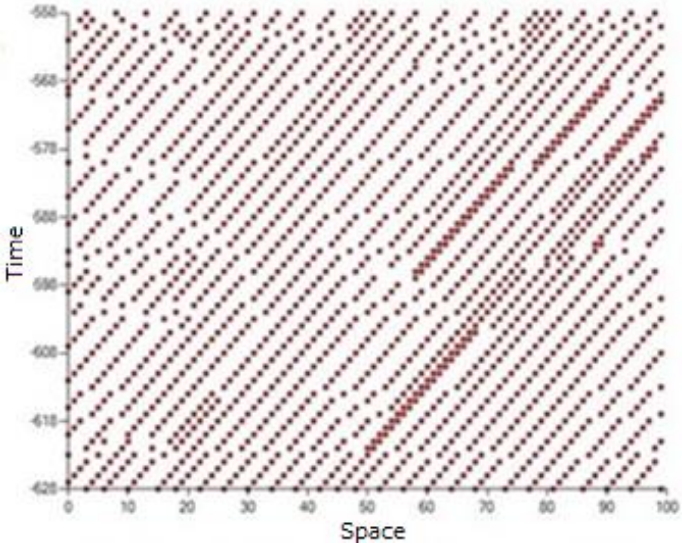

(b)Sa=2

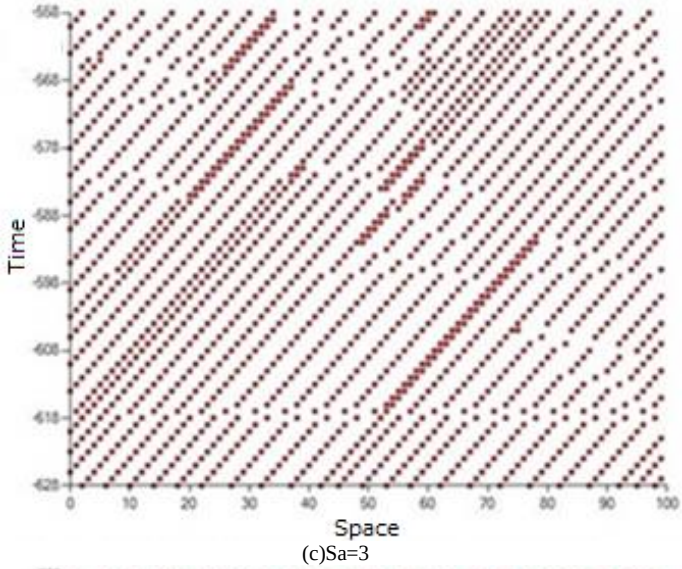

(c)Sa=3

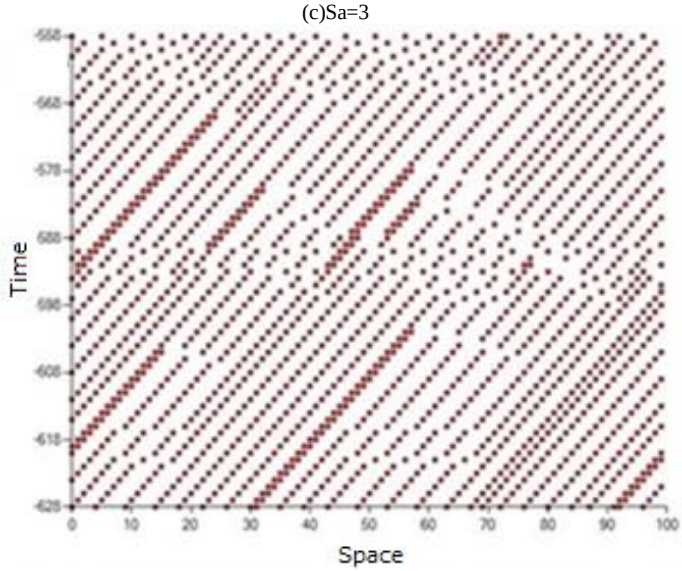

(d)Sa=4

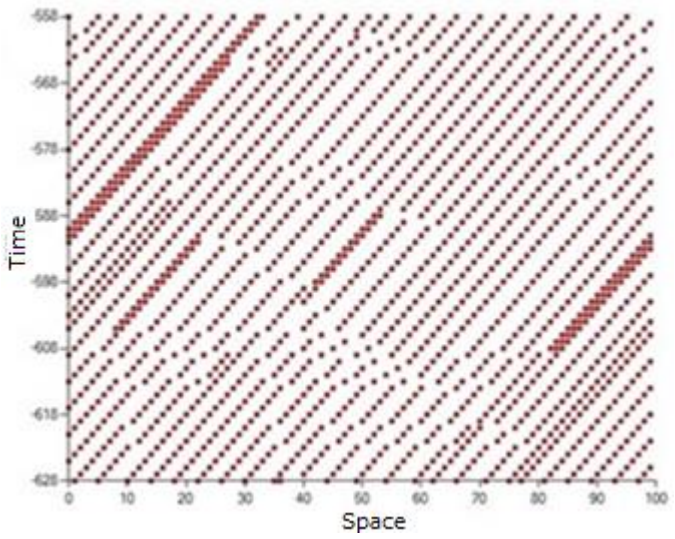

(e)Sa=5

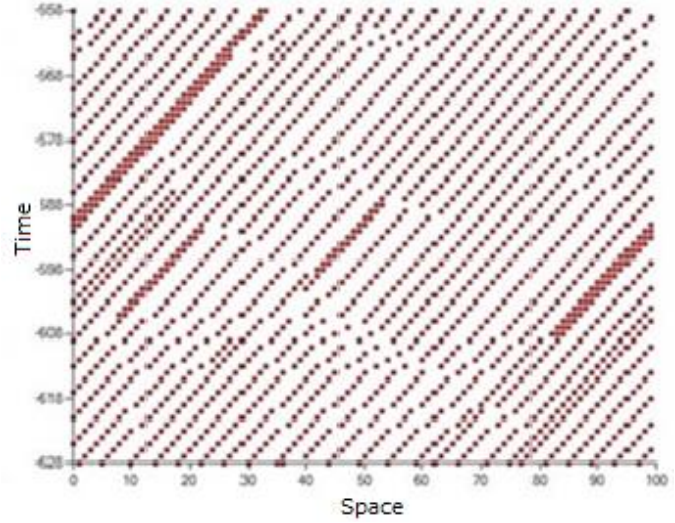

(f)Sa=6

Fig. 4. Space-time diagram for light traffic condition (density ρ = 25%). Lane changing probability 100%. (a) for Scope awareness Sa=1 ; (b) for Scope awareness Sa=2 ; (c) for Scope awareness Sa=3 ; (d) for Scope awareness Sa=4 ; (e) for Scope awareness Sa=5 ; (f) for Scope awareness Sa=6

In the light traffic condition ρ=0.25, the increases of scope awareness distance affect the vehicles flow. Free flow phase showed in Sa=1 diagram (Fig.4 (a)), which are drawn as light area and have shallow negative inclinations. However, when the Sa value is increased then some solid area appears. The solid area with steep positive inclination reflects the traffic jam. Short-vehicle-life-lines frequently appear and disappear in this case. This implies that there are a great number of lane changing at this traffic density ρ=0.25. In accordance with increasing of the scope awareness, occurrence of the short-vehicle-life-lines becomes smaller than before (Fig.4 (f)). Meanwhile, in the heavy traffic condition, traffic situation is independent on scope awareness. In this traffic condition, lane changing is very rare. The result implies that in the heavy traffic condition, drivers' lane changing style have no influence to the traffic situation.

Table 1 (a) and (b) present the ratio of the spontaneous braking number over lane changing by using the scope awareness parameter (SA) and without using the scope awareness parameter, respectively. "0" means that the spontaneous braking did not happen, although the lane changing maneuver is still occurring in this certain traffic condition. Meanwhile, "N/A" means that the lane changing maneuver did not occur at all in this traffic condition.

TABLE I. RATIO OF THE SPONTANEOUS BRAKING NUMBER OVER LANE CHANGING WITH THE SCOPE AWARENESS PARAMETER (SA) AND WITHOUT THE SCOPE AWARENESS PARAMETER

(A)WITH SA

DENSITY(%)	SA-1(%)	SA-2(%)	SA-3(%)	SA-4(%)	SA-5(%)	SA-6(%)
10	56	40	23	24	20	0
20	82	74	63	38	18	3
30	81	60	12	0	0	0
40	82	35	3	0	0	0
50	92	11	0	0	0	0
60	83	8	0	0	0	0
70	85	9	0	0	0	0
80	80	0	0	0	0	0
90	88	0	0	0	0	0

(B)WITHOUT SA

DENSITY(%)	SA-1(%)	SA-2(%)	SA-3(%)	SA-4(%)	SA-5(%)	SA-6(%)
10	53	45	36	48	13	0
20	82	83	80	63	17	6
30	71	64	55	9	0	0
40	74	63	6	0	0	N/A
50	85	33	0	0	N/A	N/A
60	89	14	0	N/A	N/A	N/A
70	91	20	0	N/A	N/A	N/A
80	100	0	0	N/A	N/A	N/A
90	100	N/A	N/A	N/A	N/A	N/A

It is found that the ratio is getting large in accordance with density while the ratio is getting small according to SA parameters. Also, the ratio of the case with SA is smaller than that without SA. These implies that the number of spontaneous braking can be suppressed by considering scope of awareness.

C. Vehicle Speed EstimationEerror

When the drivers make mistakes in speed estimation by visual perception, then the drivers fails their lane changing. Therefore speed estimation error is a key factor of lane changing. Fig.5 shows the effect of speed estimation error to the lane changing (a) and to the spontaneous braking action (b) in the light traffic ρ=0.25, moderate traffic ρ=0.5, and heavy traffic ρ=0.75, respectively. Fig.5 (c) shows the ratio between both of lane changing and spontaneous braking.

It is obvious that the number of lane changing and spontaneous braking are increased with increasing of the speed estimation error. Also, the number of lane changing and spontaneous braking in light traffic condition is larger than that in moderate and heavy traffic conditions. The reason for this is that it is getting hard for lane changing and spontaneous braking when the traffic condition is getting heavy. Also, it may say that it is getting hard for lane changing and spontaneous braking when the speed estimation error is increased.

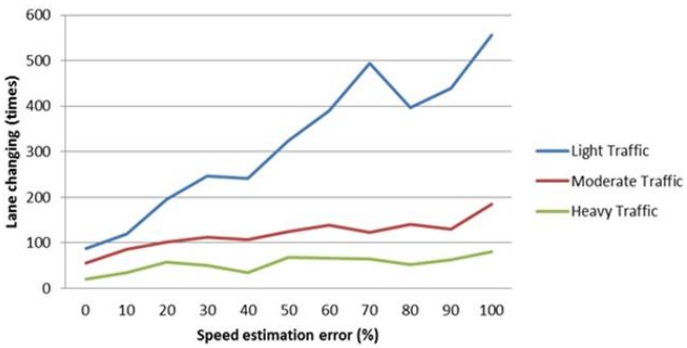

(a)Lane changing manoeuvre

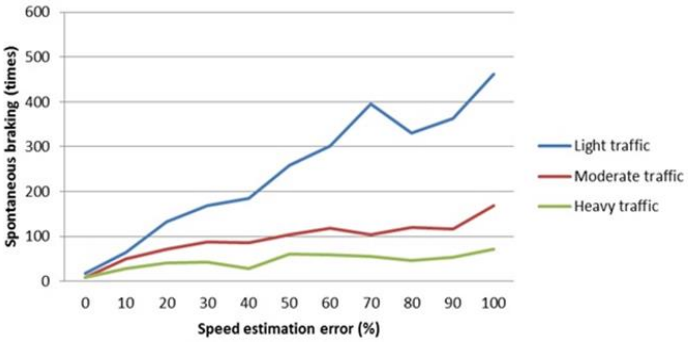

(b) Spontaneous braking number

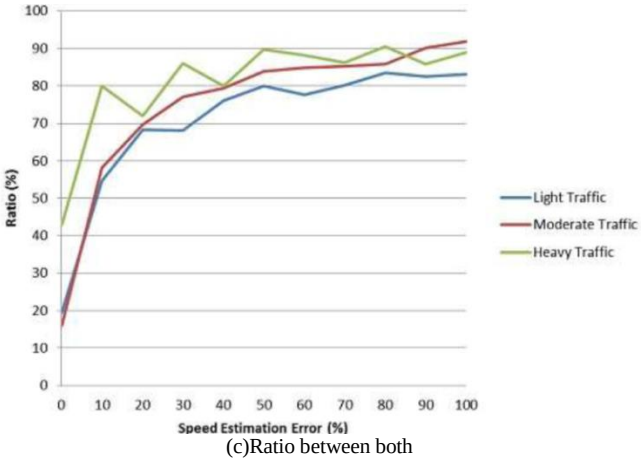

(c)Ratio between both

Fig. 5. Effect of speed estimation error to the lane changing manoeuvre (a) and to the spontaneous braking number (b) together with the ratio between both (c). These diagrams are simulated for the case S_a=**6**

Lane changing is much influencing to traffic situation than spontaneous braking, in general. Speed estimation error in lane changing is much influencing than that in spontaneous braking. Fig.6 shows Space-Time diagrams with consideration of speed estimation errors in the visual perception based driver's vehicle speed estimation raged from 0 to 1 for the light traffic condition (SA=6).

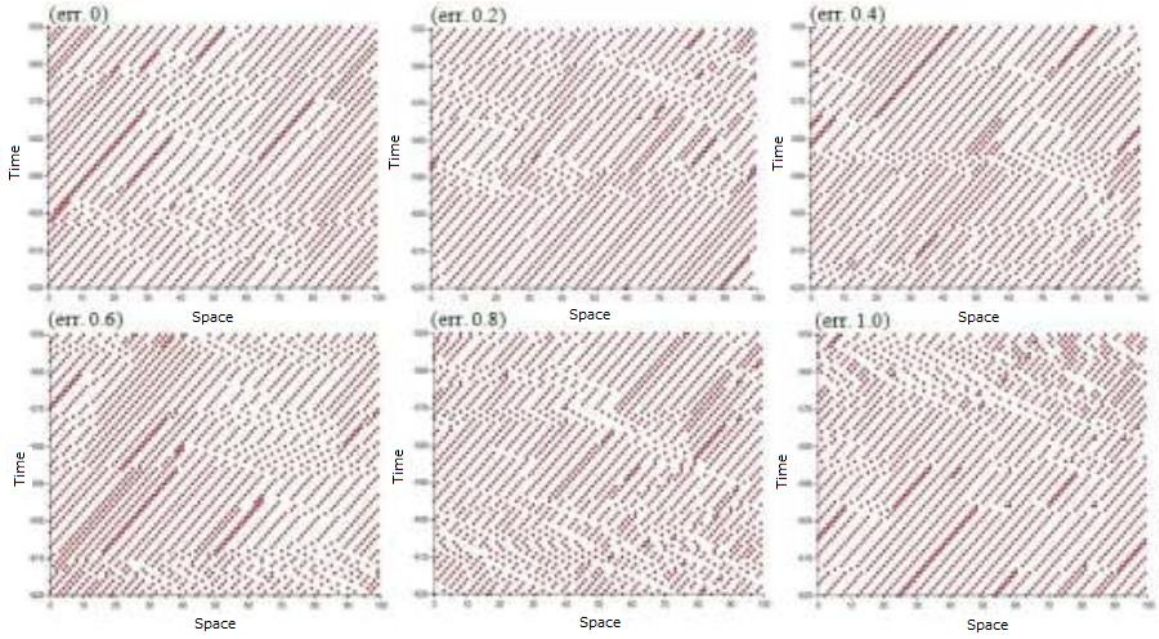

Fig. 6. Space-Time diagrams with consideration of speed estimation errors in the visual perception based driver's vehicle speed estimation raged from 0 to 1 for the light traffic condition (SA=6)

Through a comparison between Fig.4 and 6, it is found that traffic congestions seem to be independent to the speed estimation error and are happened occasionally. The phenomena of short-thin solid lines and wide solid lines also appear in these values of traffic density. The appearance of short-thin solid lines and the disappearance of wide solid line confirmed the conclusion that the short-thin solid line caused by the lane changing maneuver of another vehicle from adjacent lane so the subject vehicle has to make a spontaneous braking in order to avoid collision, and the wide solid line appeared as a result of deceleration into the minimum speed of the vehicle as the consequence of the reduced opportunities for lane changing maneuver.

V. SUMMARY AND CONCLUSION

The simulation model of the traffic cellular automata for representation of a driver behavior in a two lane highway is proposed. The term of scope awareness introduced to reflect

the certain area of roadway that is considered by the driver to make a perception of road condition. This perception includes the estimation speed of vehicles that are located within the scope-awareness distance prior to make a lane changing maneuver. The relation between flow-density and space-time are investigated in order to examine the effect of scope awareness parameter in the traffic flow. The followings are concluded through this study,

1) This model describes the realistic traffic situation, in particular for capturing the situation when driver make a lane changing maneuver. Compared to the conventional approach, the usage of scope awareness model approach produces a better flow of vehicles.

2) The various parameters of the scope awareness may represent the characteristic and the experience level of the drivers. The increases of the scope awareness value means the driver become much aware to estimate the road condition in a lane changing maneuver.

3) The proposed model reveals the phenomena of the short-thin solid line jam and the wide solid line jam in the traffic flow. It is found that the short-thin solid lines are the result of the lane changing maneuver of another vehicle from adjacent lane which makes the subject vehicle which has to make a spontaneous braking in order to avoid collision. As the result of this spontaneous braking, it is causing the other following vehicles which have to adjust or decrease their speed with the vehicle ahead. This action introduces a short queue of vehicles. On the other hand, a wide solid line appears as a result of the deceleration vehicle speed to the minimum speed of the vehicles as the consequence of the reduced lane changing chances. The chance reduction introduces a transient bottleneck effect.

4) The simulation results show that lane changing maneuvers with taking into account another vehicle speed could reduce the level of traffic congestion. However, in the heavy traffic (high dense) situation, the chance of a lane changing is small which results in traffic congestions.

The simulation results show that when the driver become more aware during lane changing decision, then the traffic flow seems to behave a single lane traffic character. In the situation, the vehicles tend to decrease its speed rather than making a lane changing. Moreover, the results indicate that in the density level less than 75%, traffic congestion is reduced by managing of the driver behavior. Other than that, the management of driver behavior makes a significant impact. The simulation result can serve as a reference for transportation planning, evaluation, and control. Moreover, the result paves the way for accurate simulation of a more complex traffic system. Based on the result, the effect of road shape towards the vehicle deceleration is to be studied hereafter.

REFERENCES

[1] K. Arai and S. Sentinuwo, "Spontaneous-braking and lane-changing effect on traffic congestion using cellular automata model applied to the two lane traffic", (IJACSA) International Journal of Advanced Computer Science and Applications, Vol. 3 (8), 2012.

[2] Elvik, R., Vaa, T. (2004) The Handbook of Road Safety Measures. Elsevier Science, Oxford.

[3] Finch, D. J., Kompfner, P., Lockwood, C. R. & Maycock, G. (1994) Speed, speed limits and crashes. Project Record S211G/RB/Project Report PR 58. Transport Research Laboratory TRL, Crowthorne, Berkshire.

[4] Nilsson, G. (2004). Traffic safety dimensions and the power model to describe the effect of speed on safety. Lund Bulletin 221. Lund Institute of Technology, Lund.

[5] Salusjärvi, M., 1981. The speed limit experiments on public roads in Finland. Technical Research Centre of Finland. Publication 7/1981. Espoo, Finland.

[6] Lewin, I. (1982). Driver training a perceptual-motor skill approach. Ergonomics,25, 917–924.

[7] Elander, J., West, R., & French, D. (1993). Behavioral correlates of individual differences in road traffic crash risk: An examination of methods and findings. Psychological Bulletin, 113, 279–294.

[8] G. M. Fitch, S. E. Lee, S. Klauer, J. Hankey, J. Sudweeks, and T. Dingus. Analysis of Lane-Change Crashes and Near-Crashes. National Technical Information Service, Springfield, VA 22161, 2009

[9] Shinar, D., Psychology on the road: The human factor in traffic safety. Wiley New York, (1978)

[10] Sun, D. J., & Elefteriadou, L. (2011). Lane-changing behavior on urban streets: a focus group-based study. Applied ergonomics, 42(5), 682–91. doi:10.1016/j.apergo.2010.11.001.

[11] X. G. Li, B. Jia, Z. Y. Gao, and R. Jiang, "A realistic two-lane cellular automata traffic model considering aggressive lane- changing behavior of fast vehicle," PhysicaA, vol. 367, pp. 479– 486, 2006.

[12] K. Nagel and M. Schreckenberg, "A cellular automaton model for freeway traffic," Journal of Physics I France, vol. 2, no. 12, pp.2221-2229, 1992.

[13] K. Nagel, Wolf, Wagner, and Simon, "Two-lane traffic rules for cellular automata: A systematic approach," Physical Review E, vol.58, no.2, 1998.

[14] S. Maerivoet and B. D. Moor, "Transportation Planning and Traffic Flow Models," 05-155, Katholieke Universiteit Leuven, Department of Electrical Engineering ESAT-SCD (SISTA), July 2005.

[15] M. Rickert, K. Nagel, M. Schreckenberg, and A. Latour, "Two Lane Traffic Simulations using Cellular Automata," vol. 4367, no. 95, 1995.

[16] W. Knospe, L. Santen, A. Schadschneider, and M. Schrekenberg, "Disorder effects in cellular automata for two lane traffic," Physica A, vol. 265, no. 3-4, pp. 614–633, 1998.

[17] A. Awazu, "Dynamics of two equivalent lanes traffic flow model: selforganization of the slow lane and fast lane," Journal of Physical Society of Japan, vol. 64, no. 4, pp. 1071– 1074, 1998.

[18] E. G. Campri and G. Levi, "A cellular automata model for highway traffic," The European Physica Journal B, vol. 17, no. 1, pp. 159–166, 2000.

[19] L. Wang, B. H. Wang, and B. Hu, "Cellular automaton traffic flow model between the Fukui-Ishibashi and Nagel- Schreckenberg models," Physical Review E, vol. 63, no. 5, Article ID 056117, 5 pages, 2001.

[20] B. Jia, R. Jiang, Q. S. Wu, and M. B. Hu, "Honk effect in the two-lane cellular automaton model for traffic flow," Physica A, vol. 348, pp. 544–552, 2005.

[21] D. Chowdhury, L. Santen, and A. Schadschneider, "Statistical physics of vehicular traffic and some related systems," Physics Report, vol. 329, no. 4-6, pp. 199–329, 2000.

[22] W. Knospe, L. Santen, A. Schadschneider, and M. Schreckenberg, "A realistic two-lane traffic model for highway traffic," Journal of Physics A, vol. 35, no. 15, pp. 3369–3388, 2002.

[23] W. Knospe, L. Santen, A. Schadschneider, and M. Schreckenberg, "Empirical test for cellular automaton models of traffic flow," Phys. Rev. E, vol. 70, 2004.

[24] Nagatani, T., "Self Organization and Phase Transition in the Traffic Flow Model of a Two-Lane Roadway," Journal of Physics A, Vol. 26, pp. 781-787, 1993.

[25] Shahar, A., Van Loon, E., Clarke, D., & Crundall, D. Attending overtaking cars and motorcycles through the mirrors before changing lanes. Accident; analysis and prevention, 44(1), 104–10, 2012.

[26] Rayner, K., Warren, T., Juhasz, B.J., Liversedge, S.P. The effect of plausibility on eye movements in reading. Journal of Experimental Psychology: Learning, Memory and Cognition 30, 1290–1301, 2004.

[27] Benjaafar, S., & Dooley, K. (1997). Cellular automata for traffic flow modeling. Minneapolis, MN, University of. Retrieved from http://ntl.bts.gov/lib/21000/21100/21189/PB99103996.pdf.

[28] Paz, A., & Peeta, S. (2009). Information-based network control strategies consistent with estimated driver behavior. Transportation Research Part B: Methodological, 43(1), 73–96. doi:10.1016/j.trb.2008.06.007.

AUTHORS PROFILE

Kohei Arai He received BS, MS and PhD degrees in 1972, 1974 and 1982, respectively. He was with The Institute for Industrial Science and Technology of the University of Tokyo from April 1974 to December 1978 and also was with National Space Development Agency of Japan from January, 1979 to March, 1990. During from 1985 to 1987, he was with Canada Centre for Remote Sensing as a Post-Doctoral Fellow of National Science and Engineering Research Council of Canada. He moved to Saga University as a Professor in Department of Information Science on April 1990. He was a councilor for the Aeronautics and Space related to the Technology Committee of the Ministry of Science and Technology during from 1998 to 2000. He was a councilor of Saga University for 2002 and 2003. He also was an executive councilor for the Remote Sensing Society of Japan for 2003 to 2005. He is an Adjunct Professor of University of Arizona, USA since 1998. He also is Vice Chairman of the Commission-A of ICSU/COSPAR since 2008. He wrote 34 books and published more than 510 journal papers. He is Editor-in-Chief of IJACSA and International Journal of Intelligent Systems and Applications. http://teagis.ip.is.saga-u.ac.jp/bib.html.

Application of distributed lighting control architecture in dementia-friendly smart homes

Atousa Zaeim
School of CSE
University of Salford Manchester
United Kingdom

Samia Nefti-Meziani
School of CSE
University of Salford Manchester
United Kingdom

Adham Atyabi
School of CSE
University of Salford Manchester
United Kingdom
School of CSEM
Flinders University of South Australia

***Abstract*—Dementia is a growing problem in societies with aging populations, not only for patients, but also for family members and for the society in terms of the associated costs of providing health care. Helping patients to maintain a degree of independence in their home environment while ensuring their safeties is considered as a positive step forward for addressing individual needs of dementia patients. A common symptom for dementia patients including those with Alzheimer's Disease and Related Dementia (ADRD) is sleep disturbance, patients being awake at night and asleep during the day. One of the problems with night time sleep disturbance in dementia patients is the possible accidental falls of patients in the dark environment. An issue associated with un-hourly sleeping behavior in these patients is the lighting condition of their surroundings. Clinical studies indicate that appropriate level of lighting can help to restore the rest-activity cycles of ADRD patients. This study tackles this problem by generating machine learning solutions for controlling the lighting conditions of multiple rooms in the house in different hours based on patterns of behaviors generated for the patient. Several neural network oriented classification methods are investigated and their feasibilities are assessed with a collection of synthetic data capturing two conditions of balanced and unbalanced inter-class samples. The classifiers are utilized within two centric and distributed lighting control architectures. The results indicate the feasibility of the distributed architecture in achieving a high level of classification performance resulting in adequate control over lighting conditions of the house in various time periods.**

***Keywords*—Smart Home; Ambient intelligence; Machine Learning; Distributed Learning**

I. Introduction

Intelligent health-care technologies often include utilizing smart devices or systems tuned to operate optimally under some specific conditions, fuse and interpret information, and make decisions that benefit the patients' care. In the context of smart home, such smart devices interact with each other through "plug and play" mechanisms, intelligent software agents and inter-connection messaging protocols. Smart home is an attractive concept with many potentials and applications in intelligent health-care due to its ability to provide cognitive assistance whenever required[1],[2]. In this study, we investigate feasibility of smart lighting control for improving living conditions of dementia patients in the context of smart home.

The effectiveness of traditional verbal commands/prompts may be questioned especially for individuals with advanced Alzheimer's disease and Related Dementia (ADRD). Sleep disturbance is a common problem in ADRD patients that can cause possible accidental falls of patients in the dark environment [7]. It is reported that 40% of patients suffering from dementia also suffer from sleep disorder and being frightened from room darkness while being incapable of turning on the lights[3]. Smart control over lighting conditions of patients' surroundings can effectively improve their quality of life due to minimizing chances of such accidents while allowing the patients to be less dependent to constant presence of caregivers.

This study focuses on investigating the feasibility of machine learning solutions for controlling the lighting conditions of multiple rooms in the house in different hours. This is to be facilitated by creating patterns of behaviors for the patients and carers and tuning the lighting conditions to the patients needs. In a small scale (single room or a small house), fuzzy logic systems are ideal candidates for developing a smart lighting condition monitoring and controlling system due to their design simplicity and their performance accuracy. However, extending such designs to larger scales such as special hospitals with multiple patients and multiple rooms might be problematic due to the required tedious design adaptation stage.

In this study a distributed lighting control architecture is proposed and its feasibility is assessed against a commonly used centric architecture. The study considers a set of synthetic data and investigates the potential of several classification methods. In order to provide clear indication on overall performance of the system both balanced and unbalanced data sample conditions are considered.

The structure of this paper is as follows: related works are presented in Section II. The architectural design is reported in Section III. The procedures considered for generating the synthetic data that is utilized in this study are discussed in Section IV. The results are reported in Section V and the final conclusions and the future works are discussed in Sections VI and VII.

[1]National Sleep Foundation, http://sleepfoundation.org/ask-the-expert/sleep-and-alzheimers-disease/page/0/2

[2]Alzheimer's Society, http://www.alzheimers.org.uk/site/scripts/documents_info.php?documentID=145

[3]Alzheimer's Association, http://www.alz.org/alzheimers_disease_10429.asp

II. Related work

In the context of smart lighting control, Nagy et al [6] proposed an occupant centric lighting control strategy that utilizes occupant specific set-points with fixed minimum and maximum illuminance threshold set to the satisfaction of each occupant. The results indicated that within a six weeks duration in an environment with 10 offices total of 37% energy savings is achieved using the proposed strategy.

Gopalakrishna et al [8] investigated the use of prediction methods (decision trees) for intelligent lighting control in an office environment. The study is conducted on the basis of synthetic data within a large environment with 2 different areas for resting and having informal meetings. Various sample sizes in the range of 100 to 50k are considered with each sample reflecting mixtures of six sensory inputs. Although systematic experimentation is carried out to identify the maximum number of samples required to make an informed decision, the results are questionable due to possible repetition of samples caused by limitations imposed from using non-numeric sensory values.

In the context of smart home and elderly care, Mahmoud et al [1] investigated implications of various soft computing approaches for generating patterns of occupancy behaviour and predicting upcoming abnormal behaviours. The study considered both synthetic and physical data and identified non-linear autoregressive network with exogenous inputs as an ideal type of recurrent neural network for the prediction and forecasting task.

Lotfi et al. [2] investigated the use of simple network of sensors to monitor the behavior elderly people suffering from dementia with a focus on improving their ability to live independently. Standard home automation sensors such as motion and door entry sensors are utilized. Abnormal behaviors are identified using the acquired data and recurrent neural network is employed to forecast the upcoming events and possible sensory readings. Utilizing such predictions, the system transit certain messages to the caregivers informing them about any possible abnormal behavior in the near future.

In the context of smart home, Dawadi et al [3] and [4] utilized a machine learning based approach for monitoring the well being of individuals and assessing their cognitive health. combinations of principle component analysis, support vector machine, and logistic regression methods are utilized to assess the quality of an activity performed by participants. The study gathered sensory data from 263 participants and using the hybrid machine learning mechanism achieved a meaningful classification performance distinguishing two classes of dementia and cognitive healthy. The mixture of door, item, power usage, and motion sensors combined with activity time log are utilized to represent the activities conducted by participants. Similar study is conducted by Dawadi et al [5]. In the study sets of activities are defined and after their completions with participating elderly people, features representing each of the activities performed are assessed separately with machine learning based predictive models that are pre-trained only with features of such activity. The study considered Naive Bayse, J48, SMO, and Neural Network approaches among which Naive Bayse and Neural Network methods performed better than others.

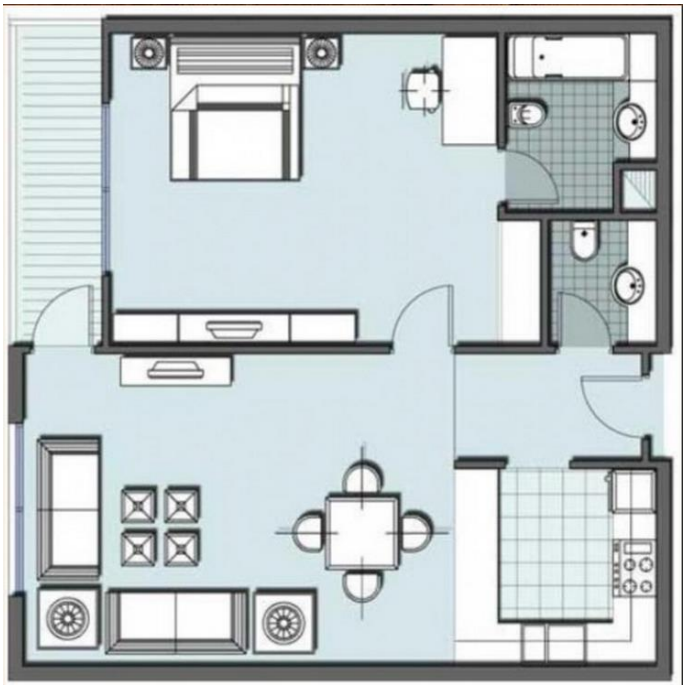

Fig. 1: A sample layout of a house with four rooms being considered in this study.

III. System Architecture for dementia friendly smart house

As mentioned earlier, in this study, a machine learning paradigm capable of providing intelligence control over lighting condition of a smart house is to be designed. Figure 1 depicts an schematic layout of the environment being consider in the study. In this study, two different designs are considered. In the first architecture, a single learning mechanism, e.g. a variation of Artificial Neural Network (ANN), with sufficient number of output nodes that is capable of handling the lighting condition of all rooms in the house is considered. The layout of this architecture is depicted in figure 2. Although this architecture is commonly employed in literature, such an architecture suffers from lack of flexibility. That is, similar to a fuzzy-based controller, adaptation of such system to a larger scale problem, e.g. controlling the lighting condition of a hospital for example, is likely to be tedious and problematic.

In order to provide a flexible and reconfigurable learning mechanism capable of being adapted to larger scale problems with minimum adaptation effort, an alternative architecture is proposed. In this architecture, the lighting condition of each room in the house is to be controlled by a separate classifier. That is, in this architecture, the lighting control is distributed across the rooms in the house. The structural design of this architecture is illustrated in figure 3. In here, the learning is distributed across classifiers that are controlling the rooms' lighting conditions. As a result, although the samples are to be representative of the status of the entire house, however, the expected reactions in terms of changes in the lighting conditions within each room are to be varied. This is facilitated by providing separated labels for each room with each sample (training and/or testing). The resulting distributed architecture

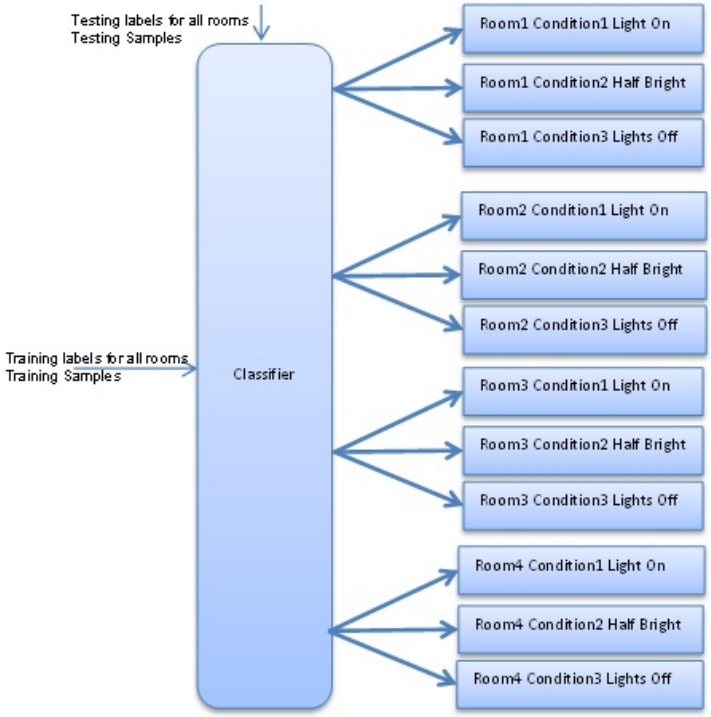

Fig. 2: Structural design of the system for a house with 4 rooms. The centric architecture.

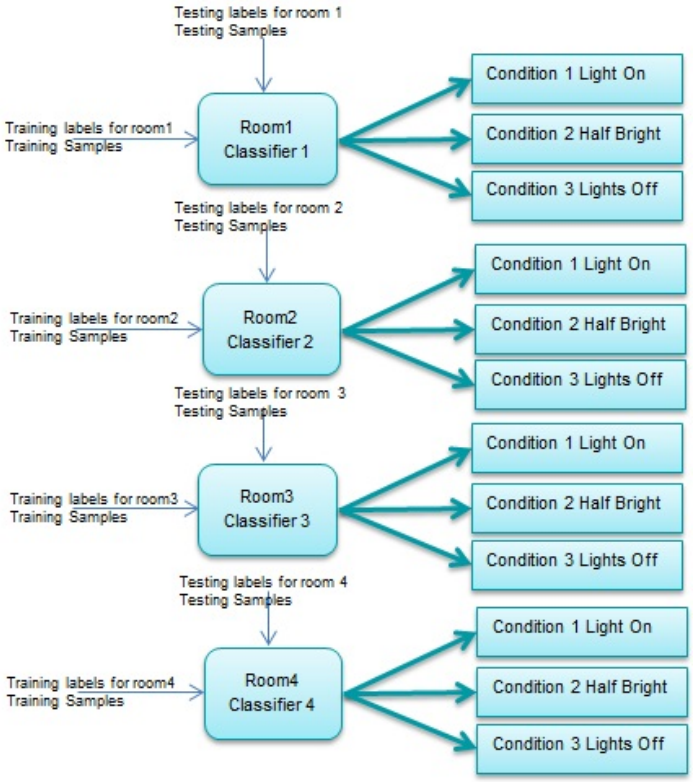

Fig. 3: Structural design of the system for a house with 4 rooms. The distributed architecture.

is highly flexible and re-scalable.

IV. Synthetic Data

This section presents the procedures followed for generating the synthetic data. In this study, following sensory inputs are considered:

- Light Detection Range (LDR) sensor: The range of sensory outputs for this sensor is assumed to be varied by time. That is, the 24 hour (day) is divided to 6 equal length periods (4 hours length each). The sensory reading within each period follows normal distribution within period-specific ranges. These periods, their associated ranges and values are presented in table I.
- Thermal camera: The camera detects whether the patient or the caregivers are present in a room. Considering a house with 4 rooms, a binary representation is utilized in which bits with 0 and 1 values respectively represent absence and presence of patient and/or caregivers.
- Displacement sensor: the sensor detects if the patient is on bed. Similar to the LDR sensor, 6 periods of 4 hours long are considered and the sensory readings within each period follow normal distribution within a certain range. These periods and their associated ranges are presented in table II. Although all the ranges are selected arbitrary however, they are deliberately set to overlap each other.

In this study, each sample represents sensory readings originating from LDR, displacement and thermal sensors. The study considers sets of 100 datasets, each containing 100 random training samples and 10 random testing samples. Figure 4 depicts the rules utilized for generating room specific labels for each sample. Two sets of datasets capturing balanced and unbalanced condition within inter classes of *'Lights Off'*, *'Half Bright'* and *'Lights On'* are considered. The choice of considering both balanced and unbalanced conditions is made due to difficulties associated with conducting complete recording sessions with patients suffering from dementia. That is, in such patients, it often happens that the data collection procedures are left uncompleted with only a sub-set of samples recorded due to inability or unwillingness of the patients to finish the tasks or recording sessions. As a consequence, it is considered advantageous for a system to be able to maintain some degree of efficiency with both balanced and unbalanced sampling conditions.

V. Experiments & Results

As mentioned in previous sections, two neural network oriented architectures of centric and distributed are considered in this study. Two sets of experiments are considered in this section to help investigating the feasibility of these two architectures with unbalanced and balanced synthetic datasets. Four well-known variations of ANN (Perceptron, Single hidden layer feed-forward neural network (SLNN) with 80 hidden nodes, Probabilistic neural network (PNN) and Multilayer feed-forward back-propagation neural network (MLNN) with three hidden layers with 40, 20 and 20 nodes in each hidden layer respectively) are considered.

TABLE I: The time periods and the associated sensory value ranges for LDR sensor

Time	Range	Value
12.00-4.00	[0,1.5]	Dark: LDR < 1.5 Half Bright: $1.5 \leq LDR > 2.5$ Bright: $LDR \geq 2.5$
4.00-8.00	[1.5,4]	
8.00-12.00	[2.5,4]	
12.00-16.00	[4,1.5]	
16.00-20.00	[2,4]	
20.00-24.00	[2.5,1.5]	

TABLE II: The time periods and the associated sensory value ranges for displacement sensor

Time	Range	Value
12.00-4.00	[0,2]	
4.00-8.00	[0,3]	
8.00-12.00	[2,3]	Sleeping on the bed≤ 2
12.00-16.00	[1,3]	Not sleeping on the bed > 2
16.00-20.00	[2,3]	
20.00-24.00	[1,2]	

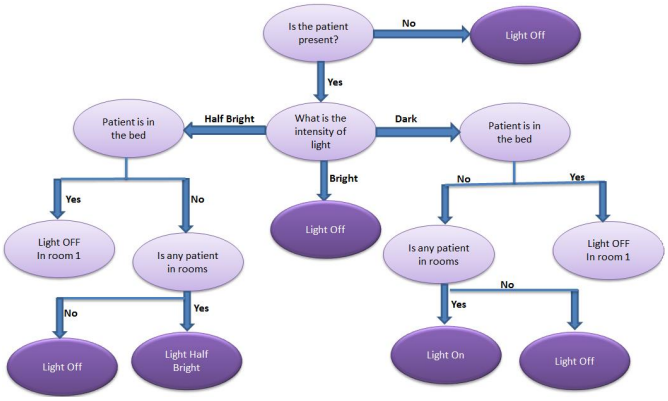

Fig. 4: Description of rules utilized for generating room specific labels for every given sample.

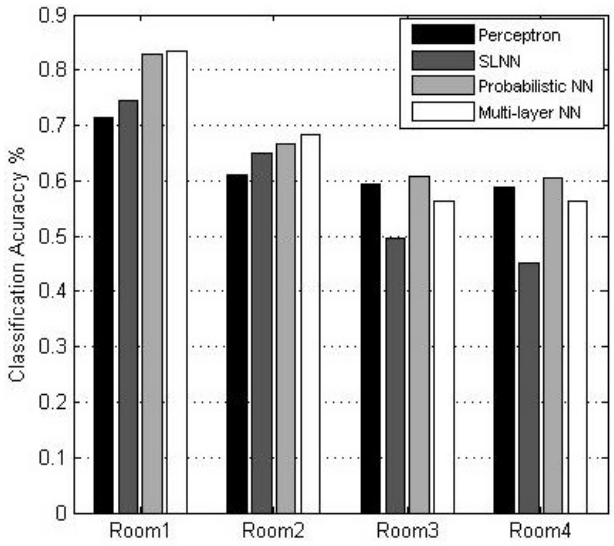

Fig. 5: Average classification accuracy achieved with the centric architecture on unbalanced datasets across four rooms in the house using variations of ANN.

A. Experiment 1: Unbalanced Data, Centric Architecture

The first experiment investigates the feasibility of the proposed architectures under unbalanced sampling condition. To do so, sets of 100 datasets utilized in this experiment are deliberately altered in a way to lack inter class balance within samples. That is, in all datasets, high percentage of samples in training and testing sets represent *'Lights Off'* class. In the training set, the percentage of samples reflecting *'Lights Off'* class in rooms one to four are set to 90%, 70%, 68% and 68% respectively. This distribution is in the range of 75%, 65%, 60% and 60% across rooms one to four respectively in the testing sets.

The overall results achieved with the centric architecture is reported in figure 5. In order to provide consistency with the distributed architecture in terms of general performance visualization, the performances are broken-down between rooms. The results indicate overall superiority of PNN across rooms closely followed by MLNN. A clear performance difference is observed between the first room (the room with a bed for the dementia suffering patient) and the other three rooms in the house.

Applying N-way ANOVA to the results revealed statistical significance across classifiers (p=$1.61728e^{-019}$) and rooms (p=$8.0147e^{-117}$) and their interactions (p=$1.43541e^{-12}$). Between classifiers, Perceptron and SLNN are significantly different from each other and PNN and MLNN while the former two lack statistical significance from each other. Between rooms, rooms 1 and 2 are significantly different from each other and rooms 3 and 4 while the former two only lack significant difference from each other. Considering unbalance/unequal distribution of training and testing samples, as observed in previous section, it is important to further investigate the results in order to gain better understanding of performances achieved by different classifiers. This section utilizes confusion matrix to illustrate the differences on true positive (TP), true negative (TN), false positive (FP) and false negative (FN) conditions with each classifier for conditions of lights off, half bright and lights on. The results are depicted in figures 6 and 7. The results highlight inefficiency of the classifiers due to their inability to avoid False Positive (FP) and False Negative (FN) conditions across all classes and all rooms.

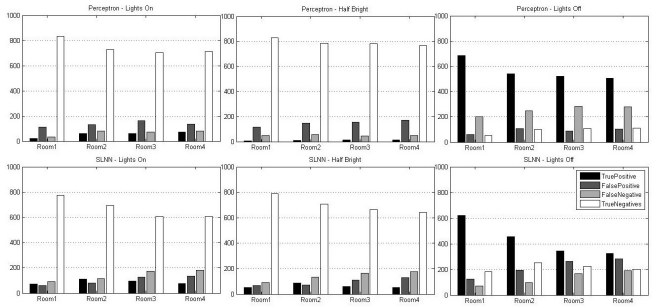

Fig. 6: Inter-class performances achieved with Perceptron and Single-Layer NN unbalanced datasets and centric architecture.

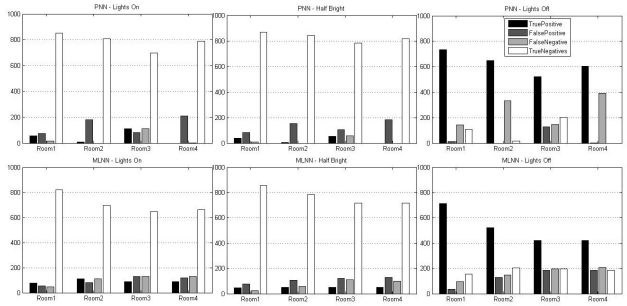

Fig. 7: Inter-class performances achieved with Probabilistic and Multi-Layer NNs unbalanced datasets and centric architecture.

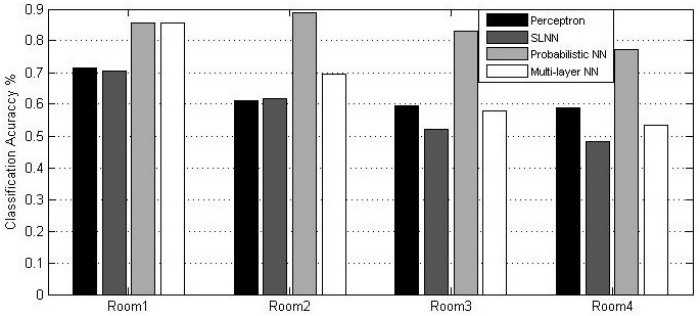

Fig. 8: Average classification accuracy achieved with the distributed architecture on unbalanced datasets across four rooms in the house using variations of ANN.

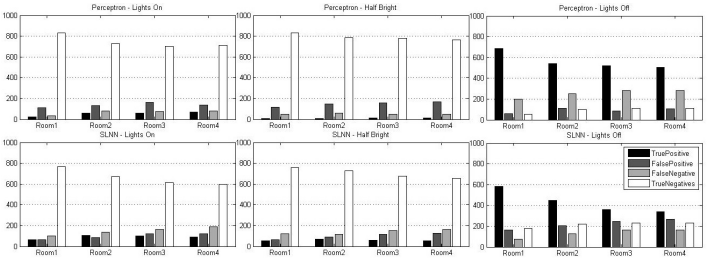

Fig. 9: Inter-class performance achieved with Perceptron and Single-Layer NN unbalanced datasets and distributed architecture.

B. Experiment 1: Unbalanced Data, Distributed Architecture

In this section the classification performance achieved with the introduced distributed architecture using the generated unbalanced synthetic data are reported. The results are illustrated on the basis of average accuracy achieved and it is categorized on the basis of the rooms in the house (see figure 8). As mentioned in previous sections, the classification approaches considered in the study includes Perceptron, Single-Layer NN, Probabilistic NN, and Multi-Layer NN. First, the differences between the performances achieved with various classifiers in each room are discussed and later the inter-class performance of the classifiers are reported.

The results indicate overall superiority of PNN across rooms followed by MLNN. Considering the best performing classification method in experiment 1, e.g. PNN, comparison between results presented in figures 5 and 8 indicate a clear advantage over using the distributed architecture. It is noteworthy that unlike the clear performance difference of PNN observed across rooms in centric architecture, such performance degradation is less obvious when the distributed architecture is utilized.

Applying N-way ANOVA to the results revealed statistical significance across classifiers (p=$3.81547e^{-132}$) and rooms (p=$5.44377e^{-8}$) and their interactions (p=$2.03979e^{-23}$). The results indicate statistical significance among all classifiers and all rooms. Figures 9 and 10 present inter-class confidence of the classifiers using a representation inspired by table of confusion. It is noteworthy that Perceptron, SLNN, and MLNN are performing similarly on both centric and distributed architectures. However, PNN improved its performance under distributed architecture by reducing number of FPs and increasing the number of TPs across rooms under *'Lights On'* and *'Half Bright'* classes in addition to reducing FNs and increasing TNs under *'Lights Off'* class.

The low number of TP and high number of TN instances on both *'Lights On'* and *'Half Bright'* classes are justifiable with the training and testing samples inter-class distributions. As mentioned earlier, the class distributions on both training and testing sets are highly biased towards having a high number of *'Lights Off'* (over 70% and 60% in training and testing sets respectively) samples. That is, the training samples used to train the classifiers to predict the lighting condition of rooms are heavily unbalanced with lights off condition having con-

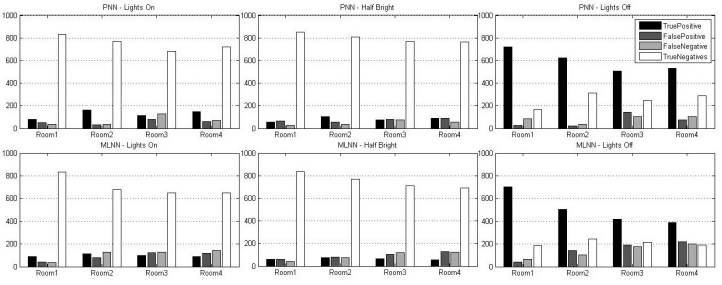

Fig. 10: Inter-class performance achieved with Probabilistic and Multi-Layer NNs unbalanced datasets and distributed architecture.

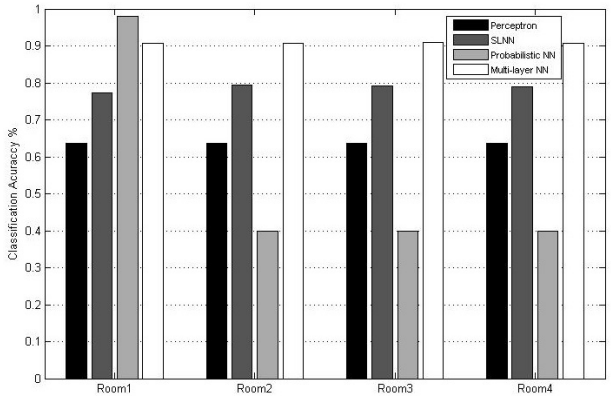

Fig. 11: Average classification accuracy achieved with the centric architecture on balanced datasets across four rooms in the house using variations of ANN.

siderably higher share of training samples compared with the other 2 conditions. This results in developing learning models that are incapable of recognizing and predicting *'Lights On'* and *'Half Bright'* conditions since their training is highly biased towards the *'Lights Off'* condition. Similar effect reported with testing sets indicate that the classification performance achieved from various classifiers studied in previous sections are likely to represent how well they can identify the *'Lights Off'* condition rather than their ability to adequately distinguish the three conditions from each other.

C. Experiment 2: Balanced Data, Centric Architecture

Considering that the results of TP, TN, FP, and FN conditions in experiment 1 indicated the variation in the performance across classifiers due to having unbalance/unequal number of training samples from different classes, the conclusion of PNN being the best performing classifier is at best restricted to the condition of lacking adequate balance between training samples. In order to better understand the feasibility of these methods for the dementia-friendly smart home scenario identified in the study, in here, the first experiment is repeated with new sets of synthetic datasets with balanced training and testing samples.

Figure 11 reports average classification performances (across 100 datasets) achieved by the classifiers under centric architecture with balanced datasets. The results indicate consistent average classification performance across classifiers in all rooms with the exception of PNN that reached to the best average classification performance in room 1 while it consistently performed poorly in all other rooms. From comparison of results presented in figures 5 and 11 it is noteworthy that with the exception of PNN, all other classifiers have considerable improvement in their average classification performances across all rooms with MLNN showing the highest performance improvement. It is also noteworthy that with the exception of room 1 in which PNN outperformed all other methods, a considerable performance degradation is observed in PNN in all other 3 rooms.

Closer look at the differences between reported inter-class performances in figures 12,13 and 6,7 reveals a noticeable

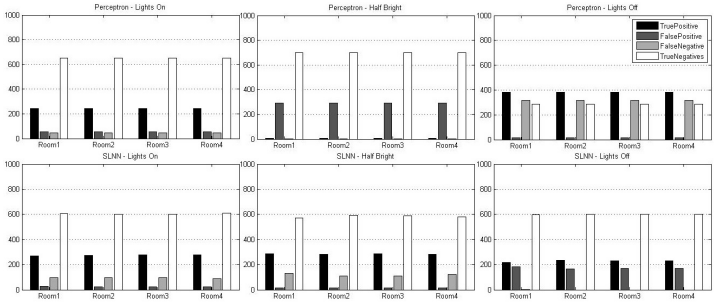

Fig. 12: Inter-class performances achieved with Perceptron and Single-Layer NN balanced datasets and centric architecture.

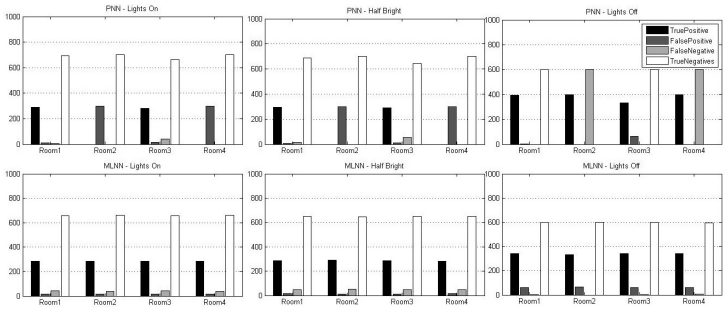

Fig. 13: Inter-class performances achieved with Probabilistic and Multi-Layer NNs balanced datasets and centric architecture.

in FPs across rooms 2 and 4 in *'Lights On'*, *'Half Bright'* and *'Lights Off'* conditions with PNN. This phenomenon is followed by considerable increased TPs in rooms 1 and 3 under *'Lights On'* and *'Half Bright'* conditions. Finally, it is noticeable that although PNN reported increment TN in rooms 1 and 3 under *'Lights Off'* condition, the decrement in TNs across all rooms under that condition is another reason behind the declined classification performance. Unlike PNN, MLNN showed consistent decrease of FNs and increased TNs in most cases. Similarly, SLNN reported declines in FPs and FNs and increases in TPs and TNs (only under *'Lights Off'* condition).

Applying N-way ANOVA to the results revealed statistical significance across classifiers (p=0) and rooms (p=0) and their interactions (p=0). The results indicate statistical significance among all classifiers. Between rooms, with exception of rooms 1 that is significantly different from all other rooms, no other statistical significance is observed.

D. Experiment 2: Balanced Data, Distributed Architecture

This section replicates the previous experiment by utilizing distributed architecture. Figure14 depicts the classification performance achieved by various classification methods in each room (averaged across all synthetic datasets). Similar to previous experiment, the datasets have inter-class balance in their training and testing sets.

Comparison between results achieved with the centric (figure 11) and the distributed (figure 14) architectures indicate clear performance improvement when the distributed

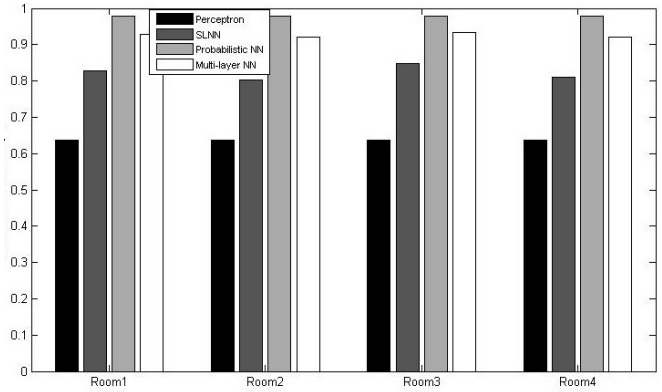

Fig. 14: Average classification accuracy achieved with the distributed architecture on balanced datasets across four rooms in the house using variations of ANN.

architecture is utilized (under inter-class balanced datasets). In addition, the consistencies across rooms and classifiers are noteworthy. Comparison between results achieved with balanced and unbalanced synthetic datasets using the distributed architectures (figures 14 and 8 respectively) indicate clear performance improvements across all classifiers in all rooms with the exception of Perceptron which demonstrated decreased performance in the first room and neglect-able performance increase in all other rooms under balanced dataset. Considering the differences between reported inter-class performances in figures 12,13 (centric architecture with inter-class balance datasets) and figures 15 and 16 indicate slight decrement of FN and slight increment of TP across all rooms in SLNN under *'Lights On'* and *'Half Bright'* classes. PNN illustrated considerable increase in TN and noticeable decrease in FN in rooms 2 and 4 under *'Lights Off'* class in addition to considerable decrease of FP and noteworthy increase of TP in rooms 2 and 4 under *'Lights On'* and *'Half Bright'* classes. This phenomenon resulted in major improvement in classification performance of PNN when distributed architecture is utilized. Perceptron and MLNN did not illustrated any major difference in their inter-class performances across the two architectures.

Considering the inter-class performance differences of classifiers reported in figures 9 and 10 (distributed architecture with inter-class unbalanced datasets) and figures 15 and 16 (distributed architecture with inter-class balanced datasets) a clear decrement of FPs and FNs in addition to a clear increment of TNs and TPs are observed across all rooms with all classifiers across all three classes of *'Lights On'*, *'Half Bright'* and *'Lights Off'*. This is with the exception of Perceptron which reported increased FNs under *'Lights Off'* class, increased FPs under *'Half Bright'*class and increased TPs under *'Lights On'* class.

Applying N-way ANOVA to the results revealed statistical significance only within classifiers (p=0) while no such significant difference is observed across rooms (p=0.1518) or the interactions of rooms and classifiers (p=0.4434). The results indicate statistical significance among all classifiers.

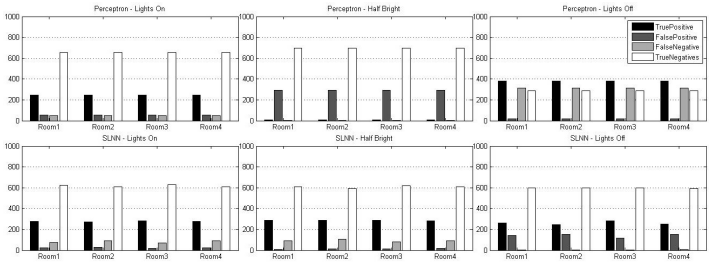

Fig. 15: Inter-class performances achieved with Perceptron and Single-Layer NN balanced datasets and distributed architecture.

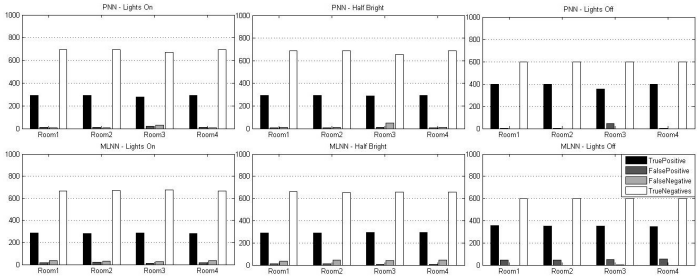

Fig. 16: Inter-class performances achieved with Probabilistic and Multi-Layer NNs balanced datasets and distributed architecture.

VI. Conclusion

Dementia is a growing problem in societies with aging populations due to intense level of care required and the associated costs in order to facilitate such care. Providing a safe environment in which the dementia patients (who are in the earlier stages of the disease) can live independently can improve the patients quality of life. Sleep disturbance is a common symptom in dementia patients. Patients inability to turn on the light by themselves, being frightened by room darkness, and possible accidental falls are some of the issues associated to such sleep disturbance. Clinical studies indicate that appropriate level of lighting can help to restore the rest-activity cycles of these patients. This study proposed a distributed learning mechanism on the backbone of machine learning solutions to address the required lighting control. The proposed architecture considered a collection of learning methods (classifiers) each being responsible to handle the lighting condition of a single room in the house. This architecture is scalable and provides efficient and smart control over lighting condition of multiple rooms in the house. An alternative lighting control architecture, called centric architecture, that employs a single learning mechanism, e.g. a classifier, to control the lighting condition of all rooms in the house is considered to assess feasibility of the proposed distributed architecture.

Four classification methods are considered and their feasibilities are assessed using a collection of synthetic data. Two sets of experiments reflecting balanced and unbalanced data sampling scenarios for a smart house with four rooms are designed. The samples reflected multiple scenarios with

possibility of having a dementia patient and caregiver in different rooms of the house. The results indicated the feasibility of such distributed control approach for controlling the lighting conditions of multiple rooms irrespective to each other. Probabilistic neural network is identified as the most feasible classification method for such an architecture.

VII. Future Work

Several future directions can be considered for the current study including assessing the robustness of the distributed architecture proposed in this study in higher scale environments such as special dementia facilities and hospitals with multiple patients with higher variety of patients' behavioural patterns. Another possible future direction is to introduce more complex scenarios capturing more than three lighting conditions (e.g., *Lights on*, *Lights off*, and *Half Bright*) as well as extending the current architecture to cover multi-objective scenarios in which in addition to addressing the lighting needs of the patients and caregivers the overall energy consumption is reduced. The stated future directions are in addition to obvious necessity of assessing the feasibility of the architecture proposed in the study against real-world data to be captured from activities of real patients interacting with the system.

References

[1] S. M. Mahmoud and A. Lotfi and C. Langensiepen, *Behavioural pattern identification and prediction in intelligent environments*, Applied soft computing, Elsevier, 13, 1813–1822, 2013.

[2] A. Lotfi and C. Langensiepen and S. M. Mahmoud and M. J. Akhlaghinia, *Smart homes for elderly dementia sufferers: Identification and prediction of abnormal behaviour*, Journal of Ambient Intelligence and Humanized Computing, 3(3), 205–218, 2012.

[3] P. N. Dawadi and D. J. Cook and M. Schmitter-Edgecombe and C. Parsey, *Automated assessment of cognitive health using smart home technologies*, Technol Health Care 21(4), 323–343, 2013.

[4] P. N. Dawadi and D. J. Cook and M. Schmitter-Edgecombe, *Automated cognitive health assessment using smart home monitoring of complex tasks*, IEEE transactions on systems, man, and cybernetics:systems 43(6) 1302–1313, 2013.

[5] P. N. Dawadi and C. Parsey and M. Schmitter-Edgecombe, *An approach to cognitive assessment in smart home*, Proceedings of the 2011 workshop on Data mining for medicine and healthcare, pp. 56–59, 2011.

[6] Z. Nagy and F. Y. Yong and M. Frei and A. Schlueter, *Occupant centered lighting control for comfort and energy efficient building operation*, J. Energy and buildings, Springer. doi.org/10.1016/j.enbuild.2015.02.053, 2015.

[7] K. Appold, *Lighting Affects Dementia Patients' Sleep*, Today's Geriatric Medicine 7(5) 10–10, 2014.

[8] A. K. Gopalakrishna and T. Ozcelebiy and A. Liotta and J. J. Lukkien, *Exploiting Machine Learning for Intelligent Room Lighting Applications*, 6th IEEE International Conference on Intelligent Systems (IS), 406–411, 2012.